THE UNIVERSITY OF CHICAGO

HOW FORMATION AND EVOLUTION IMPACT THE ABUNDANCES OF BIOCRITICAL ELEMENTS IN PLANETS AND PLANETARY ENVIRONMENTS

A DISSERTATION SUBMITTED TO
THE FACULTY OF THE DIVISION OF THE PHYSICAL SCIENCES
IN CANDIDACY FOR THE DEGREE OF
DOCTOR OF PHILOSOPHY

DEPARTMENT OF THE GEOPHYSICAL SCIENCES

BY
MEGAN NICOLE DE WIT BARNETT

CHICAGO, ILLINOIS
DECEMBER 2023

"This is war, Peacock. Casualties are inevitable. You can not make an omelet without breaking eggs, every cook will tell you that."

- Colonel Mustard

TABLE OF CONTENTS

LIST OF FIGURES

LIST OF TABLES

ACKNOWLEDGMENTS

It is hard to know who to thank when one finishes a crushingly hard task. There are so many people who encouraged, supported, and helped me along the way to eventually writing and submitting this thesis.

I thank my husband, Dr. Blake Sanders, for his love and support. I thank my friends, including those who are no longer in my life, for the wonderful times we've had and the shoulders they lent me to cry on (particular shout-outs go to Montana Strohl-Roy, Adina Feinstein, and Celeste Keith). I thank my family, although let's be real, they didn't actually do much other than come to my defense. But they did raise me for 18 years, so that's something!

I particularly thank my beloved cats, both past and present, for their unconditional love and oodles of snuggles. Celeste and Squeak, you will always be remembered. Raven, Carmine, and Jupiter, you are the loves of my life (other than my husband) and I cherish every minute I have with you.

Finally, I thank myself. I honestly didn't think we would get to this point at times, and I can't believe I'm here now. This has been a damn near Herculean task, and I did it. Way to go, me!

ABSTRACT

In the search for life outside of Earth, the key targets for current exploration are icy moons within our solar system and terrestrial exoplanets within the habitable zones of their central stars. This is because, as liquid water has been a key component for the evolution of life on Earth, icy moons with subsurface oceans and terrestrial exoplanets with surface liquid water are believed to yield potential environments in which extraterrestrial life could originate. However, the presence of liquid water is not the only requirement for life, as organisms need an ample supply of biocritical elements (carbon, nitrogen, oxygen, phosphorus, sulfur, and hydrogen) that represent the major components of proteins and DNA, the building blocks of cellular structure and biochemistry. Whether a planetary body ends up with the requisite inventory of the elements needed for life's inception depends on a series of complex, interconnected processes including formation and subsequent geophysical evolution of the planetary body, making understanding their effect on the resulting supply of biocritical elements crucial to predicting whether life can originate in a given environment.

In this thesis, I model the processes surrounding early giant planet formation, satellite formation, and the effect of planetary obliquity on terrestrial planet geophysical evolution in order to characterize how these processes impact the abundances of biocritical elements available for life in planets and planetary environments. In Chapter 2, I explore the effects of an actively forming, luminous giant planet core on local, volatile-rich solids within the protoplanetary disk. I find that a critical transition occurs where very hot (rapidly accreting) cores drive volatiles off of solids that are either accreted or experience a close fly-by with the core, while cool cores (slowly accreting) do not strip volatiles from nearby material. In Chapter 3, I model both the production of refractory carbon and nitrogen species (carbon and nitrogen molecular carriers that freeze out at temperatures higher than 40K such as CO_2 and NH_3) and their accretion by growing satellites within the circumplanetary disk (CPD) that originates during the late stages of giant planet formation. While we find that refractory carbon and nitrogen species are produced within our modeled CPDs, these

species are not efficiently accreted by forming satellitessimals and hence cannot contribute to growing satellites' carbon and nitrogen inventories. Therefore, in order for satellites with rich biocritical element inventories to form, refractory carbon and nitrogen species must be supplied from the protoplanetary disk. Finally, in Chapter 4, I model and analyze the effects that moderately high planetary obliquity (45°) has on planetary oxygenation potential and compare the resulting effects with those caused by increased phosphate and ocean remineralization depth. We find that moderately high obliquity planets experience increased planetary oxygenation potential due to an increase in photosynthethic oxygen production rates by marine organisms and a decrease in oceanic oxygen solubility when compared to their low obliquity counterparts. Moderately high obliquity planets may then prove to be more conducive to the evolution of complex life than Earth.

CHAPTER 1

INTRODUCTION

Curiosity about the worlds that exist beyond our own, and the potential life they could harbor, has long existed in the psyche of humanity. Babylonian astronomers were among the first to identify and record the existence of planets other than Earth (around 2000 BC, discussed in literature such as Olmstead, 1938; Neugebauer, 2012), and curiosity surrounding planets other than our own has only intensified as technology has increasingly allowed us to observe, and in some cases experience, both the planetary bodies in our solar system and beyond.

Naturally, when astronomers started looking to other planets and moons in both our solar system and extrasolar systems, they began to wonder whether life could exist beyond the confines of Earth. Though hampered by limitations in remote sensing and space travel in early years, planetary science and astronomy are now at a stage where we are actively searching for planetary environments that could be hospitable to either terrestrial or extraterrestrial life. As life on Earth spent the majority of its evolution within the oceans and likely originated within shallow ponds on Earth's surface, liquid water became the key sought-after indicator of the potential for life on another planet. NASA and other space agencies encouraged this idea, popularizing the term "follow the water".

In response to this motivation, there have been a variety of remote sensing and surface missions sent to investigate the environments of and search for liquid water (past or present) on planets and moons within our solar system. Mars and Venus, Earth's closest terrestrial analog siblings, were of early interest due to their similarities in size and proximity to Earth. The hope was that Mars, Venus, or both planets may harbor liquid water on their planetary surfaces, yielding potential environments for life to have originated and exist in. However, the current day conditions of both Venus and Mars were shown to be inhospitable to life through missions such as the Venera, Vega, and Magellian missions (Marov, 1978) to Venus and missions such as the Mars Odysessy, Mars EXpress, and rover missions to Mars (e.g. Christensen et al., 2003; Arvidson et al., 2011; Titov et al., 2016). Venus' surface water was lost long ago and its current oppressive atmosphere and extreme surface temperatures

cannot support liquid water (e.g. Kasting & Pollack, 1983; Kulikov et al., 2006), while water detected on Mars' surface is transient and unstable due to its tenuous atmosphere (e.g. Hecht, 2002; Richardson & Mischna, 2005; Wray, 2021). This renders both Venus and Mars unlikely candidates for extant life.

Another group of identified potential targets in the search for extraterrestrial life within our solar system lie within the gas giant or ice giant planetary systems, such as the Jovian and Saturnian systems. Though gas giant planets Jupiter and Saturn are considered highly unlikely candidates for life, their satellite systems contain a small number of moons that could potentially host life. A variety of these moons, including Europa, Callisto, Ganymede, Enceladus, and Titan, were discovered to have water ice surfaces through ground-based telescope observations and fly-by missions (e.g. Voyager 1 and 2). Though these icy surfaces were not believed to have liquid water, it was possible that underneath the ice lay liquid water oceans.

Motivated by this possibility, various icy moons within the Jovian and Saturnian systems have been targeted by subsequent missions to evaluate the potential for subsurface oceans, and by extension life, on these moons. The Galileo mission, launched to remotely observe Jupiter and its main four Galilean moons (Johnson et al., 1992), yielded measurements from the onboard magnetometer and surface images that strongly suggested Europa, Ganymede, and Callisto harbor subsurface oceans (Carr et al., 1998; Khurana et al., 1998; Pappalardo et al., 1999; Kivelson et al., 2000; Zimmer, 2000). Similarly, the Cassini-Huygens mission to observe Saturn and its moons not only provided gravitational evidence for sub-surface oceans on Titan and Enceladus (e.g. Lorenz et al., 2008; Béghin et al., 2009, 2010; Iess et al., 2014) but also observed water vapor geysers ejected from the surface of Enceladus from a deep, interior water source (e.g. Parkinson et al., 2007).

The findings from these missions and subsequent studies afterwards have cemented icy moons as prime targets for ongoing searches for extraterrestrial life. Multiple missions are on the horizon in the next decade to the icy moons of our solar system, including the recently

launched JUICE mission (Grasset et al., 2013) and the upcoming Europa CLIPPER and Dragonfly missions (Phillips & Pappalardo, 2014; Lorenz et al., 2018), which aim to further investigate and characterize the potential subsurface oceans on Europa, Ganymede, and Callisto (among other scientific goals).

Additionally, though the terrestrial planets in our solar system are not currently habitable, a large number of exoplanets have been detected outside our own that could potentially harbor life. To date, over 5000 exoplanets have been discovered through ground-based observations, radial velocity measurements, and missions such as Kepler (Borucki et al., 2010; Howell et al., 2014) and the Transiting Exoplanet Survey Satellite (TESS) (Ricker et al., 2014). Though some of the currently detected exoplanets are categorized as giant planets, and therefore unlikely candidates for life, a fraction of detected exoplanets are believed to be terrestrial planets within their central star's habitable zone (Kane et al., 2016) which is the range of orbital separations from a central star where the resulting equilibrium temperature would allow liquid water to exist on the planet's surface (e.g. Kasting et al., 1993).

Terrestrial exoplanets have also been marked as prime targets for the search for extraterrestrial life. Future missions to determine planetary habitability and potentially detect current extraterrestrial life on terrestrial exoplanets are on the horizon. For example, next space generation telescopes such as the LUVOIR-like observatory have been recommended for launch by the Astro2020 Decadal Survey, and would seek to further characterize the atmospheres of terrestrial exoplanets predicted to be habitable and possibly detect biosignatures (Wang et al., 2018).

While the prospect of liquid water has been the driving factor behind searching for life on planetary bodies, water is not the only requirement for life to originate and thrive. The building blocks of life are built from six primary biocritical elements: carbon, nitrogen, oxygen, phosphorus, sulfur, and hydrogen. Of these elements, carbon and nitrogen are suggested to be the most important as carbon acts as the scaffold for the biochemistry for life on Earth, and nitrogen is a key component in the nucleic and amino acids (e.g.

Capone et al., 2006; McKay, 2014) that are the building blocks for organisms on Earth. The availability of important biocritical elements is not guaranteed where liquid water exists and is instead set by planetary composition, which here we take to mean the abundance of biocritical elements. Planets with compositions that are poor in biocritical elements are unlikely to be able to support life, even if liquid water is present on the planet's surface, while planets that are comprised of molecular species with high amounts of biocritical elements are more likely to allow life to originate and thrive. Hence, in order to predict whether life could potentially originate on another water-bearing planet or a moon it is necessary to evaluate the extent of their biocritical element inventories, particularly carbon and nitrogen.

Planetary composition can be gleaned directly through analyzing samples from meteorites or from the planet surface, such as has been done for the Earth and Mars. However, for the icy moons of our solar system and extrasolar planets, there is not currently a way to directly determine the composition of these bodies. Remote measurements of icy satellite gravitational moments and magnetic fields have provided insights into the general configuration of icy satellite interiors and provided clues to the conductive characteristics of potential sub-surface oceans (e.g. Anderson et al., 2004; Jacobson, 2004; Sotin et al., 2021), but the composition of these bodies is unable to be determined by these measurements alone. This means that in order to predict the composition of icy moons and exoplanets, and by extension the size of their biocritical elementary inventory, one needs to model the processes that determine composition.

Predicting planetary compositions is not an easy task, however, as a planetary or satellite is a very integrated system whose properties rely both on the formation history of the object as well as the geophysical processing that occurs throughout its evolution. Due to the importance of understanding how formation and subsequent geophysical evolution affects the eventual planetary composition and environment that life would originate in, I became interested in how involved these processes are in setting the habitability of planetary bodies, and pursued projects to better understand them in this thesis.

In order to begin to investigate how planet formation and subsequent planetary evolution affect habitability, one first needs to understand the process of planet formation and the physical mechanisms at play. As such, I briefly review the current understanding of terrestrial and giant planet formation, as well as regular satellite formation, below.

1.1 A Brief Overview of Terrestrial Planet, Giant Planet, and Regular Satellite Formation

Planet formation is a process that is intricately linked with and driven by star formation. When interstellar gas collects and reaches a threshold critical mass, it begins to collapse inwards on itself due to self gravity overwhelming the opposing pressure force. This collapse of gas begins the process of stellar formation. As the gas collapses inwards, angular momentum conservation causes the gas and dust to spiral down and flatten into a disk around the star.

Gas and dust are transported through the disk, feeding the growing star. However, not all material in the protoplanetary disk is necessarily lost to the star as some material is transported outwards in the disk as a consequence of angular momentum conservation. As the forming star and protoplanetry disk evolve, material feeding into and moving through the disk also has the potential for incorporation into larger solids and, eventually, becoming the building blocks that planets form from. Here, we discuss the current understanding of the formation methods of the smallest and largest planets in our solar system, the terrestrial planets and the gas giant planets, as well as the formation of regular satellites around gas giant planets.

1.1.1 Terrestrial Planet Formation

Terrestrial planets are, as their name suggests, primarily comprised of rocky and metallic materials and have been found to reach up to $\sim 1.5 R_\oplus$ in radius (note that some nuance exists here for the maximum radius of terrestrial planets, as discussed in references including

Rogers, 2015; Fulton et al., 2017; Van Eylen et al., 2018; Petigura, 2020). The rocky material for these planets comes from both dust entrained within the interstellar gas, and so was incorporated into the forming protoplanetary disk with the gas, as well as processed dust that was destroyed and reformed (for example: CAIs, chondrules, etc. See MacPherson, 2014; Russell et al., 2018).

As material flows through the protoplanetary disk, solids settle down into a thin layer in the midplane of the protoplanetary disk in the absence of strong turbulence due to the central star's gravity (Weidenschilling, 1980). This creates a reservoir of solid material at the midplane of the disk which particles can use as feedstock to grow from micron-sized or smaller dust grains to planetesimals with radii of hundreds of kilometers.

Fundamentally, solids are able to increase their mass through collisional growth. In this growth mechanism, dust grains collide with each other in the dense midplane region of the disk and stick together, coagulating into larger solids (e.g. Weidenschilling, 1980; Beckwith et al., 1999; Dullemond & Dominik, 2005; Raymond et al., 2005; Ciesla, 2007; Alexander, 2008; Güttler et al., 2009; Wada et al., 2009; Birnstiel et al., 2010, 2012; Morbidelli et al., 2012; Visser & Ormel, 2016). Ideally, this process would repeat until solids reach planetesimal size.

The collision growth mechanism, however, faces two significant barriers that need to be overcome for planetesimal formation to occur. The first barrier is radial drift. Solids in the protoplanetary disk are subject to gas drag, which causes them to migrate inwards towards the central star (Weidenschilling, 1977). This force increases as solids grow bigger until they reach around a meter in radius, after which the effect of radial drift on the solid decreases (Weidenschilling, 1977). This creates what is referred to as the "meter-sized barrier", where growing small solids drift inwards towards the central star on timescales faster than their growth timescale. These solids are accreted by the central star before they are able to grow large enough to overcome radial drift. This prohibits solid growth, preventing the creation of planetesimal sized solids.

Additionally, as drag force is size dependent, collisions between particles can reach high relative speeds. If the relative collision speed between particles is high enough (on the order of 10 m/s or higher depending on solid composition Wada et al., 2009; Gundlach & Blum, 2015), the collision could result in the solids bouncing off each other (Zsom & Dullemond, 2008; Güttler et al., 2009) or fragmenting (Birnstiel et al., 2011; Morbidelli et al., 2012) instead of coagulating, providing another barrier to growth.

There are a few ways that the collisional growth mechanism can overcome its growth barriers. Growing particles can avoid bouncing and fragmentation during collision if the particles are low density such as if the solids are porous or comprised of fluffy aggregates, or if the solids are comprised of material with high sticking efficiency like water ice (e.g. Wada et al., 2009; Okuzumi et al., 2012). For the meter-sized barrier issue, solids could potentially avoid rapid inwards migration and accretion upon reaching a meter in radius if solids find themselves in a pressure bump, where inwards radial drift velocities go to zero (e.g. Drazkowska et al., 2013). Finally, solid growth through mechanisms such as the streaming instability (e.g. Youdin & Goodman, 2005) and gravitational collapse (e.g. Weidenschilling, 1995) as these processes lead to the concentration of small particles which are then able to collapse into planetesimal-sized solids, by-passing the meter-sized barrier entirely.

Once planetesimals have successfully formed, their growth continues until they become full terrestrial planets. These planets also undergo subsequent geophysical processing after their formation is concluded. However, the solids incorporated into a forming planet are a foundational component of a planet's composition. Hence, the composition of those solids, which in turn is dependent on under what conditions the solids originated, what their evolutionary history was like, and what thermal or chemical processing the solids have undergone, directly influences the composition and biocritical elemental inventory of the final terrestrial planet. As such, these driving mechanisms for planetary growth and the evolutionary histories of solids that are incorporated into growing planets need to be understood to predict the composition of a planet.

1.1.2 Gas Giant Planet Formation

At the other end of the mass spectrum from terrestrial planets, gas giant planets (here after referred to as giant planets) are comprised of a large gaseous envelope, containing primarily hydrogen and helium, with a rocky/metallic central core that may partially extend into and enrich the interior gaseous envelope region (e.g. Helled et al., 2014; Wahl et al., 2017; Müller et al., 2020). The two leading models for giant planet formation, the gravitational instability and core accretion models, have been well developed and quantitatively investigated in the last 30 years (Pollack et al., 1996; Boss, 1997, 2002; Levison et al., 2010). As the core accretion formation model is favored for close-in giant planets such as Jupiter and potentially Saturn, we discuss this model in detail here.

In the traditional core accretion model, giant planet formation occurs in three distinct stages. Phase 1 consists of the rapid accretion of solids into a solid protoplanetary core, and was believed to follow the same growth sequence as terrestrial planets. This phase ends when solids are depleted from the area surrounding the forming giant planet core, and the core enters Phase 2 in which it undergoes slow accretion of gas and any new surrounding solids that drift into the vicinity of the planet. The final phase, Phase 3, marks the end of giant planet formation where the core reaches a critical mass allowing runaway accretion of gas to start and continue until the surrounding gas dissipates. However, in this traditional view of giant planet formation, core formation experienced a significant hurdle that would make giant planet formation difficult.

The issue that arises when forming a giant planet core through this traditional view is that of the formation timescale for the core during Phase 1 of growth. Early studies of core formation through planetesimal accretion predicted the timescale needed to form a large enough core to initiate runaway gas accretion ($\gtrsim 10 M_\oplus$, Pollack et al., 1996) was on the order of 6-8 million years or longer (Pollack et al., 1996; Hubickyj et al., 2005), which is longer than the typical expected lifetime of gas in the protoplanetary disk of 3-5 million years (e.g. Haisch et al., 2001; Sicilia-Aguilar et al., 2006; Hernández et al., 2007; Wyatt,

2008; Mamajek et al., 2009). This presents a massive problem for giant planet formation, as core formation must occur before the dissipation of the protoplanetary disk in order for the core to be able to accrete surrounding gas.

However, this timescale issue may be mitigated by either increasing the surface density of the surrounding disk (Pollack et al., 1996; Lissauer & Stevenson, 2007) or by core formation through pebble accretion (the rapid accretion of small dust aggregates due to the effect of gas on small particle drift, e.g. Lambrechts & Johansen, 2012; Chambers, 2014; Bitsch et al., 2015; Johansen & Lambrechts, 2017). Increasing the surface density of the surrounding disk would yield a larger reservoir of solid material in the vicinity of the forming planet, which would then decrease the timescale for core formation (Lissauer & Stevenson, 2007). Core formation by pebble accretion also would decrease the timescale for core formation, as the growing core would be able to effectively accrete small dust aggregates (pebbles) on the scale of millimeters to meters due to the effect of gas drag on radial particle drift, which resupplies the feeding zone with solids (Levison et al., 2010; Johansen & Lacerda, 2010; Ormel & Klahr, 2010; Ormel & Kobayashi, 2012; Lambrechts & Johansen, 2012; Levison et al., 2015). Models of giant planet core formation through pebble accretion have demonstrated that core growth to a mass where runaway gas accretion begins is possible on timescales much less than the lifetime of the protoplanetary disk, yielding this process as a likely mechanism for the first phase of giant planet formation (e.g. Johansen & Lacerda, 2010; Ormel & Klahr, 2010; Ormel & Kobayashi, 2012; Lambrechts & Johansen, 2012; Levison et al., 2015).

From our understanding of giant planet formation, we can see that, like for terrestrial planet formation, the composition of the material that is present during giant planet formation is a key determinant in the giant planet's final composition. However, unlike terrestrial planet formation, giant planets are primarily comprised of gas accreted from the protoplanetary disk, meaning that the composition of accreted gas will likely play a large role in determining the composition of giant planets.

1.1.3 Regular Satellite Formation

Moons around giant planets are categorized into two different types, regular satellites and irregular satellites. Due to regular satellites' circular, prograde, low eccentricity orbits along the equatorial plane of the central planet, these moons are believed to have formed within a gaseous and solid disk that forms around a giant planet, called a circumplanetary disk (CPD) (e.g. Peale, 1999). Irregular satellites, in contrast, are believed to have formed outside their host giant planet's local environment and were later gravitationally captured (McKinnon et al., 1995; Schubert et al., 2010; Nogueira et al., 2011; Masters et al., 2014), leading to retrograde and/or highly eccentric orbits.

When a giant planet begins accreting gas, the planet undergoes a period of contraction due to energy loss while simultaneously gaining mass and angular momentum from material falling onto the planet (e.g. Ward & Canup, 2010). This causes the planet to become rotationally unstable and throw off gaseous material into the local area surrounding the giant planet. This shed material then becomes a circumplanetary disk orbiting the planet.

Three dimensional, high resolution (e.g. Bate et al., 2003; Fouchet & Mayer, 2008; Ayliffe & Bate, 2009; Szulágyi et al., 2014, 2016) hydrodynamical models which track the motion of gas during giant planet formation result in the formation of circumplanetary disks as a consequence of the forming giant planet. Additionally, observations of protoplanetary disks (Wolff et al., 2017; Pineda et al., 2019; Rab et al., 2019; Christiaens et al., 2019) and potential circumplanetary disks (Christiaens et al., 2019; Benisty et al., 2021; Wu et al., 2022) provide real-world evidence to support the existence of circumplanetary disks during giant planet formation.

Even after the circumplanetary disk forms, gas from the surrounding protoplanetary disk continues to be accreted onto the growing central planet, with gas entering the CPD first instead of directly falling into the planet due to its higher angular momentum. Using 3D hydrodynamical simulations to study the accretion and subsequent flow of gas within the circumplanetary disk, Tanigawa et al. (2012), Morbidelli et al. (2014), Szulágyi et al.

(2016), and Szulágyi (2017) all found that in their models, the majority of gas accreted onto the circumplanetary disk falls vertically onto the CPD surface from higher altitudes in the protoplanetary disk, while gas near the midplane spiraled outward beyond the planet's Hill sphere.

While gas is solely supplied to the CPD through vertical accretion onto the disk surface, there are two potential sources of solids from the protoplanetary disk. The first is micron-sized dust entrained in gas from the protoplanetary disk. While larger dust (Stokes numbers $\sim 1\times10^{-2}$ to 1) is much less coupled to the surrounding gas flows (Weidenschilling, 1980) and settles to below the point where the flow of gas onto the CPD originates (e.g. Tanigawa et al., 2012, 2014; Homma et al., 2020; Szulágyi et al., 2022), small dust grains are strongly coupled to the flow of surrounding gas within the protoplanetary disk. Hydrodynamic simulations have shown that these entrained small grains are able to be carried into the CPD with the vertically infalling gas (e.g. Tanigawa et al., 2014; Homma et al., 2020), while large solids are unable to enter the CPD through this route.

The second possible source of solids for the CPD is the capture and ablation of planetesimals from the protoplanetary disk. Planetesimals orbiting in the protoplanetary disk may be captured by the CPD through drag-assisted capture and strongly ablated due to frictional heating as the solid moved deeper into the CPD (Lambrechts & Johansen, 2014; Ronnet & Johansen, 2020). As the planetesimal breaks down under the strong frictional heating, pebble-sized solids (0.1 - 1mm in the CPD) are deposited within the CPD. Evolutionary models of planetesimal swarms around a proto-Jupiter and CPD suggest that this process is efficient and able to supply the CPD with solids that could then serve as the building blocks for pebble accretion of satellites (Ronnet & Johansen, 2020).

These two sources of solids provide the feedstock that satellites grow out of within the CPD. Satellites are expected to undergo a very similar growth sequence and growth mechanisms as terrestrial planets (Canup & Ward, 2002, 2006; Pappalardo et al., 2009; Shibaike et al., 2017; Batygin & Morbidelli, 2020), making the composition of the solid materials

that form the satellites a key determinant for satellite composition. However, material that forms satellites experiences not only conditions within the protoplanetary disk, but also the environment of the CPD. The conditions within the CPD may be very different from those in protoplanetary disk (e.g. Coradini et al., 2010; Ward & Canup, 2010; Szulágyi, 2017; Szulágyi & Mordasini, 2017; Batygin & Morbidelli, 2020), potentially leading to thermal or chemical processing of material with the CPD (Prinn & Fegley, 1981; Mousis et al., 2002; Alibert et al., 2005; Oberg et al., 2022, 2023).

1.2 The Link Between Formation and Evolution for Habitability

Investigation into how formation conditions affected the volatile inventory of biocritical elements such as carbon have shown that formation conditions greatly affected the inventory of such elements on Earth (e.g. Bergin et al., 2015; Hirschmann et al., 2021; Li et al., 2021). Other studies have also demonstrated that the initial volatile inventory of species on planetary bodies can greatly affect their evolution (Castillo-Rogez & Lunine, 2010; Castillo-Rogez & McCord, 2010; Castillo-Rogez, 2011). As such, how a planet forms and the composition of solids that are present during planet formation is a key determinant for a planet's future habitability.

Intrigued by the concept of looking at how formation influences the final environment and composition of planets and planetary bodies, I turned my focus towards looking at how giant planet formation affects both the composition of solids being accreted by and around the planet, as well as the composition of the regular satellites. There are many open questions remaining about how the conditions under which a planet forms affects its resulting composition and subsequent geophysical evolution, many of which stem from the environment caused by the energetics of planetary body formation.

Planet formation involves many energetic processes which serve to heat the young planet and surrounding environment. The energy released from a growing planet in the form of luminosity is modeled to range from 1×10^{-7} $L_{\odot}$ to 1×10^{-4} $L_{\odot}$ through the giant planet

formation process (Pollack et al., 1996; Mordasini, 2013). This luminosity range translates into planetary surface temperatures ranging from the low hundreds to thousands of degrees Kelvin. Hence, the effective temperatures of forming planets are much higher than the surrounding gas temperatures. The increased temperature could then warm disk material in the planet's Hill sphere, or even beyond (Montesinos et al., 2015; Cleeves et al., 2015; Szulágyi, 2017; Szulágyi & Mordasini, 2017). Increased temperatures due to forming giant planet luminosity also have the potential to chemically alter solids that are in the local vicinity during giant planet core formation, an effect that has not been considered.

Similarly, though the accretion of gas and solids onto the CPD and materials' subsequent dynamic evolution within the CPD has been characterized, the chemical effect of the CPD environment on its accreted material has only begun to be investigated in detail recently. Energy released from forming giant planets has been shown to heat the surrounding protoplanetary disk area (Montesinos et al., 2015; Cleeves et al., 2015; Szulágyi, 2017; Szulágyi & Mordasini, 2017), causing chemical processing to occur in the surrounding gas just after giant planet formation is complete (Cleeves et al., 2015). However, heating from the growing central planet could also cause chemical processing of the surrounding gas and solids within the circumplanetary disk. While some studies have touched on chemical processing of gas and solids in the circumplanetary disk, these studies did not take into account detailed dynamics of gas and solids (e.g. Prinn & Fegley, 1981; Mousis et al., 2002; Mousis & Gautier, 2004; Mousis & Alibert, 2006; Oberg et al., 2022, 2023) expected to occur within the CPD (e.g. Tanigawa et al., 2012, 2014; Szulágyi et al., 2016; Szulágyi, 2017) and instead focused on static chemical processing of material. Additionally, these studies focused on disks that were not satellite forming and hence did not simulate chemical processing under CPD conditions that allow for the formation of moons, making this area rife for study.

Formation does not directly translate into a final planetary environment, however. While planet formation does serve to set the initial composition and conditions of a planetary body, each planet undergoes further processing which can serve to alter the habitability of a current

day planet. While studying how planet formation can affect the composition of planetary bodies, I also became interested in how these initial conditions after planet formation, such as dynamical and orbital parameters, affected the potential for life to originate on Earth-sized planets. Spurred by this interest, I set out to investigate these topics and report the results of my work in this thesis.

1.3 Chapter Summaries

The remainder of this thesis is laid out as follows:

In **Chapter 2**, I explore the effects of a luminous planetary core on local, volatile-rich solids in the protoplanetary disk, both those that accrete and those that have close fly-bys to the core. I find that a critical transition occurs where very hot (rapidly accreting) cores drive off volatiles prior to accretion, while cool cores (slowly accreting) are able to inherit volatile rich solids. These results have implications for the potential mechanisms and location of Jupiter's formation. This chapter is based on Barnett & Ciesla (2022).

In **Chapter 3**, I model chemical reactions from Prinn & Fegley (1981) and Oberg et al. (2022, 2023) in CPDs whose dynamical evolution and physical conditions would allow for the formation of large, regular icy satellites to assess the production of molecules that may serve as carriers of biocritical elements or as antifreeze agents that help expand the conditions under which liquid water can exist on cold bodies. I also simulate the accretion history of growing satellitesimals to determine where growth occurs in the CPD and what percentage of solids incorporated by growing satellites may contain chemically altered material. The results from this study suggest that while refractory carbon and nitrogen species can be produced within the CPD, solids accreted by forming satellites are characterized by the chemical composition of solids inherited from the protoplanetary disk and are not strongly influenced by the chemically altered solid compositions.

In **Chapter 4**, I model and analyze the effect that moderately high planetary obliquity has on planetary oxygenation potential. This effect is compared with the effect of chang-

ing the inventory of phosphate (PO_4^{3-}) and changing the ocean remineralization depth on planetary oxygenation potential. My results suggest that moderately high-obliquity planets have higher potential for biospheric oxygenation due to a combination of increased photosynthetic oxygen production and decreased oceanic oxygen solubility in comparison to their low-obliquity counterparts. Additionally, these results have implications for the evolution of complex life on planets with higher obliquity than Earth. This chapter is based on Barnett & Olson (2022).

Finally, **Chapter 5** concludes with final thoughts on future directions for the field and potential areas of inquiry to explore.

CHAPTER 2

THERMAL PROCESSING OF SOLIDS ENCOUNTERING A YOUNG JOVIAN CORE

2.1 Chapter Summary

Jupiter's enhancement in nitrogen relative to hydrogen when compared to the Sun has been interpreted as evidence that its early formation occurred beyond the N_2 snowline ($\sim$ 20-40 AU). However, the rapid growth necessary to form Jupiter before the dissipation of the solar nebula would lead to the forming planet's core reaching very high temperatures (>1000 K), which would lead to it warming its surroundings. Here, we explore the effects of a luminous planetary core on the solids that it ultimately accretes. We find that a critical transition occurs where very hot (rapidly accreting) cores drive off volatiles prior to accretion, while cool cores (slowly accreting) are able to inherit volatile rich solids. Given Jupiter's nitrogen enrichment, if it formed beyond the N_2 snowline, its core could not have accreted solids at a rate above 10^{-10} $M_\odot$ yr^{-1}. Our results suggest that either Jupiter formed in more distal regions of the solar nebula, or nitrogen loss was suppressed, either by its incorporation in more refractory carriers or because it was trapped within ices which devolatilized at higher temperatures.

2.2 Introduction

The Galileo and JUNO missions have given important insight into the properties of Jupiter and the conditions under which it formed. Specifically, the Galileo mission provided the first in-situ look into the composition of Jupiter's atmosphere, finding that volatile species such as Ar, Kr, Xe, C, N, and S were uniformly enriched up to four times relative to solar abundances, with the following JUNO mission suggesting the same is true for O (Niemann et al., 1996; Folkner et al., 1998; Owen et al., 1999; Atreya et al., 1999, 2003; Li et al., 2020). As Jupiter's atmosphere is largely expected to be derived directly from the solar nebula, the gas is expected to reflect the solar abundance of elements or be deficient in particular elements as they freeze out beyond molecular snowlines and are accreted into the core (e.g. Öberg et al., 2011b). Thus, observed enrichments must be sourced from solids as

frozen-out elements can easily be added independently of hydrogen and helium, which remain predominately as gaseous H_2 and He under all conditions expected within a protoplanetary disk. However, to be uniformly enriched in all other elements, solids must have formed at much colder temperatures than expected at Jupiter's current distance from the Sun ($\sim$5.2 AU) to contain all of the volatile species at their observed abundances (e.g. Pollack et al., 1996; Owen et al., 1999).

One possible way to reconcile these observations, suggested by Owen et al. (1999), would be if Jupiter's formation was initiated far beyond its current orbital location, where temperatures were low enough to support solids with a nearly solar composition (all elements present at their solar abundance except H and He). The planet would then migrate inwards over time as a result of torques that arise from gravitational interactions with the disk (e.g. Nelson et al., 2000; Alibert et al., 2005; Paardekooper & Johansen, 2018). In fact, it is worth noting that the migration of Jupiter from further distances than where it is found now is consistent with the capture of the Jupiter Trojans and preservation of their high inclinations (Pirani et al., 2019).

It is this framework that allowed Bosman et al. (2019) and Oberg & Wordsworth (2019) to argue that Jupiter, or at least its core, formed beyond the solar nebula's N_2 snow line which is estimated to have been tens of astronomical units from the Sun. As nitrogen is among the most volatile elements, including even the majority of noble gases (Oberg & Wordsworth, 2019), essentially all other elements would be frozen out beyond the N_2 snowline, leaving solids in this region with a solar mix of elements. Accretion of these solids would then result in uniform elemental enrichment in the planet.

Formation of giant planets at these extreme distances from the Sun is difficult within traditional core accretion models as the planetary growth timescale would exceed the typical lifetime of protoplanetary disks (e.g. Pollack et al., 1996; Hubickyj et al., 2005). More rapid formation, however, is possible in the context of pebble accretion (e.g. Lambrechts & Johansen, 2012; Levison et al., 2015) where solid mass is delivered by small solids whose

dynamics are controlled largely by their interactions with the gas. Accretion of these small solids can lead to the rapid production of massive cores in protoplanetary disks, initiating planet formation very early in disk history. In fact, models have shown that a 10 $M_\oplus$ solid core can grow at 100 AU in less than 1 Myr, and even faster at the shorter distances where the N_2 snowline is expected to reside (Lambrechts & Johansen, 2012).

As giant planets require rapid growth, it is important to consider the energy balance that occurs during accretion, as planets will get hot and radiate heat to the surrounding environment. Models of Jupiter's formation suggest that the planet reached luminosities exceeding 10^{-7} $L_\odot$ throughout its growth and may have reached 10^{-4} $L_\odot$ at times (D'Angelo et al., 2021). Radiation escaping from the growing planet may have a significant effect on the local disk environment. For example, Cleeves et al. (2015) showed that an accreting gas giant could release enough energy to volatilize ices in the area around their orbits, offering a means of detecting these planets in a disk.

The situation considered by Cleeves et al. (2015) focused on the late-stage growth of a Jupiter-mass planet that had already opened a gap in the surrounding protoplanetary disk. However, a rapidly growing core early in its evolution may also release enough energy to heat its surface by thousands of Kelvin. In fact, temperatures at the surfaces of pebble-accreting cores can be sufficient to vaporize silicates before they reach the surface (e.g. Johansen et al., 2021). In the case of Jupiter forming far from the Sun, if the core was too luminous, nitrogen ice may have devolatilized prior to accretion, preventing the growing core from incorporating this element despite forming beyond the N_2 snow line.

As such, in this work we investigate the effect of an accreting giant planet core on the solid material it encounters in its protoplanetary disk and implications for volatile enrichments that could occur during this stage of growth. The next section (Section 2.3) details the modeling framework used to track the dynamical, thermal, and chemical evolution of pebbles approaching such a core. Section 2.4 presents the complete histories for particles encountering the core at various stages throughout its growth. We discuss significant trends in our findings

in Section 2.5 and our conclusions are outlined in Section 2.6 along with discussion for the implication for volatile accretion by growing giant planets.

2.3 Methods

In our model, we simulate a protoplanetary disk with a young planetary core on a circular orbit around a solar-mass star. The core has low enough mass ($\leq 5 M_\oplus$) that it has not opened a gap in the disk and is fully embedded in the gaseous disk. Solid particles drift inwards from the outer regions of the disk under the influence of gas drag, with some encountering the growing core. Not all encounters are equal, however, and depend on the details of the core and particle trajectory. To investigate the effect on the nitrogen inventories of accreting solids, we simulate this dynamical evolution, the corresponding thermal evolution, and the resulting chemical evolution of these bodies.

2.3.1 Dynamical Evolution

We simulate the dynamical evolution of solids of various sizes in a protoplanetary disk as they move under the combined gravitational effects of the star and growing planetary core using a method similar to Tanigawa et al. (2014). That is, we consider a Cartesian coordinate frame that is centered on and co-rotating with the planet. The x-axis is defined by the line connecting the core and the star, while the y-axis is oriented in the direction of motion of the planet. The corresponding equations of motion for the particles (focusing on the disk midplane and ignoring vertical motions) are given by:

$$\ddot{x} = -\left(\frac{GM_\odot(x+a)}{\sqrt{(x+a)^2+y^2}^3} + \frac{GM_{core}x}{\sqrt{x^2+y^2}^3}\right) + 2\Omega_0\dot{y} + \Omega_0^2(x+a) - \frac{C_d\rho_g\pi r_p^2\Delta v_{p,g}(\vec{v_{px}} - \vec{v}_{gx})}{2m_p} \tag{2.1}$$

$$\ddot{y} = -(\frac{GM_{\odot}}{\sqrt{(x+a)^2+y^2}^3} + \frac{GM_{core}}{\sqrt{x^2+y^2}^3})y - 2\Omega_0\dot{x} + \Omega_0^2 y - \frac{C_d\rho_g\pi r_p^2\Delta v_{p,g}(\vec{v_{py}} - \vec{v}_{gy})}{2m_p} \quad (2.2)$$

where G is the gravitational constant, $M_{\odot}$ is stellar mass, M_{core} is core mass, m_p is the mass of the particle, ρ_g is the surrounding gas density, Ω_0 is the orbital frequency of the core around the central star, C_d is the Epstein drag coefficient, $\vec{v_p}$ and $\vec{v}_g$ are the velocities of the particles and gas respectively, and $\Delta v_{p,g}$ is the magnitude of $\vec{v_p} - \vec{v}_g$. The last term of each equation represents the acceleration from gas drag (Tanigawa et al., 2014). Note that while we perform the calculations in the co-rotating reference frame, all figures displayed in this paper are presented in a reference frame centered on the Sun for ease of analysis and interpretation.

The particles in our models are initially defined by their Stokes numbers, St, where:

$$St = \frac{r_p\rho_p v_{th,i}}{\rho_{g,i}\Omega_i} \quad (2.3)$$

and is used as a proxy for the radius (Stokes numbers change as they migrate into new environments). Particles are assumed to be primarily icy, with a density (ρ_p) of 1000 kg m^{-3}. For this work we consider initial St = 0.01, 0.1, 1.0, or 10.0, but generalize our results to other sizes further below.

Our model focuses on particle movement at the disk midplane and ignores vertical motions. As we ignore the effects of turbulence here, we expect most particles to be located around the disk midplane; the settling time for particles considered here are ∼100-10,000 years, which is a short time compared to the lifetime of the disk. If particles were not fully settled by the time they approach the growing core, it is possible that they could escape an encounter, and avoid accretion. As our focus is on those particles that are ultimately accreted by the growing core, and accretion requires the particles to be near the plane around the midplane, ignoring particles at higher altitudes will not change our conclusions.

The physical structure of the protoplanetary disk is taken from Oberg & Wordsworth

(2019):

$$\Sigma_r = 15,000 \left(\frac{r}{1 \text{ au}}\right)^{-3/2} \text{ kg m}^{-2} \tag{2.4}$$

$$T_b = 140 \left(\frac{r}{2 \text{ AU}}\right)^{-0.65} \text{ K} \tag{2.5}$$

where r is the distance from the star. Midplane gas densities are then found from:

$$\rho_g = \frac{\Sigma_r}{\sqrt{2\pi}H} \tag{2.6}$$

where H is the isothermal scale height:

$$H = \frac{c_s}{\Omega_K} \tag{2.7}$$

where Ω_K is the local Keplerian frequency and c_s is the sound speed.

The sound speed is calculated using the equation:

$$c_s = (kT/\mu m_H)^{1/2} \tag{2.8}$$

where k is the Boltzmann constant, T is the temperature, m_H is the mass of hydrogen, and μ is the mean molecular weight of the protoplanetary gas which we take to be 2.3.

We consider core masses ranging from 0.5-5 $M_\oplus$. The radius of the solid core is found from the scaling laws for planetary mass-radius developed in Valencia et al. (2006) for Super Earths (1-10 $M_\oplus$):

$$R_{core} = R_\oplus (M_{core}/M_\oplus)^{0.27} \tag{2.9}$$

In addition to the solid component, a growing core will gravitationally attract surrounding gas in the disk to form a planetary envelope. The radius of this planetary envelope is given by Chambers (2017):

$$r_{env} = min[\frac{r_H}{4}, r_B] \tag{2.10}$$

Here, r_H is the core's Hill radius ($r_H = a(\frac{M_{core}}{3M_\odot})^{1/3}$), and r_B is the core's Bondi radius ($r_B = \frac{GM_{core}}{c_s^2}$). For low mass cores, the Bondi radius sets the outer extent of the envelope as it defines the location where gas becomes gravitationally bound to the core. As the Bondi radius grows at larger masses, however, the differential rotation of the disk becomes important in setting the core's envelope boundary. Lissauer et al. (2009) used 3D hydrodynamic simulations to show that gas beyond 25% of r_H will be sheared away from the planet due to this rotation, thus setting this location as the distance beyond which gas no longer remains bound to the core. At the orbital separations considered here, the planetary envelope boundary is defined by the Bondi radius for core masses 0.5-4 $M_\oplus$ and is 25% of the Hill radius for a 5 $M_\oplus$ core. Any particles that cross into this envelope-disk boundary are assumed to be accreted, delivering any volatiles they contain to the growing core.

We note that volatile delivery may be affected by planetary envelope recycling flows, as are found in planetary envelope hydrodynamic simulations (e.g. Lambrechts & Lega, 2017; Kurokawa & Tanigawa, 2018; Popovas et al., 2018; Johansen et al., 2021). In these simulations, gas flows within the planetary envelope hinder gaseous volatile delivery to the core as the desorbed volatiles may flow back out to the protoplanetary disk. As such, our results represent an upper limit on volatile delivery to the core.

2.3.2 Thermal Evolution

The temperatures that the particles reach in the disk will be set by the background environment through which they move and radiative heating from the growing core. The contribution from the core is set by the core's luminosity and the distance between the core and the particle. The core surface temperature is defined as:

$$L_{\text{core}} = 4\pi\sigma R_{\text{core}}^2 T_{\text{eff}}^4 \tag{2.11}$$

Ultimately, the luminosity of the growing core is set by the rate of mass accretion which varies over the lifetime of the core. To consider a plausible range of values, we define the luminosity by setting the surface temperature of the solid core to a value between 1000-3000 K; these values correspond to mass accretion rates of $1.5 \times 10^{-11}\,\mathrm{M_\odot yr^{-1}}$ to $1.19 \times 10^{-9}\,\mathrm{M_\odot yr^{-1}}$ and luminosities of $7.5 \times 10^{-8}\,\mathrm{L_\odot}$ to $6.13 \times 10^{-6}\,\mathrm{L_\odot}$ for a 1 $\mathrm{M_\oplus}$ core, all within the range expected from detailed models of Jupiter's growth (e.g. D'Angelo et al., 2021).

As the envelope is assumed to be in hydrostatic balance (Rafikov, 2006; Hori & Ikoma, 2011; Lambrechts et al., 2014; Venturini et al., 2015; Chambers, 2017), the rate of energy transfer is constant throughout the envelope, meaning the amount of energy passing into the surrounding nebula at the envelope boundary is equal to L_{core}. The physical structure of the envelope interior is complex, containing both a convective inner layer and radiative outer layer with varying optical depths (Hori & Ikoma, 2011; Venturini et al., 2015; Chambers, 2017). However, as we are only concerned with the blackbody temperature experienced by solids at the envelope boundary and we can consider the envelope in steady state, the interior temperature/pressure profiles of the planetary envelope are not necessary for us to calculate here. As such, we follow Rafikov (2006) and Lambrechts et al. (2014) by adopting the optically thin equation to calculate the solid blackbody temperature exterior to the envelope boundary.

We calculate the blackbody temperature of solids encountering the core using the equation [1]:

$$T_{\mathrm{BB}} = \left(\frac{L_{\mathrm{core}}}{16\pi\sigma r^2} + T_b^4 \right)^{\frac{1}{4}} \tag{2.12}$$

This treatment assumes that the solid instantaneously equilibrates with the radiation field of the core and ignores the diffusion of heat into the interior of the solid. However, given that we expect that the resulting desorption of molecules will occur from the surface

1. We also considered the effect of the optical depth in the disk by having the flux from the core decrease as it passed through the gas, but found this effect to be minor for the cases of interest

of the solids, such an assumption is justified.

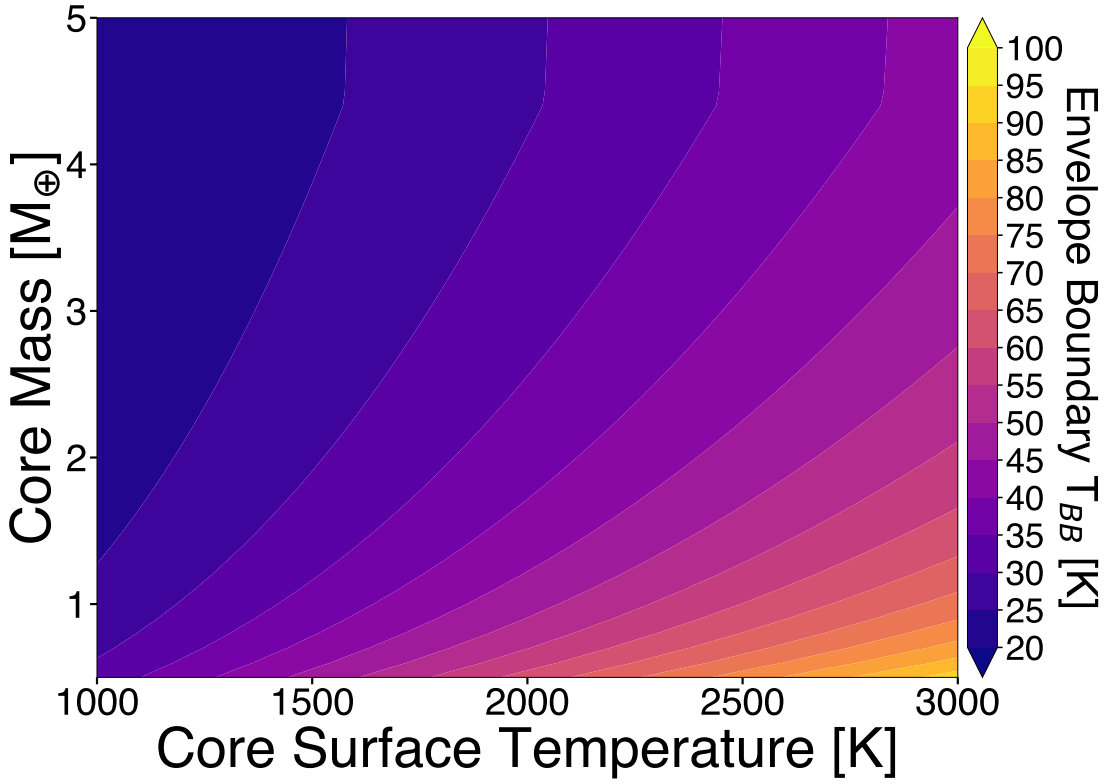

Figure 2.1: Blackbody temperature experienced by solids at the envelope boundary for the entire range of simulated core masses and core surface temperatures. Lower mass cores have smaller planetary envelope radii, resulting in solids coming in closer proximity to the core before accretion. Due to this closer proximity, solids experience higher blackbody temperatures before accretion. Core masses of 0.5 $M_\oplus$ lead to the highest solid blackbody temperatures at the envelope boundary for each simulated core surface temperature, while 5 $M_\oplus$ core masses result in the lowest solid blackbody temperatures.

Blackbody temperatures for solids at each core mass envelope boundary for the range of core surface temperatures are displayed in Figure 2.1. For the range of core masses and core surface temperatures we consider, the resulting temperature enhancements felt by solids at the various cores' envelope boundaries range from ∼2K - 100K. The radius of the planetary core's envelope scales with core mass, which results in radiation emitted from the surface of larger cores having to travel farther to reach the respective envelope boundaries. This longer distance traveled results in lower blackbody temperatures experienced by solids at the core

boundary of larger mass planets.

2.3.3 Chemical Evolution

As particles are warmed in the disk, species in their ice mantles may begin to volatilize. This occurs via thermal desorption at a rate described by the Polanyi-Wagner relation (e.g. Hollenbach et al., 2008; Piso et al., 2015):

$$k_{desorption,i} = \nu_i e^{\frac{E_i}{T_{BB}}} [\mathrm{s}^{-1}] \tag{2.13}$$

Where $\nu_i = 1.6{\times}10^{11}\sqrt{(E_i/k)(m_H/m_i)}\ \mathrm{s}^{-1}$ is the vibrational frequency of a given species and E_i is its corresponding binding energy. As our focus here is on the nitrogen content of the solids, we consider the two most abundant carriers, N_2 and NH_3 (Öberg et al., 2011a; Pontoppidan et al., 2019). N_2 is more volatile with a binding energy of 1050K (∼15-25K freeze-out temperature, Bisschop et al., 2006; Fayolle et al., 2016), while NH_3 desorbs at higher temperatures with a binding energy of 3800K (Oberg & Wordsworth, 2019). We set the initial abundances relative to hydrogen of N_2 and NH_3 as 3×10^{-5} and 7×10^{-6}, respectively (Oberg & Wordsworth, 2019).

In our model, we only consider loss of molecules from the particles' ice mantles; we ignore freeze-out as the particle sizes we consider (Stokes numbers >0.01) have sufficient drift velocity such that desorbed molecules are unlikely to freeze back out onto the solid before it has drifted away. That is, freeze-out timescales around the disk midplane are on the order of ∼1 year, while solids and gas have relative velocities of $\sim 1\ \mathrm{m\ s}^{-1}$ or larger (e.g. Weidenschilling, 1977), allowing the solids to drift away from any desorbed molecules before they freeze-out again. Further, desorbed molecules would likely freeze-out on the smallest solids present (micron-sized fine dust with St $\sim 10^{-4}$) as these particles provide the greatest total surface area. The desorption of molecules from the ice mantle is calculated using a first order Euler method, using the rate given in Equation (2.13). We ignore other forms

of molecular desorption or destruction (via UV, X-rays, or cosmic rays) as we are focused on regions around the disk midplane where fluxes of energetic particles and photons are expected to be low.

2.4 Results

In order to sample the range of dynamical encounters between particles and the growing core, we simulated the evolution of 360 different particles for each set of conditions (particle Stokes number, core semi-major axis, core mass, and core surface temperature). These particles began on orbits that were 1-2 AU greater than the semi-major axis of the planet, distributed as a ring around the star and separated by 1 degree from one another. The particles were then allowed to drift inwards over time due to the effects of gas drag, accounting for the gravitational effects of the growing core and central star. Simulations were run for $\sim 10^4$ years of model time, sufficient enough for particles to either be accreted by the core or drift inside of the core's orbit such that continued encounters would not occur.

In each simulation, only a small fraction (<15%) of the drifting particles were accreted by the core. The fraction of particles accreted, or "accretion efficiency", is shown in Figure 2.2 as a function of core mass and Stokes number. The lowest accretion efficiency for all cases is seen in St=1 particles where, depending on core mass, 0.8-2.5% of particles are accreted by the core. This occurs because these are the most rapidly drifting particles in the disk, migrating through the range of radial distances where they may have a close (accretionary) encounter with the growing core in the least amount of time. Accretion efficiencies increase as one moves away from St=1 particles as smaller solids remain in the vicinity of the core's orbit for longer periods of time, increasing the likelihood of a close encounter.

The accretion efficiencies found in our model are consistent with trends and averages found in pebble accretion studies from Lambrechts & Johansen (2014) and 2D pebble accretion models from Ormel (2017), but the details of accretion efficiency will vary with initialized particle population and model set-up. Our model simulates the extended dynamical paths

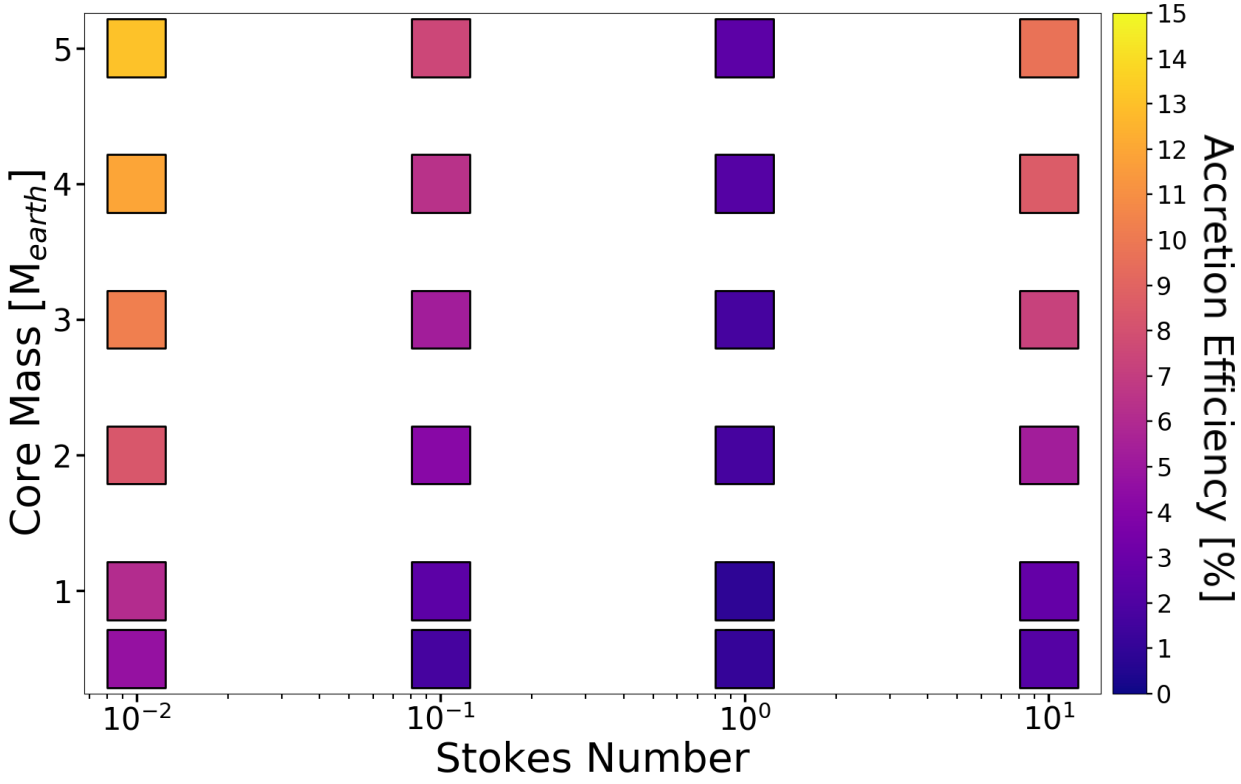

Figure 2.2: Accretion efficiency for particles initialized with all combinations of model core mass and Stokes number. Core/star orbital separation is fixed at 40AU. Accretion efficiency is highest for smallest Stokes number particles (St = 0.01), followed by the highest Stokes number particles (St = 10). Accretion efficiency is lowest for St = 1 particles.

of particles which are initialized outside the core's orbit and encounter the core as they drift inwards. This provides a more realistic picture of the geometries of pebble trajectories for pebbles that encounter the core. Other models evaluating accretion efficiency take a different approach, and instead inject pebbles close to the planetary core (e.g. Popovas et al., 2018). This can lead to different trends in accretion efficiency with particle size, as disparate pebble population locations lead to different encounter geometries.

Figure 2.3 shows the paths followed by all accreted particles in the St=0.01, M_{core}=3$M_{\oplus}$ case for a core orbiting at 40 AU with a surface temperature of 3000K. We display particle trajectories in the area directly adjacent to the core as this is where the particles approach close enough to experience heating, although, again, we simulate particle dynamics through the entire protoplanetary disk. While all shown particles are eventually accreted, we note that their accretion trajectories fall into two categories: *directly* accreted particles which impact the core soon after crossing its Hill radius, and *indirectly* accreted particles that enter and leave the Hill sphere only to return again before accretion. The enhanced accretional cross section of the core compared to its physical cross-section is due to the gas drag-regulated velocities of the drifting solids that allows pebble accretion to be so efficient as a means of growth (Lambrechts & Johansen, 2012, 2014; Kretke & Levison, 2014; Chambers, 2014; Levison et al., 2015; Johansen & Lambrechts, 2017).

Figure 2.4 shows the variation in thermal and chemical evolution that different particles may experience as a result of their close encounter with the core. Here we show two different particle trajectories (Figure 2.4), one directly accreted particle from Figure 2.3 (white line in Figure 2.4a) and one indirectly accreted particle (dark blue line in Figure 2.4a). The directly accreted particle's temperature monotonically increases on its way to being accreted, reaching values near 50K before entering the core's envelope (Figure 2.4b). In this case, the particle's N_2 ice completely desorbs from the ice mantle outside of the core's envelope but leaves NH_3 ice, allowing just 20% of the original nitrogen inventory to be accreted by the core (Figure 2.4c).

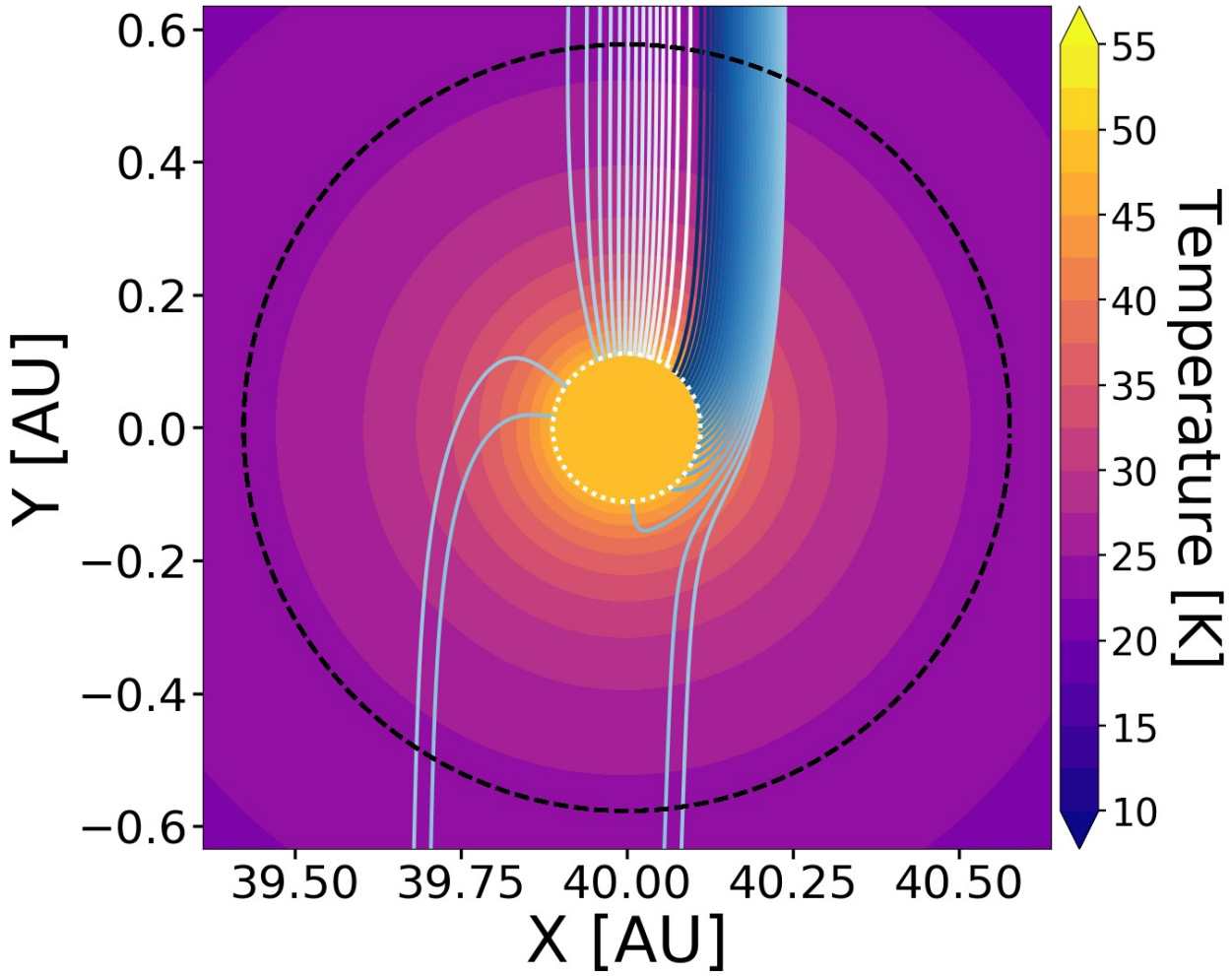

Figure 2.3: Particle trajectory lines (solid white to blue lines) from particles started at different azimuthal locations over-plotted on the temperature contour map (colorbar) describing the temperature environment of the protoplanetary disk near the planetary core. This model features a 3 $M_{\oplus}$ planetary core located 40AU from the central star with a surface temperature of 3000K. Particle trajectories are for all accreted particles with St = 0.01. Black dashed and white dotted lines mark the Hill radius and envelope boundary, respectively.

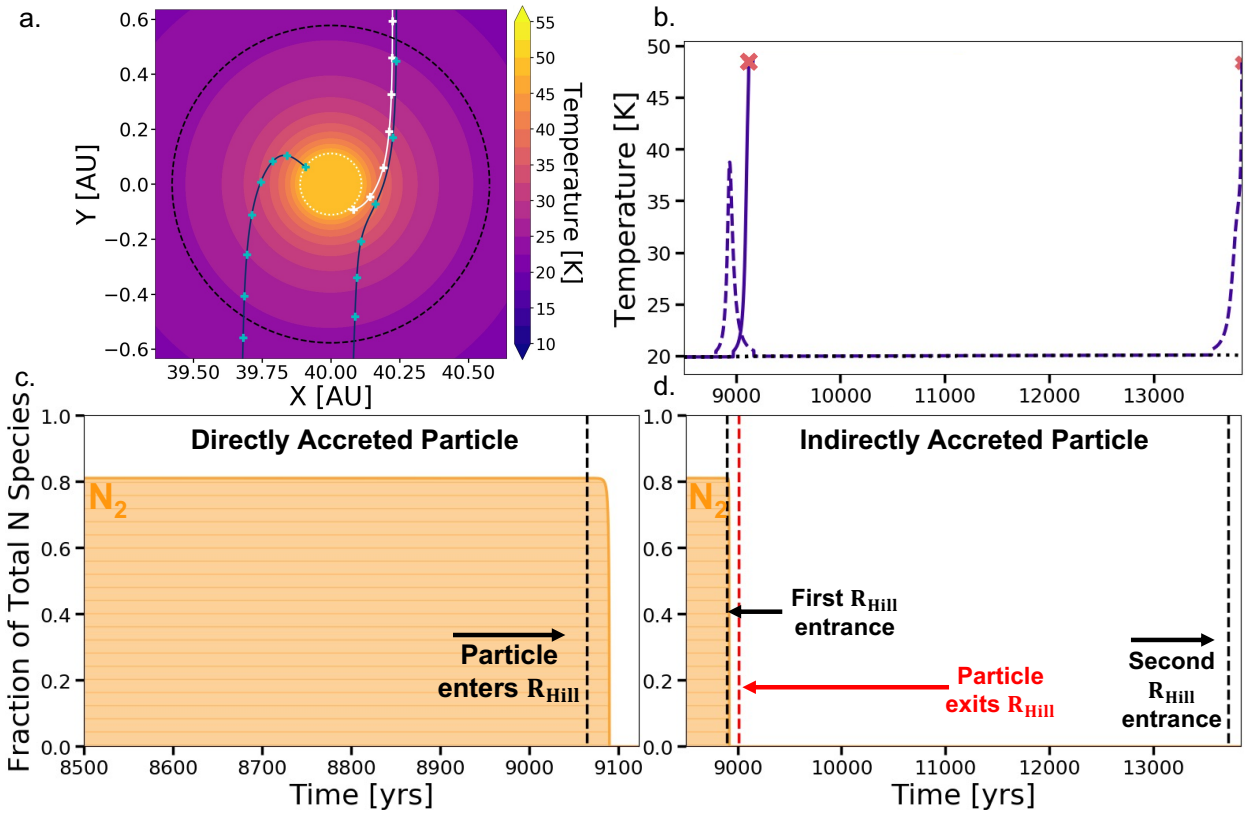

Figure 2.4: Particle trajectories (a), thermal (b), and chemical evolution (c and d) comparison for particles with St = 0.01 around a 3 $M_\oplus$ core at a = 40AU and core surface temperature of 3000K. The indirectly accreted particle (solid blue line in panel a, and dashed line in panel b) and directly accreted particle (solid white line in panel a, solid line in panel b) are identical except for different azimuthal starting locations. We show the thermal and chemical evolution starting from 8500 years into the particles' evolution, as this is when the particles first encounter the core. Crosses (panel a) denote 10 year time-points for the directly accreted particle track (white, 9060-9120 years) or 20 year time-points for the indirectly accreted particle tracks (cyan, 8900-9000 years on right-hand side and 13710-13850 years on left-hand side). Pink x's (panel b) correspond to time of accretion for each particle and represent the endpoints of panel c and d plots.

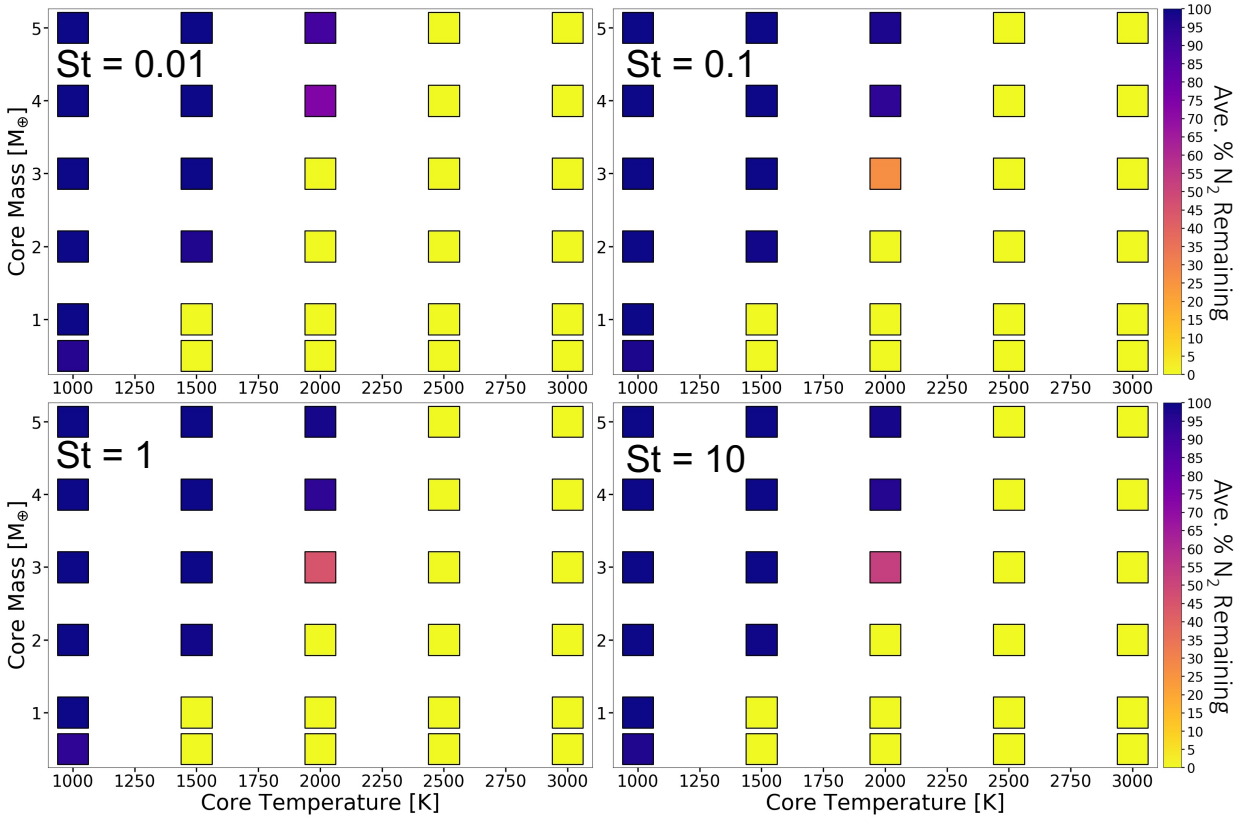

Figure 2.5: Percent particles with N_2 as the dominant nitrogen species (colorbar) for models initialized with all combinations of core mass and core temperature. Subplots are results for particles with Stokes numbers 0.01 (upper left), 0.1 (upper right), 1 (lower left), 10 (lower right). The planet was assumed to orbit at 40 AU in these simulations.

The indirectly accreted particle is similarly warmed during its initial close passage to the core, reaching temperatures of ∼40K before moving back outside the core's Hill radius, cooling as it migrates away. While this temperature is cooler than that reached by the directly accreted particle, it is sufficient to drive off the N_2 ice in the particle's mantle (Figure 2.4d). Interestingly, upon exiting the Hill sphere of the embryo, this particle would be available for incorporation into other planetesimals or cores that may be nearby, delivering nitrogen-depleted solids to these growing bodies. In the absence of such an event, the particle returns to the core and is accreted, also delivering a sub-solar amount of nitrogen to the growing planet.

With our simulated collection of trajectories, thermal histories, and subsequent nitrogen

inventory evolution, we can then determine how much of this element is delivered to a growing core for the conditions considered. These results are displayed in Figure 2.5, which shows the average percentage of remaining N_2 ice on accreted particles for all core mass-temperature and particle Stokes number combinations considered. In all cases, we see that cores with temperatures of 2500K or higher are too luminous for N_2 ice to be retained; particles experience significant heating before accretion and thus would be unable to enrich a growing core in this element. At temperatures of ∼1000K or lower, the low amount of energy radiated from the core does not significantly warm incoming pebbles before accretion, allowing them to retain their full nitrogen inventories.

Intermediate to these temperature regimes, we see a transition occur in the 1500K-2000K runs where the retention of N_2 ice begins to differ based on the sizes of the particles and the core mass. More specifically, as the core mass decreases, less N_2 ice is retained by the accreting particles. This effect arises because both the Bondi radius and Hill radius of the core, and thus the size of its envelope, depend on the core's mass. Particles are considered accreted when they pass the envelope-disk boundary, thus larger envelope radii translate to lower solid blackbody temperatures at the boundary as particles are relatively farther from the core when they are accreted.

Though this temperature difference can be seemingly minor between core masses (on the order of ∼2-10K difference between core masses 2 $M_\oplus$ to 3 $M_\oplus$), this can lead to significant differences in volatile loss given the exponential dependence of desorption rates on temperature. Additionally, as particles decrease in size (Stokes number), a smaller fraction retains their N_2 when compared to larger pebbles (see 3 $M_\oplus$ core model for all Stokes numbers in Figure 2.5). This is due to two effects: (1) larger particles are less coupled to the gas and thus fall through it at faster rates than the small particles where drag slows down their accretion, and (2) larger particles have larger inventories of ice and thus take longer to lose their nitrogen than the small particles. Both of these effects result in greater volatile loss from smaller particles, a trend that would continue to smaller particles than those considered

here.

The dependence of volatile loss on core mass and particle size is best captured in the T_{core} = 2000K runs in Figure 2.5. We see that solids approaching very low mass cores (0.5-2 $M_\oplus$) experience full stripping of their frozen N_2, while higher mass cores (4 and 5 $M_\oplus$) fully maintain all N_2 for all particle Stokes numbers. However, solids encountering the 3 $M_\oplus$ core experience progressively more N_2 stripping as the pebble Stokes number decreases. This transition occurs because the temperature experienced by solids at the 3 $M_\oplus$ envelope boundary is fairly moderate at $\sim$ 33K for a core surface temperature of 2000K, thus the amount of time each solid spends in the vicinity of the core before accretion has a significant effect on its N_2 inventory.

2.5 Discussion

Our results indicate that the surface temperature (luminosity) of a growing core will be the primary factor in determining whether N_2 ice is retained and delivered during accretion. Additionally, we find that the presence of a planetary envelope is required for volatile delivery as the envelope increases the effective accretionary boundary radius by a factor of $\sim$500-2500. Solids approaching the core are then accreted at much larger radii from the core and as such reach much lower temperatures before accretion than they would otherwise. In the absence of an extended envelope, significant warming would occur prior to accretion, leading to volatile-poor planets.

Cores with temperatures of $\lesssim$1500K will readily accrete all the nitrogen that its feed stock is able to carry, while cores with temperatures of $\gtrsim$2500K would be depleted in nitrogen. At temperatures between 1500-2000K, the nitrogen story is more nuanced, depending on the size of the core and the particles being accreted. As these second order effects become important at core temperatures of 1500-2000K, we define this as the transition point between when a solar inventory of nitrogen would be delivered to the core versus N-depleted solids, allowing us to constrain the conditions under which a growing giant planet core would inherit

a solar mix of this element. Given that the temperature of the core's surface is set by the accretion rate of solids, this transition point sets an upper limit on the accretion rate that would allow the chemical constraints inferred for Jupiter's formation to be met. To maintain a core temperature below this critical value, the mass accretion rate must satisfy:

$$\dot{M} \lesssim \frac{4\pi R_{core}^3 \sigma T_{core}^4}{G M_{core}} \tag{2.14}$$

For a 5 $M_\oplus$ core, this implies that $\dot{M} \lesssim 10^{-10}$ $M_\odot$ yr^{-1} to stay below T_{core} <2000 K. This value is in the range estimated for Jupiter's formation (>10^{-11} $M_\odot$ yr^{-1}), but suggests that some of the higher values (∼10^{-9} $M_\odot$ yr^{-1}) (Lambrechts & Johansen, 2012, 2014; D'Angelo et al., 2021) must be ruled out. Lower mass cores thus have even lower limits on the critical mass accretion rate needed to maintain frozen N_2 (Figure 2.1).

The core surface temperature where cores transition from being able to accrete volatiles at a given temperature versus being unable to do so will depend on the location in the disk where the core forms as the semi-major axis (a) also impacts the extent of the envelope ($r_H \propto a$ and $r_B \propto a^{0.65}$). Smaller semi-major axes would push the transition point to lower core temperatures as particles approach closer to the core before accretion and would therefore be exposed to higher radiation fluxes and reach higher temperatures. Thus, if Jupiter were to form closer to the Sun, the upper limit on the accretion rate would be even lower. For simulations at 30 AU, similar to those presented here, we found a transition temperature of ∼1500K for a 5 $M_\oplus$ core, which would limit accretion rates to below 7.5×10^{-11} $M_\odot yr^{-1}$.

This finding is important in considering the possibility that Jupiter formed closer to its current orbital separation. In discussing the Galileo probe data, Owen et al. (1999) offered another possible mechanism for Jupiter's atmospheric volatile enhancement, suggesting that temperatures at Jupiter's current orbit were much colder than previously believed. This idea was recently explored by Ohno & Ueda (2021), who suggested that a dust enhancement just inside of the water snow line could have led to a shadowing of Jupiter's orbit, vastly reducing

temperatures there. However, though decreasing the background temperature may allow N_2 ice to form in this location, forming Jupiter closer to its current orbital separation causes a dramatic increase in solid blackbody temperatures during accretion onto larger ($\geq 5M_\oplus$) core masses.

While for a $5M_\oplus$ core with T_{core} = 2000K at 40AU (the transition point for a $5M_\oplus$ core) the solid blackbody temperature is ∼29K at the planetary envelope boundary, moving that same core to 5AU increases the solid blackbody temperature to ∼78K, which would lead to incredibly rapid N_2 loss. We find that the transition point for such a core at 5AU now occurs around a temperature of 700K, corresponding to a mass accretion rate of $\sim 2.5 \times 10^{-12}\, M_\odot yr^{-1}$ and a core doubling time of $\sim 5 \times 10^6$ yrs. This formation time is likely too slow to form a sufficiently massive core before gas dissipation in the protoplanetary disk occurs, implying that forming Jupiter at 5AU with its atmospheric volatile enhancements would prove challenging if nitrogen is expected to be accreted by higher mass cores. However, as lower mass cores have envelope boundaries set by the Bondi radius, which in turn depends on the disk background temperature, shadowing would allow these lower mass cores to accrete nitrogen ice even at 5AU. While shadowing does potentially provide a mechanism for Jupiter to accrete nitrogen ice at 5AU during the early stages of core accretion (M_{core} <5 M⊕), the specifics of this scenario should be investigated in future work.

2.6 Conclusions and Summary

In this work, we have found that the luminosity of growing cores may be sufficient to drive off volatiles from solids before they are accreted by a forming planet. Thus, even if a given planet formed beyond a snow line in the disk, it may still fail to accrete the particular species that freezes out at that location. In other words, the chemical composition of a planet will not simply reflect the local environment where it formed but instead is set by a complex interplay of its formation location and its accretion history. Planets that form rapidly or experience rapid accretion rates will devolatilize solids to some degree before they are accreted. In

the case of Jupiter, the fact that its nitrogen abundance is uniformly enhanced with other volatile elements suggests it formed in a very cold environment and slowly enough to prevent loss of volatiles during accretion.

We note that elemental enhancements may be possible at higher mass accretion rates under certain circumstances. Here we considered accretion at 40 AU, but accretion further out in the disk, sufficiently beyond the snow line, may be conducive to retention of all volatiles. As discussed above, the extent of the core's envelope is proportional to either r_H or r_B, both of which increase with semi-major axis. This would lead to lower radiative fluxes emerging from the envelope for the same core temperatures considered here. This, combined with the cooler background temperatures at these locations, may allow volatiles to be retained more readily. Additionally, while our model assumes direct desorption of all molecules off the grain as temperatures rise, this may not be the case for nitrogen molecules in the solar nebula. Owen et al. (1999) posited that one mechanism of nitrogen delivery to a forming Jupiter could be through trapping of N_2 molecules in amorphous water ice. In this case, N_2 would only be lost when the surrounding water ice desorbs from the grain, but this occurs at much higher temperatures ($\sim$150-180K) than N_2 desorption. This mechanism may allow delivery of N_2 at higher core surface temperatures than the upper boundary characterized in our results. Further, the model considered here assumed steady-state (constant) accretion of solids by the core; if accretion is instead episodic, it is possible large amounts of mass could be delivered while the core remains relatively cool. These conditions should be considered in future studies.

Additionally, while this work focuses on evaluating the conditions under which nitrogen can be accreted by Jupiter in the solid phase, another potential mechanism for explaining volatile enhancement in Jupiter's atmosphere has recently been suggested by Schneider & Bitsch (2021). They propose that volatile enhanced gas generated as nitrogen ice-rich pebbles passed interior to the N_2 snowline could provide Jupiter's observed nitrogen enhancement. As the N_2 would be accreted in the gas phase, there would no longer be a constraint placed

on the growth rate of Jupiter's core.

The outcomes described here develop due to the paths that accreting solids take through the radiation field of a growing planet. In our work, we have not accounted for detailed changes in gas flow due to the gravitational influence of the core in its immediate vicinity as has been done in other studies (e.g. Okamura & Kobayashi, 2021). This could alter the trajectories of the grains and their exposure time to high radiation flux. However, given the exponential dependence of desorption rate on temperatures, this effect is likely minor in determining particle volatile loss, possibly slightly shifting the temperatures where secondary effects become important but not likely to change the general conclusions detailed here.

Giant planet accretional history will also be important when interpreting the elemental ratios observed in exoplanet atmospheres. One of the primary observations to be carried out by the James Webb Space Telescope will be the determination of C/O ratios in the atmospheres of giant exoplanets. Given that carbon and oxygen are expected to be present across a number of molecular carriers with a wide range of volatilities (e.g. Li et al., 2021), these elements may be driven off to varying degrees depending on their dominant molecular carrier in the protoplanetary disk and accretionary history. This would allow for the planet to inherit elemental ratios that differ significantly from its host star. Such possibilities were motivated by early analyses of WASP 12b observations (e.g. Ali-Dib et al., 2014; Madhusudhan et al., 2011, 2014; Öberg et al., 2011b) which investigated how the formation location or migration of the planet through its protoplanetary disk was related to the planet's atmospheric composition. Based on the results presented here, mass accretion rate will also play a role in setting the composition of a planet and the apparent evolution of a planet relative to its host star, and must be considered in interpreting future observations of giant planet compositions.

CHAPTER 3

PRODUCTION AND ACCRETION OF REFRACTORY CARBON AND NITROGEN-BEARING MOLECULES IN SATELLITE-FORMING CIRCUMPLANETARY DISKS

3.1 Chapter Summary

A subset of icy moons believed to harbor subsurface oceans within our solar system have been identified as potential homes for extraterrestrial life. However, the presence of liquid water does not ensure that a planetary body contains the necessary biocritical elements to form the building blocks of cellular life (DNA and proteins). Instead, this biocritical element inventory is highly dependent on the composition of material that formed the satellite. It is unclear whether the material composition within the circumplanetary disk (CPD) is set by inheritance from the protoplanetary disk or by subsequent chemical processing once material is incorporated into the CPD. While work has been done to characterize chemical processing within CPDs, the birthplaces of regular satellites, these models assume physical conditions that may not be conducive to satellite growth. In this work, we model the production of refractory carbon and nitrogen species (carbon and nitrogen molecular carriers that freeze out above 40K, specifically CH_4, CO_2, and NH_3) from accreted protoplanetary disk material within two satellite-forming CPDs and simulate the subsequent accretion of these produced species by forming satellitesimal seeds. We find that while some refractory carbon and nitrogen species (CO_2 and NH_3) are effectively produced within these satellite-forming CPDs, satellitesimals are unable to efficiently accrete these locally produced refractory species. Hence, in order for forming satellites to support life, satellites would need to be supplied with refractory carbon and nitrogen species directly from the protoplanetary disk.

3.2 Introduction

As the hunt for the first sign of extraterrestrial life continues, subsurface ocean-bearing icy moons orbiting the giant planets of our solar system have become central in this search. These subsurface oceans would provide the necessary liquid water for life to originate and evolve, making these moons prime targets for further study (e.g. Council et al., 2012; Bayer et al., 2015). However, molecular sources of biocritical elements such as nitrogen, carbon,

and phosphorus are also necessary (e.g. Redfield, 1942, 1963) for the formation of life. While these elements were naturally delivered to Earth during its formation (e.g. Chyba et al., 1990; Marty, 2012; Bergin et al., 2015; Kitadai & Maruyama, 2018; Trigo-Rodríguez et al., 2019), icy moons are formed under conditions that likely varied dramatically from Earth's formation, making the abundances of biocritical elements on these bodies uncertain.

Some icy satellites are descrbined as regular satellites of the giant planets they orbit due to their coplanar, prograde orbits (e.g. Europa, Titan, and Ganymede; Morrison & Cruikshank, 1974; Peale, 1999). These moons formed through the accretion of solids in a circumplanetary disk (CPD) around a central giant planet during or at the end of the runaway gas accretion stage of the planet's formation (e.g. Prinn & Fegley, 1981; Canup & Ward, 2002; Alibert et al., 2005; Canup & Ward, 2006; Peale, 2007; Canup & Ward, 2008; Ward & Canup, 2010; Sasaki et al., 2010; Szulágyi et al., 2014, 2016; Szulágyi, 2017; Shibaike et al., 2017; Batygin & Morbidelli, 2020). In this formation scenario, the composition of satellites formed within a CPD will be determined either by the composition of materials inherited from the protoplanetary disk, by chemical processing that occurs within the CPD environments, or by a combination of the two. However, it is currently unclear to what extent each material source contributes to satellite composition.

Chemical processing of material incorporated into the CPD may be driven by the differences in the CPD environment vs. the local protoplanetary disk. CPDs create a region around their host planets with much higher densities than the local protoplanetary disk (e.g. Coradini et al., 2010). Additionally, CPD temperatures are predicted to be much higher than in the local protoplanetary disk due to viscous heating and irradiation from the hot, growing central planet (e.g. Ward & Canup, 2010; Szulágyi & Mordasini, 2017; Shibaike et al., 2019; Batygin & Morbidelli, 2020). Thus, material incorporated into a CPD has the potential to be chemically processed within this new environment, yielding solids that would be compositionally distinct from those within the protoplanetary disk.

Within the protoplanetary disk, the main carriers of carbon and nitrogen are expected to

be CO and N_2 (Lewis & Prinn, 1980; Beuther et al., 2014; Cleeves et al., 2016, 2018; Pontoppidan et al., 2019; Anderson et al., 2021), which are volatile species with very low freeze-out temperatures (∼15-20K). Lewis & Prinn (1980) investigated potential chemical processing of CO and N_2 within protoplanetary disks, finding that though equilibrium chemistry predicted the conversion of CO and N_2 into CH_4 and NH_3 (species with higher freeze-out temperatures of 40K and 80-100K, respectively Bosman et al., 2018; Oberg et al., 2023), respectively, these reactions were kinetically inhibited due to their long reaction timescales. Hence, in the protoplanetary disk, the majority of carbon and nitrogen species are primarily in the gas phase and are unable to be delivered to growing solids except for those very far from the central star.

In contrast, Prinn & Fegley (1981) theorized that chemical processing stemming from a dense and cold CPD would result in the main carbon and nitrogen species within the disk being comparatively more refractory carriers (CH_4 and NH_3 with freeze-out temperatures of $\sim$ 40K and 80-100K, respectively Bosman et al., 2018; Oberg et al., 2023) than in the parent protoplanetary disk. While the specific reactions Prinn & Fegley (1981) considered were kinetically inhibited within the protoplanetary disk due to long reaction timescales (Lewis & Prinn, 1980), the higher densities of the CPD allowed for much more rapid conversion of CO and N_2 to CH_4 and NH_3.

If the main molecular species bearing carbon and nitrogen in CPDs are comparatively more refractory (species that freeze out at higher temperatures such as CO_2, CH_4, and NH_3, here-after referred to as refractory carbon and nitrogen species) than those predicted to be dominant in the protoplanetary disk, they would freeze out more readily onto solids. This would increase the abundances of carbon and nitrogen that could be delivered to forming satellites at the higher temperatures expected in CPDs. Additionally, some refractory carbon and nitrogen species such as CH_3OH and NH_3 could work to widen the range of conditions over which subsurface liquid water oceans can be maintained on icy moons as they can act as potent anti-freeze agents (Kargel, 1991, 1992; Deschamps et al., 2010; Dougherty et al.,

2018), representing another important contribution to possibly creating conditions conducive to life.

However, not all CPD conditions were found to allow for the conversion of carbon and nitrogen species to these comparatively more refractory species. Mousis et al. (2002); Mousis & Gautier (2004) considered the same reaction network as Prinn & Fegley (1981) under more turbulent and lower density conditions than the Prinn & Fegley (1981) CPD, meant to better represent the Jovian and Saturnian CPDs. In these CPDs, they found that the conversion of CO and N_2 to CH_4 and NH_3 was too inefficient to occur on a reasonable timescale in the vast majority of each disk and so would not produce significant abundances of these species. They concluded that carbon and nitrogen then could only be delivered to growing satellites through the trapping of volatile carbon and nitrogen species within cages of water ice molecules called clathrates that would form in the protoplanetary disk and be delivered to the CPD (Mousis et al., 2002; Mousis & Gautier, 2004; Mousis et al., 2009).

The production of refractory carbon and nitrogen carriers may occur through other pathways than those considered by Prinn & Fegley (1981). Oberg et al. (2023) explored a variety of different reaction networks, finding that refractory carbon and nitrogen species such as CO_2, HCOOH, and NH_3 (freeze-out temperatures of $\sim$ 80K, 120K, and 80-100K, respectively Bosman et al., 2018; Oberg et al., 2023) could be created within their CPD under certain starting compositional conditions. While the production of NH_3 was fairly inefficient and yielded low abundances, leaving nitrogen sequestered in more volatile carriers, carbon-bearing species were able to be converted into more refractory carriers that could potentially be delivered to forming satellites at relatively high abundances.

While these studies constitute key first steps towards understanding whether icy satellite makeup is determined primarily by protoplanetary disk composition or by chemical processing occurring within the CPD, these studies did not consider CPDs with the conditions necessary for satellite formation. Satellite formation can be hampered by the "millimeter-sized barrier", in which solids can easily grow to around the millimeter size before being

rapidly accreted by the central planet due to drag induced drift (Zhu et al., 2018). Due to this effect, specific conditions are necessary for solids to be able to grow past the millimeter-sized barrier but these are generally different than those considered in the chemical studies to date. So, in order to determine whether refractory carbon and nitrogen species produced within the CPD can significantly contribute to the biocritical element inventory of icy satellites, it is necessary to understand the chemical processing that occurs in satellite-forming CPD environments.

Shibaike et al. (2017) suggested that efficient satellitesimal formation was possible through collisional dust growth in a viscous accretion CPD only for sufficiently high dust-to-gas ratios (dust-to-gas mass ratio of ≥ 1, which is greatly enhanced in comparison to predicted canonical protoplanetary disk values of $\sim$0.01) and moderate turbulence (α) values ($\alpha \sim 10^{-4}$ - 10^{-3}). This high dust-to-gas ratio and turbulence level would allow solids to quickly grow within the CPD at a rate faster than radial drift-timescales. Additionally, Shibaike et al. (2017) found that mass accretion rates of $\dot{M} \leq 0.02$ M_{Jup}/Myr onto the CPD were needed to allow satellite formation to occur outside of the water-ice snowline, which is necessary to explain the icy satellites around Jupiter and Saturn.

Alternatively, Batygin & Morbidelli (2020) found that viscous decretion disks had the potential to support satellite formation. In these disks, material that free falls towards the central planet from the protoplanetary disk would feed into the CPD from the inner disk edge and flow outwards. Decretion CPDs naturally yield regions where solids would experience a net zero local radial velocity from the balance between gas drag and the decretionary gas flow. These regions of net zero radial velocity cause particles to stop their migration, avoiding accretion by the central planet. As the concentration of solids built up in these regions, satellitesimals would then be able to grow through direct gravitational collapse.

In both the Shibaike et al. (2017) and the Batygin & Morbidelli (2020) satellite-forming CPDs, the conditions necessary for satellite formation yield temperatures and densities which are different from conditions present in the CPDs used to study chemical processing. As gas

phase chemical reaction kinetics depend strongly on both temperature and gas density, this means the chemical evolution expected in satellite-forming CPDs may differ from what was reported by Prinn & Fegley (1981) and Oberg et al. (2023).

Furthermore, a key aspect of these models for satellite formation is that both point to a dynamic setting in which materials are constantly in motion. This was not considered by Prinn & Fegley (1981), Mousis et al. (2002) and Mousis & Gautier (2004), as they utilized a static CPD model that did not take into account the dynamic nature of material within the CPD. Additionally, while Oberg et al. (2023) did consider the dynamic timescales of material within the CPD, they did not explicitly model the dynamic evolution of the incorporated material as the reactions occur. Considering the dynamic evolution and growth of material within the CPDs is important to potential chemical processing as the evolution and growth of solids may be critical factors in setting their thermal and chemical evolution as they move through different environments.

In this work, we model the dynamical, thermal, and chemical evolution of solids and gas within the two satellite-forming CPDs of Shibaike et al. (2017) and Batygin & Morbidelli (2020). We describe our chemical modeling approach and examine the resulting production of more refractory carbon and nitrogen-bearing species in Section 3.3 under conditions where satellite growth is expected. Section 3.4 details the dynamic gas evolution model we utilize within satellite-forming CPDs and explores the resulting effect on the production of refractory carbon and nitrogen species. We then outline our model treatment of satellitesimal growth from reservoirs of small and large dust and determine the accretion efficiency of locally produced refractory carbon and nitrogen species onto growing satellitesimals within each satellite-forming CPD in Section 3.5. Discussion of our results and implications for the chemical composition of regular satellites is presented in Section 3.6. These findings are summarized in Section 3.7.

3.3 Chemical Processing in Satellite-Forming CPDs

In this work, we adopt two different steady-state satellite-forming disks introduced by Shibaike et al. (2017) and Batygin & Morbidelli (2020) (hereafter referred to as S17 and B20, respectively). Though there are a variety of satellite-forming models within CPDs we could choose to use for this work (e.g. Canup & Ward, 2002; Mosqueira & Estrada, 2003a,b; Ogihara & Ida, 2012; Shibaike et al., 2017; Batygin & Morbidelli, 2020), we have chosen to consider the S17 and B20 CPDs for three reasons:

1. Both the S17 and B20 CPDs can reproduce the formation of satellites outside the CPD snowline, which is necessary for forming the icy satellites seen in the Jovian and Saturnian systems.

2. Each model considers how and where material is delivered to the CPD and includes this within their model framework, which until recently had not been considered within satellite-forming CPD models.

3. When considered together, these two models provide examples of satellite formation under very disparate conditions, which allows us to assess the production of refractory carbon and nitrogen species in two very different satellite-forming environments which likely bracket other potential satellite-forming CPDs.

S17 and B20 have significant contrasts in the mechanisms and requirements under which satellitesimals are able to be formed, as well as in where material is assumed to be added to the CPD from the protoplanetary disk. This leads to clear differences in the temperature and gas density environments, dynamic evolution of material, and satellitesimal growth and evolution within each CPD. However, the S17 and B20 CPD environments are not only distinct from each other, but are also different from the P+F81 and O23 CPD environments where chemical processing has previously been studied but are likely unable to produce satellites due to the radial drift barrier.

When comparing the radial temperature and surface density distributions from the P+F81, S17, B20, and O23 CPDs (Figure 3.1), we can clearly see that each of the disks

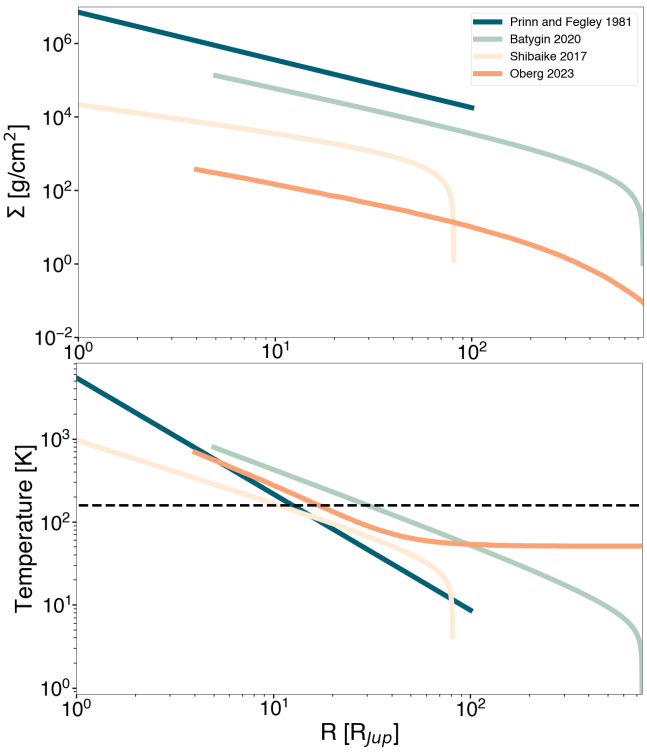

Figure 3.1: Radial surface density (top) and temperature (bottom) distributions for the P+F81, S17, B20, and O23 CPDs. The temperature of the water snowline (T = 160K) is denoted by a black dashed line (bottom panel).

have different physical structures. The P+F81 CPD environment has both the highest surface densities among the disks and the lowest midplane temperatures for the majority of the disk. This is likely due to the early nature of this work as, at the time, the structure and transport of material within disks (including CPDs) was not well understood in detail. Additionally, as the idea of viscosity in gaseous disks as a mechanism of angular momentum transfer and a source of heat was not widely accepted yet, early CPDs did not consider viscosity and were static. This resulted in early CPD models relying on simple power law relationships to determine radial temperatures and surface densities (e.g. Lewis, 1974; Pollack et al., 1976).

In order to match the compositional data of planets and satellites in our solar system that was available at the time, the P+F81 CPD utilized a cold temperature structure based on condensate formation temperatures (Lewis, 1974). Their CPD featured much lower tem-

peratures than the S17, B20, and O23 CPDs as the P+F81 CPD was both assumed to be opaque to solar radiation and did not include viscous heating. As their disk was opaque, it was assumed to be adiabatic with no heat exchanged between the disk and the surrounding environment (e.g. Lewis, 1974; Pollack et al., 1976). The P+F81 CPD also featured a comparatively high surface density profile compared to the other CPDs as it was theorized that high gas densities were needed in order to generate condensates necessary to match prevailing planet and satellite compositional data (e.g. Lewis, 1974; Pollack et al., 1976; Prinn & Fegley, 1981). Additionally, as stated above, the P+F81 CPD did not consider how material was added to the disk or the subsequent dynamic evolution of material.

While the P+F81 CPD was able to convert CO and N_2 incorporated from the protoplanetary disk into more refractory molecular carriers of carbon and nitrogen, their CPD has now been replaced by CPDs whose structures are determined by the rate of material incorporation and the disk viscosity. One such CPD is the O23 disk. Their CPD is a gas-starved (i.e. low surface density), optically-thick, actively-fed accretion disk akin to the CPD theorized in Canup & Ward (2002), which allows the disk physical processes occurring to determine the disk structure. The gas-starved nature of their disk leads to a very low radial surface density distribution compared to other disks (Figure 3.1 top), which results in the higher global dust-to-gas ratios needed for satellite formation. Unlike the Canup & Ward (2002) disk, however, the O23 CPD explicitly assumes a radial region where material infall occurs to determine the temperature and surface density conditions through the redistribution of material within the disk (Oberg et al., 2022, 2023).

Though both the P+F81 and O23 CPDs investigate potential chemical processing through various chemical reaction networks, neither considers conditions necessary for satellite formation to occur within their disks. While chemical processing within non-satellite-forming disks is interesting in both a chemical and CPD detection context, we need to consider the chemical processing occurring within the satellite-forming S17 and B20 CPDs to assess whether biocritical element-bearing molecules can be produced within these disks and po-

tentially incorporated into forming satellitesimals. We discuss in detail the physical pictures and equations used to describe the S17 and B20 CPDs below.

3.3.1 Shibaike et al. 2017 CPD

The S17 CPD is characterized as a classical accretion disk, where material from the protoplanetary disk falls onto the outer part of the disk and flows inwards towards the central planet. This disk is supplied with a constant source of solids from the surrounding protoplanetary disk as gaseous material and entrained dust grains fall onto the disk surface (Machida et al., 2008; Tanigawa et al., 2012; Szulágyi et al., 2014). The infall of material is assumed to occur over a narrow radial range concentrated at $r_b = 27$ R_{Jup}, which hydrodynamic simulations of material flow has predicted is the maximum radius that gas will enter the CPD as a result of shock dissipation and gravitational acceleration from the planet (Tanigawa et al., 2012; Fujii et al., 2014).

As material enters the CPD at this location, it viscously spreads, forming a disk whose surface density is given by:

$$\Sigma(r) = \frac{\dot{M}}{3\pi r_b} \frac{r^{\frac{3}{2}}}{\nu} \left(-\frac{2}{9} r^{-\frac{1}{2}} + \frac{2}{3} r_b r^{-\frac{3}{2}} \right) \tag{3.1}$$

where $\dot{M}$ is the mass accretion rate of material into the CPD, r is the radial distance from the central planet to the location being considered, r_b is the radius where material infall is assumed to be concentrated, and ν is the disk viscosity characterized by the alpha prescription (effective turbulence level) in Shakura & Sunyaev (1973):

$$\nu = \alpha c_s H \tag{3.2}$$

Here, H is the gas scale height represented by:

$$H = \frac{c_s}{\Omega_K} \tag{3.3}$$

and c_s is the sound speed:

$$c_s = \left(\frac{kT}{\bar{m}}\right)^{\frac{1}{2}} \tag{3.4}$$

where T is the gas temperature, k is the Boltzmann constant, $\bar{m}$ is the average mass of a gas molecule in the CPD (taken to be 2.3 times the mass of a hydrogen atom, $m_{\rm H}$, as gas is largely expected to be hydrogen and helium rich), and Ω_K is the Keplerian angular frequency:

$$\Omega_K = \left(\frac{GM_p}{r^3}\right)^{\frac{1}{2}} \tag{3.5}$$

Here, G is the gravitational constant and M_p is the mass of the central planet at the time of consideration.

The S17 CPD models the growth of solids through collisional accretion, surveying a wide range of dust-to-gas ratios and turbulence levels to determine which conditions allow for the growth of satellitesimals within their CPD. Within the CPD, as previously discussed, growing solids are subject to the millimeter-size barrier, where solids that reach a millimeter in radius have very short drag timescales and are quickly lost to the central planet (e.g. Zhu et al., 2018). In order to overcome this barrier, the rate of solid growth needs to be faster than the drag timescale, which can occur at high dust-to-gas ratios (dust-to-gas ratio $\sim$1, where the predicted value for the protoplanetary disk is 0.01 or 0.005).

Growth of satellites may also be limited by collisions that are too energetic. When growing solids collide at high velocities ($v \gtrsim$10 m/s), they will either bounce off of each other or fragment into much smaller pieces instead of coagulating (e.g. Birnstiel et al., 2011, 2012; Okuzumi et al., 2012). As the collisional velocity between solids is dependent on the turbulence within the disk, Shibaike et al. (2017) find that only moderate levels of turbulence

($\alpha \sim 1 \times 10^{-4} - 1 \times 10^{-3}$) allow for satellites to grow without being limited by bouncing or fragmentation. Turbulence that is too high ($\alpha > 1 \times 10^{-3}$) results in collisions that are too energetic, while turbulence that is too low ($\alpha < 1 \times 10^{-4}$) does not allow enough collisions to grow large enough to overcome radial drift before crossing the water-ice snowline (located at $\sim$10R_{Jup} in the S17 disk), making the formation of icy satellites impossible.

Within the S17 CPD, viscous heating is assumed to be the primary heat source for setting the disk's temperature distribution. The midplane temperature distribution is represented by the equation:

$$T_{\rm m} = \left(\frac{9}{8\sigma_{SB}} \nu \Sigma \Omega_K^2 \right)^{\frac{1}{4}} g(\tau) \tag{3.6}$$

(Nakamoto & Nakagawa, 1994) where σ_{SB} is the Stefan-Boltzman constant, and Σ is the gas surface density calculated from Equation 3.1. The opacity of the disk contributes to temperature through $g(\tau)$, which is a function of the Rosseland mean optical depth (τ). Here, we follow Shibaike et al. (2017) in assuming a minimum CPD midplane temperature distribution by setting $g(\tau) = 1$, resulting in an optically thin and vertically isothermal CPD. This allows for the formation of icy satellites exterior to the water-ice snowline for a wider range of mass accretion rates.

Finally, to form icy satellites, they must grow outside the water-ice snowline. In the S17 CPD, mass accretion rates $\dot{M}$ >0.02 M_{Jup}/Myr yielded CPD temperatures greater than the freeze-out temperature of water ice ($\sim$ 160K within the CPD) in the regions where satellite formation occurred, making these high mass accretion rates unsuitable for icy satellite formation (Shibaike et al., 2017). Given these constraints for satellite formation within the S17 disk, we use dust-to-gas ratio = 1, $\alpha = 1 \times 10^{-4}$, and $\dot{M} = 0.02$ M_{Jup}/Myr for our simulations of chemical processing within the S17 CPD. These conditions, which Shibaike et al. (2017) find are able to create satellitesimals, yield temperature and surface density distributions within the disk that are different from the three other considered disks (the S17 CPD has temperatures lower than B20 and O23 but higher than P+F81, and has surface densities lower than P+F81 and B20 but higher than O23, see Figure 3.1) which should lead

to differences in chemical processing within the S17 CPD.

3.3.2 Batygin and Morbidelli 2020 CPD

To consider an alternative physical picture for the CPD environment and satellite formation, we also consider the B20 CPD. The B20 CPD mainly differs from the S17 CPD in where material is predicted to be incorporated from the protoplanetary disk and the resulting flow of material in the CPD. While the material feeding the S17 CPD falls onto the outer portion of the disk and flows inwards, the B20 CPD envisions a scenario where material that clears the gap that forms between the protoplanetary disk and the forming giant planet free-falls towards the planet and viscously spreads outwards, creating a decretion disk (a disk type first characterized for Be stars in Lee et al., 1991). Whether a CPD will form as an accretion or decretion disk is not well understood and is believed to be determined by a variety of factors, including the strength of the planet's magnetic field, the angular momentum of the central planet and infalling material, and the infall location of deposited material feeding the planet (Lee et al., 1991; Pringle, 1991; Rafikov, 2016). As these properties may vary for forming planets and are not currently well constrained, we consider both the S17 accretion and B20 decretion CPDs to encapsulate two end-member cases for potential CPDs with distinct material infall locations.

The B20 disk's radial surface density distribution due to a constant material infall rate can be expressed as

$$\Sigma(r) = \frac{\dot{M}}{3\pi\nu}\left(\sqrt{\frac{r_H}{r}} - 1\right) \tag{3.7}$$

Here, $\alpha = 1 \times 10^{-4}$ (comparable to the turbulence level in the S17 CPD), ν is viscosity as above, r_H is the Hill radius of the planet $r_H = a(\frac{M_p}{3M_\odot})^{\frac{1}{3}}$ (where a is the distance between the star and planet and $M_\odot$ is the mass of the star), and $\dot{M}$ represents the material infall rate onto the CPD which Batygin & Morbidelli (2020) assumes to be $\dot{M} = 0.1$ M_{Jup}/Myr as this is the highest rate that allows the formation of satellites outside the water-ice snowline

in their model. This mass inflow rate onto the CPD is a factor of five higher than the maximum accretion rate possible for forming icy satellites in the S17 CPD (0.02 M_{Jup}/Myr) and results in the B20 CPD having a higher surface densities than both the S17 and O23 CPDs, though it still has a lower surface density distribution compared to the P+F81 CPD.

Heating of the B20 CPD is also assumed to be dominated by viscous heating, resulting in the radial temperature distribution being set by the energy balance between viscous heating from the disk interior and blackbody radiation from the CPD surface. This balance yields the same temperature expression for the S17 CPD in Equation 3.6. Additionally, like the S17 CPD, the B20 CPD is also assumed to be optically thin and vertically isothermal to allow for the formation of icy satellites under higher mass incorporation rates onto the CPD. However, the resulting temperature distribution for the B20 CPD is much higher than the other CPDs we consider due to the disk's high surface densities, which has implications for potential chemical processing.

The B20 decretion CPD also naturally yields satellitesimal growth without necessitating a global dust-to-gas ratio higher than that of the protoplanetary disk, providing a contrast to the collision accretion growth of satellites and conditions within the S17 CPD. Within a decretion disk, the two dynamic effects acting upon growing solids are gas drag due to the gas rotating at slower-than-Keplerian speeds (i.e. the source of the millimeter-size barrier within the CPD) and the outwards radial flow of material through the CPD. These two effects act in opposing directions, with gas drag causing solids to lose angular momentum and drift radially inwards while the outwards radial flow of material causes solids to gain angular momentum and drift radially outwards. Batygin & Morbidelli (2020) found that, within their decretion disk, solids would naturally arrest at the point in the disk where the inwards radial drift balanced the outwards radial flow of material. At these points of arrest, or particle traps, similar-size solids would start to accumulate and form a localized region with an enhanced dust-to-gas ratio. Once the dust-to-gas ratio within a particle track region grows high enough, solids are then able to gravitationally collapse into satellitesimals, which

then continue to evolve and grow.

Within the B20 CPD, the material feeding in at the inner edge of the CPD is expected to be gaseous with entrained small dust, much like the material predicted to be infalling into the S17 CPD. However, though all solid material is assumed to enter the S17 CPD entrained within vertically accreted gas, the solids that contribute to satellitesimal growth in the B20 CPD are envisioned to be sourced from either sub-millimeter (0.1 mm) sized solids that are able to enter the outer edge of the CPD due to radial drift after diffusing across the gap between the outer CPD edge and protoplanetary disk, or from sub-millimeter sized solids deposited by planetesimals that are ablated within the CPD (e.g. D'Angelo & Podolak, 2015; Ronnet & Johansen, 2020). B20 found that these solids were able to become stuck in particle traps, while material that entered the inner CPD edge with infalling gas would either quickly be accreted by the central planet or join the outward material flow to the outer regions of the CPD.

3.3.3 Gas-Phase Reaction Model

As our aim is to characterize the extent to which chemical processing of materials occurs within satellite-forming CPDs, specifically in regards to biocritical elements, we have utilized a selection of chemical reactions focusing on important pathways for processing carriers of nitrogen and carbon.

The reaction rate coefficients for gas-phase reactions are governed by the Arrhenius law (McElroy et al., 2013):

$$k = \alpha \left(\frac{T}{300} \right)^{\beta} e^{-\frac{\gamma}{T}} \tag{3.8}$$

where T is the gas temperature, and α, β, and γ are rate constants specific to each chemical reaction and are determined by experimentation (see Table 3.1 for rate constants and corresponding references).

Using the reaction rate coefficients, we can calculate the formation rate of a product

Reaction Rate Constants			
Eq. #	α	β	γ [K]
3.13[1]	2.3×10^{-10}	0	36200
3.14[2]	8.5×10^{-8}	0	81515
3.15[3]	2.81×10^{-13}	0	176
3.16[3,4]	1×10^{-30}	0	0
3.17[3,5]	6.07×10^{-30}	-1.76	0

Table 3.1: List of reaction rate constants used to calculate reaction rate coefficients for carbon and nitrogen processing reactions from Prinn & Fegley (1981) and Oberg et al. (2023). Exponents on equation number corresponds to the reference(s) where each constant was taken from: 1. Prinn & Barshay (1977) 2. Lewis & Prinn (1980) 3. McElroy et al. (2013) 4. Oberg et al. (2023) 5. Gordon et al. (1971). These reaction rate constants are derived from either experimentation or reaction physics modeling and have some uncertainty associated with them (discussed in above references).

by multiplying the reactant densities by the corresponding reaction rate coefficient. For example, for the simple reaction A + B $\rightarrow$ C, the formation rate of C is calculated by the expression:

$$\frac{\partial[C]}{\partial t} = k[A][B] \tag{3.9}$$

We can also estimate chemical reaction timescales using the calculated reaction rate coefficients and the starting reactant densities. Using the same simple reaction example as before, A + B $\rightarrow$ C, the chemical reaction timescale for this equation is represented by the expression:

$$t_{\text{reaction}} = \frac{[C]}{k[A][B]} \tag{3.10}$$

As we are calculating the chemical timescale for the reaction to go to completion, [C] will be equal to the smaller value of either [A] or [B] as you can only make as much product as your least abundant reactant.

Once the resulting densities of species involved in the chemical reaction networks have been calculated for the desired evolution timescale, we make the simplifying assumption that any species whose freeze-out temperature is higher than the current location temperature is immediately available in the form of ice frozen out on small particles. This is a valid

assumption as the maximum freeze-out timescale for CO_2 and NH_3 within both the S17 and B20 CPDs is on the order of microseconds, meaning species will freeze-out much quicker than material dynamical timescales.

Using the equations detailed here to calculate reaction coefficients, product creation rates, and chemical timescales, we can now investigate whether the chemical reaction networks outlined in P+F81 and O23 drive chemical processing in the S17 and B20 satellite-forming CPDs.

3.3.4 Prinn and Fegley 1981 Reaction Network

As discussed previously, Prinn & Fegley (1981), followed by Mousis et al. (2002); Mousis & Gautier (2004), considered two chemical reaction networks that allowed the conversion of more volatile carbon and nitrogen carriers to more refractory ones (CO to CH_4 and N_2 to NH_3). In order to determine whether these chemical reaction networks are viable within the S17 and B20 satellite-forming CPDs, we first consider which carbon and nitrogen species are predicted to be the dominant carriers within each CPD.

Which species is favored between CO vs. CH_4 and N_2 vs. NH_3 as predicted by equilibrium chemistry is demonstrated in Figure 3.2a. Here, we have calculated two lines of equilibrium pressures and temperatures, or the equilibrium P-T lines, for CO $\rightarrow$ CH_4 (Figure 3.2, dark red line) and N_2 $\rightarrow$ NH_3 (Figure 3.2, dark blue line) conversion reactions (equilbrium chemistry equations utilized here are detailed in Prinn & Fegley, 1981, and references there-in). For a given pressure and temperature (hereafter referred to as a reaction coordinate) on each equilibrium P-T line, we expect CO/CH_4 and $N_2/NH_3 = 1$. However, if the reaction environment is at colder temperatures or higher pressures than those given by the equilibrium P-T lines, CH_4 and NH_3 production are favored. Similarly, if the reaction environment is at higher temperatures or lower pressures than the conditions on the equilibrium P-T lines then the initial reactants, CO and N_2, will be more strongly favored.

Given this framework, we compare the corresponding temperature and pressure distribu-

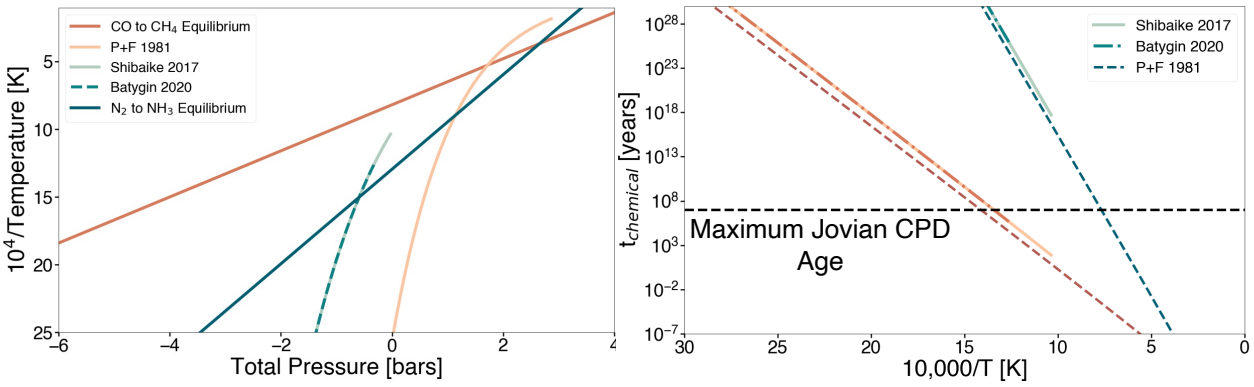

Figure 3.2: Equilibrium P-T line for CO to CH_4 and N_2 to NH_3 conversion (left) and reaction timescales for the carbon and nitrogen network rate limiting reactions (right). The S17, B20, and Prinn & Fegley (1981) CPD P-T are displayed for comparison. In the right-hand panel, the red reaction timescale lines are for CO to CH_4 conversion and blue lines are for N_2 to NH_3 conversion.

tions for the S17 and B20 models to see which carbon and nitrogen species are predicted to be the dominant species through the disks (Figure 3.2a). We find that CH_4 is predicted to be the favored carbon species within the entirety of both the S17 and B20 disks. For nitrogen, the majority of both the S17 and B20 CPDs are at temperatures and pressures such that NH_3 is predicted to be the dominant nitrogen species. However, for a small section of the S17 and B20 disks (within $\lesssim$0.5 R_{Jup} of the inner disk edge boundary which occurs at 1 R_{Jup} for the S17 CPD and 5 R_{Jup} for the B20 CPD), the temperatures are high enough that N_2 is the predicted dominant nitrogen species. These results are very similar to those found by Prinn & Fegley (1981), though their CPD structure does have a small section where the temperatures are high enough that CO is favored over CH_4 (Figure 3.2a).

However, equilibrium chemistry does not take into account reaction kinetics or the timescale on which a reaction goes to completion. The P+F81 chemical reaction networks for the production of CH_4 and NH_3 yield the following net equations

$$CO + 3H_2 \rightarrow CH_4 + H_2O \tag{3.11}$$

$$N_2 + 3H_2 \rightarrow 2NH_3 \tag{3.12}$$

which are the simplified expressions for the collection of reactions that convert CO to CH_4 and N_2 to NH_3. While one could model each reaction within the networks, we follow Prinn & Fegley (1981) by focusing on the reaction which is the slowest in each network, thereby determining how long the entire reaction chain will take and the total product created. These rate determining reactions are (Prinn & Barshay, 1977; Lewis & Prinn, 1980; Prinn & Fegley, 1981):

$$CH_2O + H_2 \rightarrow CH_3 + OH \tag{3.13}$$

$$N_2 + H_2 \rightarrow NH + NH \tag{3.14}$$

The calculated chemical timescales for the carbon and nitrogen network rate limiting reactions for the P+F81, S17, and B20 CPD P-T radial distributions using Equation 3.10 are shown in Figure 3.2b. We can see that only the very inner portion within the P+F81 CPD are at conditions resulting in reaction timescales less than the maximum Jovian CPD age (we take the maximum Jovian CPD age to be 10 million years here based on the maximum observed age for protoplanetary disks and the time necessary for the CPD to dissipate/be accreted after the protoplanetary disk dissipates, e.g. Haisch et al., 2001; Sicilia-Aguilar et al., 2006; Hernández et al., 2007; Wyatt, 2008; Mamajek et al., 2009) for both the carbon and nitrogen network rate limiting reactions.

In contrast, the S17 and B20 CPDs only have a small region at the inner edge of their disks where the CH_4 production timescale is less than the CPD maximum lifetime. While the S17 and B20 CPDs can produce CH_4 within this small region, icy satellites cannot form within the hot, inner CPD and hence locally produced CH_4 cannot be incorporated into forming icy satellites at this production location. Additionally, though we expect any CH_4

produced within this small, 0.5 R_{Jup} region at the inner edge of the S17 CPD to be directly accreted due to its close proximity to the growing planet (e.g. Ciesla, 2010, 2011; Misener et al., 2019), it is possible that CH_4 produced within this region in the B20 CPD could be transported outwards due to strong outwards radial gas flow within the decretion disk. However, we will return to this point in Section 3.5 and the discussion, as we find that refractory carbon and nitrogen production within the CPD is not the bottleneck to delivery of these species to growing satellitesimals.

For the nitrogen network rate limiting reaction, neither the S17 nor the B20 CPD have any region within their disk that has the conditions necessary for NH_3 production on relevant timescales. Hence, while NH_3 is predicted to be the dominant nitrogen species throughout most of the S17 and B20 CPDs through an equilibrium chemistry lens, the necessary reaction timescale is much longer than the plausible lifetime of the disk, leaving N_2 as the dominant nitrogen carrier in the S17 and B20 CPDs through the Prinn & Fegley (1981) chemical network.

Finally, in order to fully assess whether chemical processing through the P+F81 reaction networks is viable in satellite-forming CPDs, we also model the rate limiting reactions from P+F81 chemical reaction networks using our gas-phase reaction model. Using these reactions, we first simulated the production of CH_4 and NH_3 at a range of different orbital separations from the central planet and a wide range of starting reactant mixing ratios in the S17 and B20 CPDs. The reactions were allowed to proceed for 10 million years, our assumed maximum age of the Jovian CPD. From these simulations, we found that the rate limiting reactions for the CO to CH_4 conversion sequence and the N_2 to NH_3 conversion sequence were unable to proceed within the reaction timescale given (10 million years) in the vast majority of both CPDs for the entire range of viable mixing ratios tested. As predicted by our chemical reaction timescale calculations in Figure 3.2b, we found that negligible CH_4 (mixing ratio of less than 10^{-20} relative to the background gas density) was able to be produced within 0.5 R_{Jup} of the inner disk edge for both the S17 and B20 CPDs while NH_3

production was kinetically inhibited through the entirety of both CPDs. These results are in agreement with our calculated chemical timescales (Figure 3.2b) leading to the conclusion that NH_3 is unable to be produced efficiently within the S17 and B20 disks through the P+F81 reaction networks while CH_4 is only nominally produced and would likely only contribute to refractory carbon abundance within the B20 CPD.

3.3.5 Oberg et al. 2023 Reaction Network

While we find the production of NH_3 within the P+F81 reaction network to be kinetically inhibited within the S17 and B20 CPDs and CH_4 to be only negligibly produced in the very inner region of the S17 and B20 satellite-forming CPDs, these reaction pathways are not the only ones through which carbon and nitrogen carriers can be converted to more refractory species. Alternative reaction networks for the gas-phase production of two refractory carbon and nitrogen molecular carriers, CO_2 and NH_3, have been simulated by Oberg et al. (2023). The production of CO_2 and NH_3 through the O23 reaction networks were shown to have much shorter reaction timescales, on the order of 10^3 - 10^4 years within the O23 CPD (where this timescale is set by dynamic considerations of material movement within the CPD), which is much shorter than the maximum lifetime of the CPD. However, though the temperatures and densities within the S17 and B20 satellite-forming CPDs are distinct from those within the O23 CPD and would be predicted to lead to even more rapid CO_2 and NH_3 production through the O23 reaction networks, this has not been tested within these satellite-forming CPDs and is investigated here.

We utilize our chemical model to simulate the primary gas-phase reaction pathways presented in Oberg et al. (2023) for the production of CO_2 and NH_3. The production of CH_4 through a potential alternative reaction network to P+F81 is not addressed by O23, and is replaced by the production of CO_2. This is because O23 assumes that the conversion of CO to CO_2 is the dominant intermediate step for CH_4 production as OH produced in the optically thin surface layers of the CPD drives efficient CO_2 formation through this

reaction (Akimkin et al., 2013; Oberg et al., 2023). However, as CO_2 has a much higher freeze-out temperature than CH_4 (80K vs. 40K) and freezes out on very short timescales (<1 microsecond), CO_2 is quickly removed from the gas phase which renders it unable to continue to be processed into CH_4 through gas-phase reactions (e.g. Akimkin et al., 2013; Oberg et al., 2023). As such, solid CO_2 is produced instead of CH_4. This is advantageous to carbon enrichment in growing satellitesimals as CO_2 will be more easily incorporated into growing solids than CH_4 at higher temperatures.

We list each chemical reaction within the O23 CO_2 and NH_3 producing reaction networks we focus on below. Each reaction listed within the NH_3 production network is simulated within our model as, in contrast to the P+F81 NH_3 production network, each equation is expected to have similar reaction timescales and so there is no obvious rate-limiting reaction to isolate.

Within O23, the primary CO_2 production pathway described by the chemical reaction

$$CO + OH \rightarrow CO_2 + H \tag{3.15}$$

and the primary NH_3 production pathway is described by the following two chemical reactions

$$H_2 + N + M \rightarrow NH_2 + M \tag{3.16}$$

$$NH_2 + H + M \rightarrow NH_3 + M \tag{3.17}$$

where M is either H, H_2, or He. For these reactions, the total amount of CO_2 and NH_3 produced is determined by the starting composition of OH, and N and H, respectively.

We note that here, the starting nitrogen species in the NH_3 production pathway is N and not N_2. While the dominant carriers of carbon and nitrogen in the protoplanetary disk are predicted to be CO and N_2, material infalling onto a CPD may undergo processes such as shock heating that could cause the dissociation of molecules (such as the dissociation of N_2 into N) and alter the composition of incorporated material (Szulágyi et al., 2017; Szulágyi,

2017; Aoyama et al., 2018). As the extent to which the composition of infalling material is altered is currently not well constrained, we follow Oberg et al. (2023) in considering three potential composition scenarios for material falling onto the CPD: full inheritance, partial reset, and full reset. For the full inheritance scenario, incorporated material is assumed to undergo no processing and maintains its protoplanetary disk composition. For the opposite end case, the full reset scenario, material is assumed to undergo substantial shock-heating resulting in the full atomization of all infalling material. Finally, for the partial reset scenario, infalling material is assumed to undergo a moderate shocking event where part of the gaseous material is atomized while ices are only sublimated, leaving a mixture of inherited and processed material. The starting composition of material in the full reset and partial reset scenarios for our chemical model is then determined by the reformation of molecular species during vertical settling to the CPD midplane (Oberg et al., 2023).

O23 does consider the production of CO_2 and NH_3 through auxiliary pathways not addressed in this work, including the production through grain-surface reactions and alternative gas-phase reaction pathways. However, we choose to focus on the listed reaction networks for CO_2 and NH_3 that produce the majority of each species for simplicity and to reduce computational expense. The listed reaction networks we focus on account for $\sim$92% of the total CO_2 production and $\sim$65% of the total NH_3 production, meaning that the reactions included in our model are the primary reaction pathways. Our approach can also be applied to the O23 reaction network auxiliary pathways, but we do not expect our results to be significantly affected by the inclusion of these additional reactions.

As the O23 reactions we consider in our model are gas-phase reactions, their corresponding reaction rate coefficients are also governed by the Arrhenius law (Equation 3.8) with reaction rate constants listed in Table 3.1. The production of CO_2 and NH_3 within the S17 and B20 CPDs can then be calculated by solving for the amount of each species produced at each timestep using the Euler equation. Additionally, we can use the equation form described

in Equation 3.10 to express the chemical timescales for the CO_2 and NH_3 reactions:

$$t_{3.15} = \frac{1}{k_{3.15}[\mathrm{CO}]} \tag{3.18}$$

$$t_{3.16} = \frac{1}{k_{3.16}[\mathrm{H_2}][\mathrm{M}]} \tag{3.19}$$

$$t_{3.17} = \frac{1}{k_{3.17}[\mathrm{H}][\mathrm{M}]} \tag{3.20}$$

where $k_{3.15}$, $k_{3.16}$, $k_{3.17}$ are the reaction rate coefficients calculated using Equation 3.8 and the corresponding reaction rate constants from Table 3.1 and [H], [H_2], [M], and [CO] are the number densities of H, H_2, M, and CO calculated as:

$$[\mathrm{X}] = f_{\mathrm{X}} n_{\mathrm{gas}} \tag{3.21}$$

where X is the molecular species and n_{gas} is the background gas number density.

Reactant Starting Mixing Ratios (n_X/n_{gas})			
f_X	Full Inheritance	Partial Reset	Full Reset
f_{H_2}	0.5	0.5	0.5
f_{CO}	1.35×10^{-4}	1.35×10^{-4}	1.35×10^{-4}
f_{OH}	1×10^{-8}	1×10^{-12}	1×10^{-16}
f_H	1×10^{-16}	1×10^{-12}	1×10^{-8}
f_N	1×10^{-16}	1×10^{-12}	1×10^{-8}

Table 3.2: List of reactant starting mixing ratios within the tracked gas parcel for the gas-phase production of CO_2 and NH_3 from the reactions discussed in Oberg et al. (2023). Starting reactant mixing ratios are listed for each of the three infall scenarios which are determined by allowing material for each starting composition scenario to settle vertically down to the CPD midplane over a span of 10 years and tracking the chemical evolution of the material during its descent (Oberg et al., 2023). After this evolution period of 10 years, the final material composition is taken to be the starting abundances for each infall scenario.

To assess the viablity of O23 CO_2 and NH_3 production in the S17 and B20 CPDs, we utilize the starting compositions for each of the three material infall scenarios and use the given values as our starting reactant mixing ratios (listed in Table 3.2). We first model the gas-phase production of CO_2 and NH_3 within the S17 (Figure 3.3a,c) and B20 (Figure

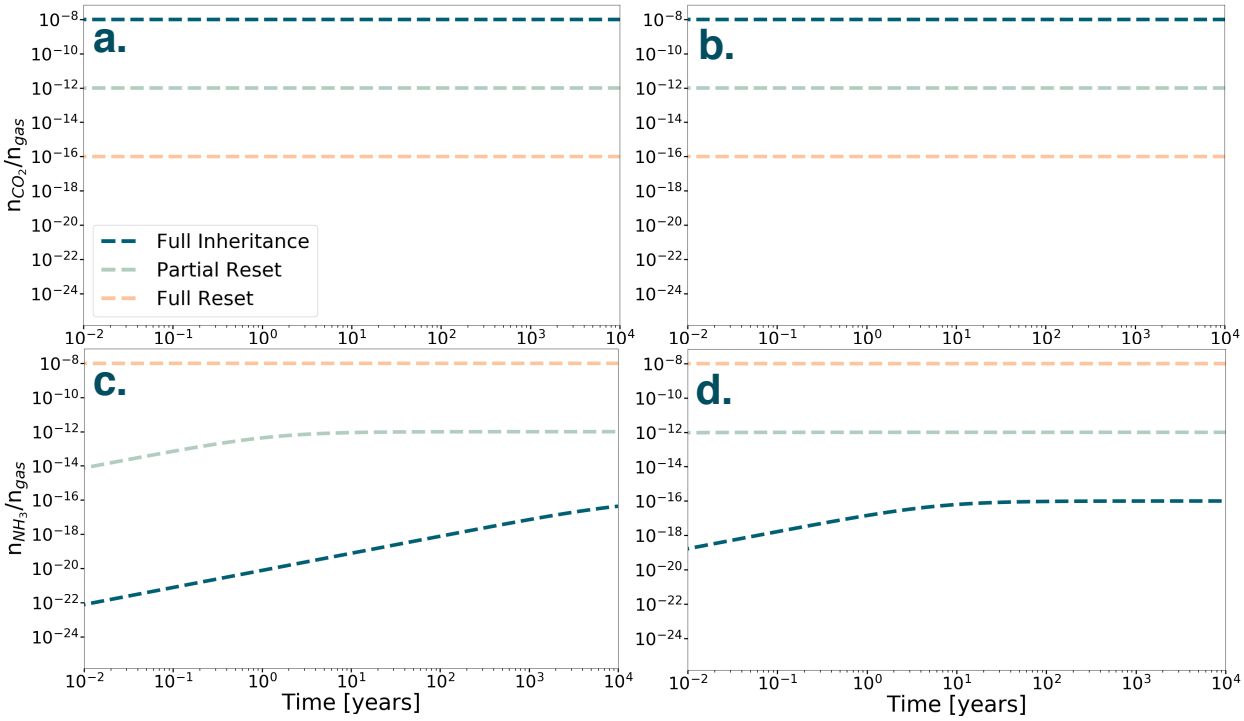

Figure 3.3: CO_2 (a,b) and NH_3 (c,d) production relative to background gas density over 10^4 years within gas parcels at the material infall location within the S17 (27 R_{Jup}, panels a,c) and B20 (5 R_{Jup}, panels b,d) CPDs. All product abundances start within the models at 1×10^{-25} (our chosen effective zero value) while the displayed product abundances start at the first timestep (0.01 years) value. Results are shown for static gas parcels that are evolved at the initiated location for 10^4 (dashed lines). Line color indicates the starting composition of the gas parcels, which is set by one of three starting material infall scenarios. While panels a and b are not incredibly interesting on their own, we include them for visual comparison with panels c and d.

3.3b,d) CPDs at the radial location where material is expected to fall onto each CPD (27 R_{Jup} and 5 R_{Jup}, respectively). We find that, in contrast to the Prinn & Fegley (1981) reaction networks, these reactions are able to proceed on timescales much shorter than the expected lifetime of the CPD. For CO_2 production, we find that in the S17 and B20 CPDs ($k_{3.15} = 2.59 \times 10^{-14}\,cm^3/s$ and $k_{3.15} = 2.25 \times 10^{-13}\,cm^3/s$, respectively) lead to incredibly fast reaction timescales (∼11.67 seconds and ∼0.003 seconds, respectively) for each of the three starting composition scenarios for the reactants in both the S17 and B20 CPDs. We note that the timescales are the same for each starting composition scenario for the CO_2 reactions because CO abundance is the same for each scenario and OH abundance is the limiting reactant.

While CO_2 production proceeds incredibly quickly for each scenario, we start to see significant differences in the NH_3 production timescale between the S17 and B20 CPDs. The reaction rate coefficients for the two reactions in the NH_3 production network, evaluated at the entry point of material in each disk and hence at different densities and temperatures, are $k_{3.16} = 1 \times 10^{-30}\,cm^6/s$ and $k_{3.17} = 7.067 \times 10^{-29}\,cm^6/s$ for the S17 CPD and $k_{3.16} = 1 \times 10^{-30}\,cm^6/s$ and $k_{3.17} = 1.086 \times 10^{-30}\,cm^6/s$ for the B20 CPD. These reaction rate coefficients yield chemical reaction timescales of much less than 0.01 years for the full reset scenario composition (0.0097 years and 9.589×10^{-6} years for the S17 and B20 CPDs, respectively), but the reaction timescales increase for the partial reset and full inheritance cases in both CPDs. We find the net reaction timescales for the partial reset composition to still be very quick at ∼1.67 years and ∼0.0095 years for the S17 and B20 CPDs, respectively, while the full inheritance composition timescales are $>10^4$ years and ∼10.28 years for the S17 and B20 CPDs, respectively. The net timescale difference observed between the partial reset and full inheritance composition cases, as well as between the S17 and B20 CPDs, can be explained by the dependence of the Equation 3.20 chemical timescale on [H]. While the reaction rate coefficients, starting f_{H_2}, and background gas density are all identical for the partial reset and full inheritance cases, the starting f_H is four orders of magnitude smaller

in the full inheritance composition yielding longer reaction timescales.

The shorter reaction timescale for NH_3 production in the B20 CPD than the S17 CPD can be similarly explained by the dependence on gas density. For the same starting composition, the reactant mixing ratios are the same for each S17 CPD and B20 CPD model. However, the local gas densities are higher in the B20 CPD than in the S17 CPD. Additionally, material infalling onto the B20 CPD is expected to enter the CPD at the dense midplane of inner disk edge ($\sim 5R_{Jup}$) while material accretes vertically onto the disk in the less dense outer portion of the S17 CPD ($\sim 27R_{Jup}$). Due to these two effects, material at the B20 CPD infall location experiences significantly higher densities yielding the observed shorter reaction times for NH_3 production within the B20 CPD.

While we find that the abundances of produced CO_2 and NH_3 are low compared to predicted abundances of CO and N_2 within the protoplanetary disk ($\sim 1.35 \times 10^{-4}$ and $\sim 1 \times 10^{-5}$, respectively; Bosman et al., 2018), the production timescales of these species are much shorter than the lifetime of the disk, giving opportunity for higher abundances to be produced over the CPD lifetime. However, we do note that the NH_3 production abundance shown for the B20 CPD is likely an overestimation as we wouldn't expect NH_3 to be stable until about 700K, which occurs at around r = 10 R_{Jup} with lower densities and temperatures than the CPD material infall location of 5 R_{Jup}, resulting in longer NH_3 production timescales. Additionally, the CO_2 production abundance shown for the B20 CPD is also likely an overestimation as CO_2 needs to freeze out to avoid conversion to CH_4 which does not occur until around around 80K, or r = 60 R_{Jup}. Hence, outflowing material in the B20 CPD would not be able to produce CO_2 until it drifted outwards from the material infall location of r = 5 R_{Jup} to r = 60 R_{Jup}. However, the overestimation of CO_2 and NH_3 production does not affect our overall conclusion that local production of refractory carbon and nitrogen is not the limiting step to delivering CPD produced refractory species to growing satellitesimals, which we will address in the discussion.

3.4 Effect of Dynamic Evolution on Chemical Processing

We have shown that, though NH_3 production is kinetically inhibited and CH_4 production is minimal through the P+F 81 reaction networks under the conditions within satellite-forming CPDs, CO_2 and NH_3 are able to be produced through the O23 chemical networks. These reactions are not kinetically inhibited within static gas parcels at the material infall regions of the S17 and B20 CPDs, proceeding on timescales less than the maximum lifetime of the CPD. However, the O23 simulations and our above results (Figure 3.3) consider the evolution of stationary gas parcels for 10^4 years, which is not an accurate representation of how gaseous and solid material exist within a CPD. Incorporated material is expected to dynamically evolve within a CPD, experiencing different gas densities and temperatures as the material moves within the disk, which will impact the rates at which these reactions proceed. Hence, including the dynamic evolution of materials within the CPD is necessary to fully assess whether CO_2 and NH_3 production is viable within satellite-forming CPDs.

As discussed previously, the S17 and B20 CPDs expect material to be incorporated onto the disk at different locations ($r = 27R_{Jup}$ for the S17 CPD and $r = 5R_{Jup}$ for the B20 CPD). Material incorporated onto each CPD will then experience different dynamical evolution pathways and by extension different environments, which may cause differences in chemical processing between these two satellite-forming CPDs.

In order to track the distinct evolution of material incorporated into the S17 and B20 CPDs, we follow the method outlined by Takeuchi & Lin (2002) to calculate how gas moves within the S17 and B20 CPDs using the equations governing angular momentum transfer for a viscous disk. The resulting radial gas velocity fields for the S17 and B20 CPDs are shown in Figure 3.4. We find that both CPDs are characterized by outwards radial flow at the midplane up to $z \sim H$ (higher for the B20 CPD as the net radial flow is outwards) and inwards radial flow in the midplane region, displaying the conveyor-belt-like flow pathway predicted to occur in the protoplanetary disk (e.g. Takeuchi & Lin, 2002; Keller & Gail, 2004; Ciesla, 2009) and seen in some CPDs (e.g. Tanigawa et al., 2012; Szulágyi et al., 2016).

For the S17 accretion disk, material above one scale height experiences rapid inwards flow towards the central planet. This flow is reversed in the region between the midplane and one scale height, where gaseous material slowly moves outwards towards the outer edge of the CPD. While the B20 CPD experiences the same general flow pattern, gaseous material moves inwards at slower velocities in B20 CPD than the S17 CPD. Additionally, the region of outwards material flow in the B20 from the midplane to one scale height moves at velocities an order of magnitude faster than in the S17 CPD ($v_{\mathrm{r,g}} \sim 2$ cm/s in the S17 CPD and $v_{\mathrm{r,g}} \sim 20$ cm/s in the B20 CPD). These differences in material flow pattern seen in Figure 3.4 are due to the distinct density and viscosity gradients present in each CPD, which in turn are caused by the variation in where material is incorporated onto accretion disks vs. decretion disks (see discussion in Section 3.3.2).

Using these velocity fields, we then calculate how gas parcels move within both the S17 and B20 disk after incorporation into each CPD and settling to the midplane. Each gas parcel is initialized at the disk midplane and radial location where material is expected to feed into each disk (r = $27\mathrm{R_{Jup}}$ for the S17 CPD and r = $5\mathrm{R_{Jup}}$ for the B20 CPD). Then, the radial movement of each parcel through the disk is determined using the background gas velocity from the calculated velocity fields. We find that for both the S17 and B20 CPDs, the gas parcels move outwards along the midplane following the background flow of gas ending at r $\sim 45\mathrm{R_{Jup}}$ and r $\sim 120\mathrm{R_{Jup}}$ after 10^4 years, respectively.

Though we assume that gas parcels do not exchange material with the surrounding environment as they migrate, we track the densities and thermal environments experienced by the parcels as they move through each disk and use these histories to simulate the chemical processing experienced during dynamical evolution using our chemical model and the O23 reaction networks. When we compare the chemical processing that occurs in the static and dynamic gas parcel models, we find that there are no significant differences in final CO_2 abundances between the static and dynamic gas parcel cases for either the S17 CPD or the B20 CPD. This is due to the short reaction timescale for CO_2 production, which allows rapid

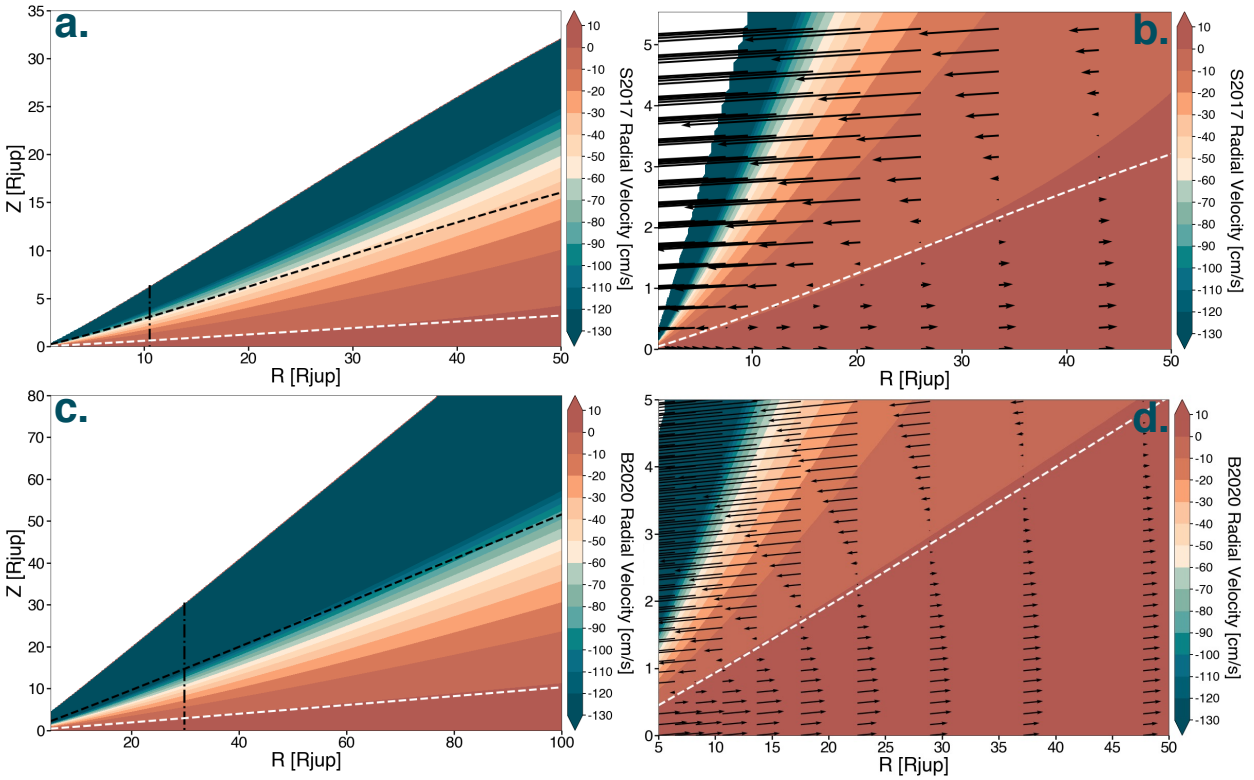

Figure 3.4: Radial velocity field distributions for the S17 CPD (a,b) and B20 CPD (c,d) for their fiducial mass accretion rates ($\dot{M} = 0.02\ \frac{M_{\rm Jup}}{\rm Myr}$ for S17, and $\dot{M} = 0.1\ \frac{M_{\rm Jup}}{\rm Myr}$ for B20). Panels a and c show the gas radial velocity contours for each disk, while panels b and d show velocity vectors (black arrows) overplotted on the corresponding velocity contour for a zoomed-in portion of the disk. H and 5H at each radial location are denoted by the white and black dashed lines, respectively, and the water snowline contour is marked by the black dash-dotted line (where T = 160K) (panels a,c). Panels b and d display H at each radial location shown by the white dashed line.

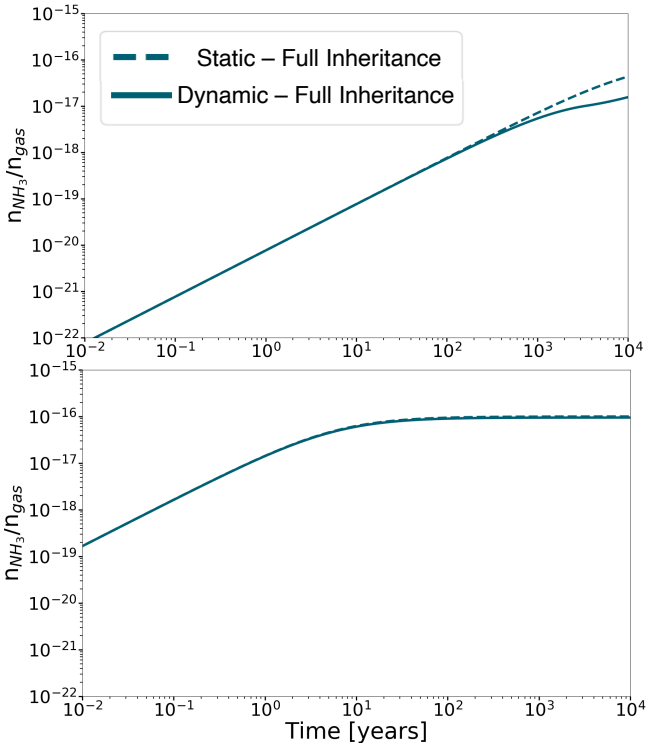

Figure 3.5: NH_3 production relative to background gas density over 10^4 years within gas parcels started at the material infall location within the S17 (27 R_{Jup}, top panel) and B20 (5 R_{Jup}, bottom panel) CPDs. All product abundances start within the models at 1×10^{-25} (our chosen effective zero value) while the displayed product abundances start at the first timestep (0.01 years) value. Gas parcel production abundances are shown for static gas parcels (dashed lines) and gas parcels that are allowed to evolve dynamically within the disk (solid lines). As two of the three material infall cases result in no difference between the static and dynamic gas parcel cases (full reset and partial reset), we only show the full inheritance material infall case to show the effect of considering dynamic evolution of material within the CPD on chemical processing.

formation of CO_2 before the dynamic gas parcel moves outwards in the disk which would significantly lower gas densities and temperatures, increasing the CO_2 formation timescale (the reaction timescale is on the order of 10 seconds for the S17 disk and on the order of 1 millisecond for the B20 disk while the outwards radial gas velocity at the midplane is on the order of 10 cm/s).

For NH_3 production, we find that considering dynamic evolution of material reduces the final abundance of NH_3 produced for both the S17 and B20 CPDs. The static gas parcel yields approximately 5x higher final NH_3 abundances in the S17 disk and a very small (on

the order of a percent) increase in NH_3 abundances in the B20 disk in the full inheritance composition case only. This disparity in NH_3 production between the static and dynamic gas parcels occurs due to the differences in local gas density evolution each parcel experiences. While the local gas density stays constant throughout the 10^4 year evolution for the static gas parcel, the dynamic gas parcel experiences lower gas densities as it migrates outwards in the disk. The NH_3 reaction timescale increases at lower gas densities, leading to a depletion in the amount of NH_3 that can be created over the 10^4 year evolution as the parcel moves outwards in the disk or before the parcel is carried out of the outer edge of the CPD. This effect is only seen in the full inheritance composition case, however, as the low starting abundance of H causes the starting reaction timescale to be longer than for the partial and full reset scenarios and be on the order of the dynamic evolution timescale for the dynamic parcel.

Additionally, while we see that production of refractory carbon and nitrogen species CO_2 and NH_3 is viable within the S17 and B20 CPDs at the midplane for both the static and dynamically evolving material, this production efficiency is the maximum possible within the disk. Away from the midplane, towards the upper layers of the CPD, gas density drops dramatically with vertical height. This leads to a corresponding increase in reaction timescale and decrease in the efficiency of CO_2 and NH_3 production within the 10^4 year evolution period. If dynamically evolving gas parcels are lofted up to vertical heights above the midplane, as would occur due to vertical diffusion in a turbulent CPD environment, the gas parcels would be exposed to lower gas densities relative to the midplane and as a result produce less refractory CO_2 and NH_3 while in those regions. Hence, the amount of CO_2 and NH_3 production predicted by our models here is a maximum amount and would likely be lower in a more turbulent CPD environment. At the same time, if CO_2 and NH_3 production timescales are very short at the midplane, these reactions may reach completion before being lofted to these altitudes.

3.5 Accretion of CPD Produced Refractory Species by Growing Satellitesimal Seeds

While we have shown that the production of relatively more refractory carbon and nitrogen species can occur within satellite-forming disks through the Oberg et al. (2023) gas-phase reaction networks for both static and dynamically evolving material, these products still need to be incorporated into growing satellitesimals in order to be available for future potential life. The dominant carbon and nitrogen carriers within the protoplanetary disk (CO and N_2) are unable to freeze out at the higher CPD temperatures and cannot be delivered to growing icy satellesimals in solid form. However, more refractory carbon and nitrogen carriers such as CO_2 and NH_3 are able to freeze out at higher temperatures ($\sim$ 80-100K) and therefore can be deposited onto solids within the CPD. We can then model and track the mass of solids bearing refractory carbon and nitrogen species produced within the CPD that are accreted by growing satellitesimal seeds as they dynamically evolve through the disk.

At any given instant, we can calculate the radial velocity of a growing satellitesimal seed within a CPD as

$$v_r = \frac{\frac{v_{r,g}}{St} - v_K \eta}{St + \frac{1}{St}} \tag{3.22}$$

where v_K is the Keplerian velocity ($v_K = r\Omega_K$), η denotes how sub-Keplerian the gas is (η = 1 - $\frac{v_{\phi g}^2}{v_K^2}$ where v_{ϕ_g} is the azimuthal gas velocity $v_{\phi_g} = [v_K^2 + \frac{\partial P}{\partial r}\frac{r}{\rho_g}]^{\frac{1}{2}}$ and ρ_g is the gas density), and St is the Stokes number of the particle. The Stokes number of a solid is calculated as

$$St = \frac{t_s v_K}{r} \tag{3.23}$$

and is a non-dimensional representation of particle size where t_s is the stopping time of the

particle described by the piece-wise expression:

$$t_s = \begin{cases} \frac{\rho_p r_p}{\rho_g v_{\rm th}} & \text{if } t_s \leq \frac{9}{4}\lambda_{\rm mfp} \\ \frac{4 r_p}{9 \lambda_{\rm mfp}} \frac{\rho_p r_p}{\rho_g v_{\rm th}} & \text{if } t_s > \frac{9}{4}\lambda_{\rm mfp} \end{cases} \tag{3.24}$$

Here, r_p is the radius of a growing satellitesimal seed, ρ_p is the internal density of solids within the CPD (assumed to be 3 g/cm^3 in this work), $\lambda_{\rm mfp}$ is the mean free path-length of an average gas particle at this location with in the CPD ($\lambda_{\rm mfp} = 2.3 {\rm m}_H / \sigma_{\rm mol} \rho_g$ where $\sigma_{\rm mol}$ is the collision cross section of gas molecules, $\sigma_{\rm mol} = 2 \times 10^{-15}$ cm^2), and $v_{\rm th}$ is the thermal velocity of the gas particles $v_{\rm th} = \sqrt{\frac{8}{\pi}} c_s$.

We follow S17 and B17 in assuming that growing satellitesimal seeds start out as solids with radius ${\rm r}_p = 0.1$ mm. Hydrodynamic simulations of solid infall onto CPDs suggest that 0.1 mm is the maximum size of solids that can be entrained within the gas infalling onto the CPD (e.g. Tanigawa et al., 2014; Fujii et al., 2014; Homma et al., 2020) and the maximum size of the particles that can enter the CPD through the outer disk edge by diffusing across the gap between the CPD and protoplanetary disk (Zhu et al., 2012), making solids of this size most likely to be the seeds of growing satellitesimals. Additionally, as these solids are supplied from protoplanetary disk materials, we can assume that growing satellitesimal seeds are initially comprised of material incorporated directly from the protoplanetary disk and thus lack carbon and nitrogen. Incorporation of any additional carbon or nitrogen would have to occur during growth and dynamical evolution of the satellitesimal seeds within the CPD.

As locally produced refractory carbon and nitrogen species are deposited onto dust grains, we assume that these species preferentially freeze out onto small, sub-micron sized dust that represents the vast majority of the solid surface area within the disk. This creates a population of small solids with enhanced abundances of carbon and nitrogen-bearing species which we refer to as the "enhanced dust" population. Growing satellitesimal seeds can then gain locally produced refractory carbon and nitrogen species only through the accretion of

these small dust grains. In contrast, larger solids do not experience preferential freeze-out and so will not contribute to a growing satellitesimal seed's carbon and nitrogen inventory upon accretion. This makes tracking the accretion of small enhanced and non-enhanced larger solids incredibly important for predicting whether CPD produced refractory carbon and nitrogen species can be efficiently accreted by growing satellitesimal seeds.

Following this framework, we simulate the growth of satellitesimal seeds within the CPD using the methodology detailed in Krijt & Ciesla (2016) and Misener et al. (2019). In this physical model of solid growth, particles grow through colliding with two distinct solid populations. The first population consists of small, sub-micron sized dust grains (radius of 0.1μm) that represent the carbon and nitrogen enhanced dust within the CPD. These solids enter the CPD within infalling gas and are responsible for determining disk opacity (e.g. Semenov et al., 2003). As dust moves at sub-Keplerian speeds while entrained in surrounding gas flows that are slower than the velocities of larger particles (Weidenschilling, 1977), this small dust can be efficiently swept up by larger solids such as growing satellitesimals.

The second population that growing satellitesimal seeds can interact with in our growth model is the non-enhanced, large solid population (referred to as the "incorporated solid" population hereafter). While our model tracks the specific evolution of one particle at a time, other solids will be growing simultaneously within the CPD and are represented through this second population. Collisions involving this large solid population are not continuous as they are for sweep-up of the small particle population, instead taking place as random, distinct events. Over a given time period, there is a random chance that a collision with a member of the large solid population will occur. As long as the relative velocity between colliding satellitesimal seeds and large incorporated particles is less than the critical velocity at which bouncing or fragmentation occurs ($\sim$10 m/s; Birnstiel et al., 2011, 2012; Okuzumi et al., 2012; Misener et al., 2019), the collision will result in the merger of the two solids.

As the large solid population is meant to represent concurrently growing large particles, we set their composition to be the same as the growing satellitesimal seed we are tracking at

the time of that specific collision. This means that the mass fraction of accreted enhanced small dust within the growing satellitesimal seed (calculated as the total mass of accreted small enhanced solids solids divided by the total amount of accreted mass) only increases when small dust grains are accreted.

By utilizing this two population growth method from Krijt & Ciesla (2016) and Misener et al. (2019), we can model not only how early growth affects the dynamics of solids within satellite-forming CPDs but also determine which solid population and CPD locations contribute most to satellitesimal seed growth. The dynamics and growth of solids within the S17 CPD is treated similarly to the method detailed in Krijt & Ciesla (2016) and Misener et al. (2019). While Misener et al. (2019) models the large solid population as the same size as the tracked satellitesimal seed, we follow Shibaike et al. (2017) and Sato et al. (2016) in setting the large solid population particle size equal to one half the Stokes number of the growing satellitesimal seed we are tracking at the time of collision. The resulting dynamic and growth evolution difference due to variation in large solid population treatment is minimal and adopting this difference in large particle population size utilized by S17 allows us to accurately replicate the dynamic and growth behavior of satellitesimal seeds reported for the S17 CPD. Additionally, as the sweep-up of small, refractory carbon and nitrogen species enhanced dust grains is not explicitly modeled within the S17 CPD, we are able to incorporate tracking this important source of solids into our model by utilizing the Krijt & Ciesla (2016) and Misener et al. (2019) method. Our resulting model allows us to determine whether growing solids primarily accrete solids enhanced with CPD produced refractory carbon and nitrogen species (the enhanced solids) or solids whose composition is determined by protoplanetary disk conditions (the incorporated solids).

We note that the B20 CPD satellitesimal growth model does not explicitly consider the growth of drifting particles before they become stuck within particle traps. If this scenario occurs, and particles do not experience significant growth before they are trapped and eventually incorporated into satellitesimals through gravitational collapse, CPD produced

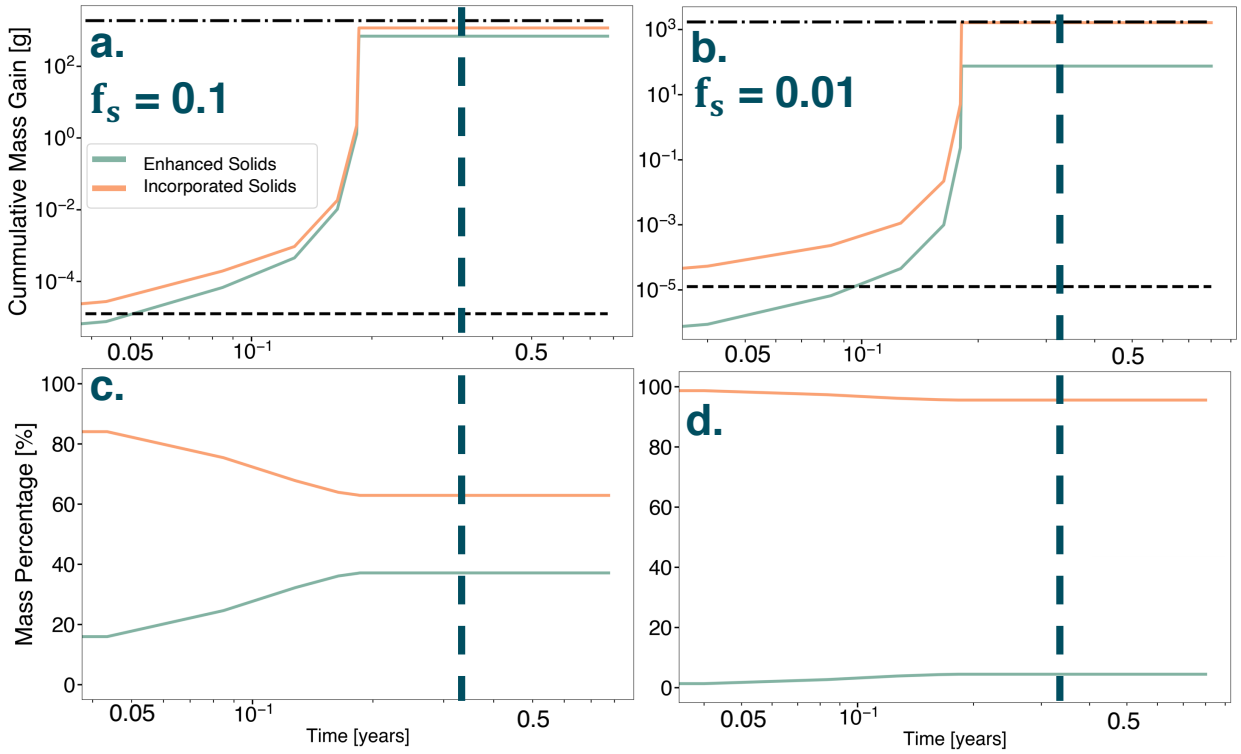

Figure 3.6: Cumulative mass gain (a,b) and mass percentage (c,d) of enhanced and incorporated solids accreted by a growing particle within the S17 CPD. The small dust fraction within the dust population is denoted as f_s and is set to either 0.1 (a,c) or 0.01 (b,d). The time when the particle crosses the CO_2 snowline is depicted by the blue dashed line, and occurs after the solid has halted growth. The starting mass of the satellitesimal seed is denoted by the black dashed line, while the black dash-dotted line represents the final mass of the satellitesimal seed at the end of its evolution.

refractory carbon and nitrogen species would not be delivered to growing satellite seeds and could not act as a vehicle through which satellites could become enhanced in carbon and nitrogen. However, we include the B20 CPD case in our satellitesimal seed growth results to both act as a point of comparison for the S17 CPD and to predict what compositional reservoir material would be accreted from if satellitesimal seeds were able to grow through early collisional accretion in the B20 CPD.

Additionally, while our model incorporates radial diffusion following the treatments described in Ciesla (2010), Ciesla (2011), and Ciesla & Sandford (2012) (see references for detailed description of this treatment), the addition is negligible for the vast majority of the satellitesimal seeds' evolution within both the S17 and B20 disk. For the S17 disk, this is

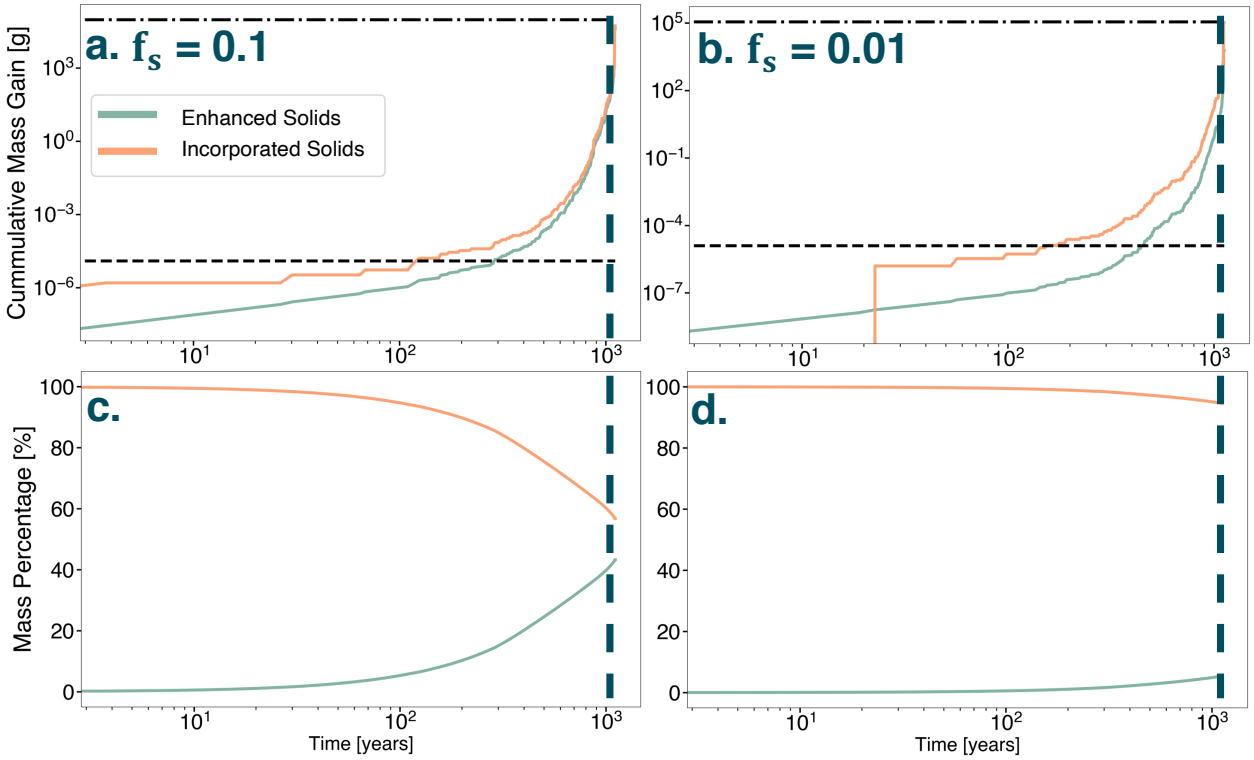

Figure 3.7: Cumulative mass gain (a,b) and mass percentage (c,d) of enhanced and incorporated solids accreted by a growing particle within the B20 CPD. The small dust fraction within the dust population is denoted as f_s and is set to either 0.1 (a,c) or 0.01 (b,d). The time when the particle crosses the CO_2 snowline is depicted by the blue dashed line, and occurs at the end of the evolution of the solid. The starting mass of the satellitesimal seed is denoted by the black dashed line, while the black dash-dotted line represents the final mass of the satellitesimal seed at the end of its evolution.

because at the location of material incorporation (r = 27 R_{Jup}) the solid growth timescale is incredibly rapid and so the satellitesimal seed quickly becomes large enough such that radial drift dominates the solid's movement. Within the B20 disk, the growing satellite seed begins at the outer edge of the CPD where the disk is incredibly diffuse and the Stokes number of the solid is relatively large, resulting in radial drift dominating the solid's movement. By the time the satellite seed migrates inwards where it would be more strongly affected by turbulence, it has grown to a size such that radial drift is still dominant. As such, the results displayed here do not include radial diffusion.

We initialize satellitesimal seeds (r_p = 0.1mm) at the material infall region of the S17 CPD midplane (r_b = 27 R_{Jup}) and the exterior edge of the B20 CPD (r_{start} = 500 R_{Jup}) where satellite-forming solids may be sourced from for the parameter set that was favorable to satellitesimal formation in both CPDs ($\alpha = 1 \times 10^{-4}$ and dust-to-gas ratio = 1.0 for the S17 CPD, and $\alpha = 1 \times 10^{-4}$ and dust-to-gas ratio = 0.01 for the B20 CPD). We allow the satellitesimal seeds to move radially within the disk until they reach St = 2 (the point at which solids grow on timescales faster than their drift timescales, occurring at r_{end} = $\sim$13R_{Jup} for the S17 CPD and r_{end} = $\sim$50$_{Jup}$ for the B20 CPD) and track the particle growth from sweep-up of enhanced small solids and collisional accretion of incorporated large solids. We stop growing satellesimal seeds at St = 2 as their radial drift rate begins to slow at this size and the seeds will undergo explosive growth as smaller, faster drifting solids reach the slowing satellitesimal seeds. During the particle's evolution, we calculate the cumulative mass gain of enhanced and incorporated solids onto a growing satellitesimal seeds and the percentage of the satellitesimal seed's accreted mass due to accreted incorporated or enhanced solids. Additionally, while we ran a large number of particle simulations, the variation between the final mass percentages of incorporated or enhanced material accreted was very small ($\lesssim 1\%$) between the suite of growing satellitesimal seeds. As such, we display a representative particle evolution for the S17 CPD (Figure 3.6) and the B20 CPD (Figure 3.7) results.

Figure 3.6 shows the evolution of a growing satellitesimal seed within the S17 disk for small dust fractions (the percentage of the dust-to-gas ratio made up of small particles, f_s) of 0.1 (Figure 3.6a,c) and 0.01 (Figure 3.6b,d). In the protoplanetary disk, values between 0.03 and 0.23 are appropriate small dust fraction values for drift-limited local growth (Birnstiel et al., 2012) and were shown to reproduce dust growth in more detailed models. As such, we follow Misener et al. (2019) in utilizing $f_s = 0.1$, hereafter referred to as the high f_s case, for one of our simulations to represent a dust population similar to the protoplanetary disk with the maximum fraction of small particles. However, the S17 and B20 disks are assumed to be optically thin and as such would have a lower fraction of small dust grains than within the protoplanetary disk. Due to this, we also simulate the satellitesimal seed growth in a CPD with $f_s = 0.01$, hereafter referred to as the low f_s case, to represent the depletion of small dust grains within the dust population.

We find that during the evolution of a growing satellitesimal seed within the S17 CPD for both small dust fraction values (Figure 3.6), the solid first experiences a phase of slow growth where it accretes both enhanced and incorporated solids (from the start of the evolution to around 0.15 years). As the growth rate of a solid depends on its effective cross-section, which in turn depends on its radius, the solid's growth rate increases as it grows larger. This yields the exponentially increasing growth rate seen from $\sim$0.15 to $\sim$0.2 years. However, when the particle gets to a large enough size such that collisions with particles from the small and large particle population have relative velocities higher than the bouncing barrier, the particle's growth halts ($\sim$0.2 years, Figure 3.6 a,b). The particle then drifts inwards without growing until it reaches an area where relative collisional velocities drop below the critical value and undergoes its final growth to St = 2. We also find that the entirety of the tracked particle's simulated growth occurs external to both the CO_2 and the NH_3 snowlines (Figure 3.6, blue dashed vertical line), meaning locally produced CO_2 and NH_3 would remain frozen out onto accreted enhanced solids during the entirety of the satellitesimal seed's growth.

The final composition of the satellitesimal seeds primarily reflects the incorporated com-

position from the protoplanetary disk for both the high f_s case (final mass percentage of incorporated solids is ∼63%) and the low f_s case (final mass percentage of incorporated solids is ∼95%) for its entire growth. This indicates that even when there is a relatively large small dust population present within the CPD, a growing satellitesimal's composition will primarily reflect that of material incorporated from the surrounding local protoplanetary disk. Additionally, while enhanced solids do still comprise a significant portion of the tracked solid for the high f_s case (∼37%, Figure 3.6c), when we consider a low f_s case that is more representative of the optically thin disk environment within the S17 and B20 CPDs, the percentage of enhanced solid mass in the growing satellitesimal seed drops to ∼5%, suggesting that enhanced solids will not be efficiently accreted by growing satellite seeds in the S17 CPD (Figure 3.6d).

Figure 3.7 shows similar satellitesimal seed growth evolution within the B20 disk for f_s = 0.1 (Figure 3.7a,c) and 0.01 (Figure 3.7b,d). The growth evolution pathways for both the high f_s case and low f_s case are similar to the S17 CPD tracked particles, consisting of a slow initial growth phase followed by rapid growth until growth ceases momentarily due to relative collisional velocities growing higher than the critical bouncing/fragmentation velocity. The satellitesimal seed then reaches the stopping criteria, St = 2, once it drifts inwards to the point that the relative collisional velocities dip below the bouncing barrier. The evolutionary time necessary for the particle to reach St = 2 is much longer in the B20 CPD, as the tracked particle begins its evolution in the low density outer disk region. As the satellite seed moves inwards, its growth rate increases as the surrounding gas and dust densities increase. The tracked particle reaches both the CO_2 and NH_3 snowline at the very end of its growth evolution for both the high and low small dust fraction cases when the particle has accreted almost all of its mass, meaning that the enhanced solids accreted by the tracked particle were comprised of both CO_2 ice and NH_3 ice.

Similar to both f_s cases for the S17 CPD, the satellitesimal seeds in both the B20 CPD high f_s and low f_s simulations are primarily comprised of incorporated solid material.

For the high f_s case, the solid is comprised of ∼55% incorporated material and ∼45% enhanced material (Figure 3.7c). Hence, in the B20 high f_s case, the tracked solid accretes proportionally more enhanced material than the S17 CPD high f_s case tracked particle. For the low f_s case, which is more representative of conditions expected in the B20 CPD, we see that the tracked particle is comprised of ∼4% enhanced solid material and ∼96% incorporated material (Figure 3.7d), around the same proportion as in the S17 low f_s case.

These results suggest that for the conditions present in S17 and B20 satellite-forming CPDs, while refractory carbon and nitrogen species can be produced locally through gas phase production of CO_2 and NH_3 (Oberg et al., 2023), subsequent accretion of enhanced solids bearing these produced refractory carbon and nitrogen species will be difficult. Within the protoplanetary disk, CO_2 and NH_3 abundances are predicted to be at least an order of magnitude lower than the dominant carbon and nitrogen carriers (CO and N_2) (e.g. Bosman et al., 2018; Oberg & Wordsworth, 2019). This means that even if all gaseous carbon and nitrogen incorporated from the protoplanetary disk is converted to CO_2 and NH_3, growing satellite seeds would need to accrete over 90% of their mass from the enhanced small dust population to form with the carbon and nitrogen fractions present in protoplanetary disk gas. As even our results for solid growth in small dust-rich CPDs show a maximum accretion percentage of 45% from the enhanced small dust population, we find that growing satellitesimals are unable to be enriched in carbon and nitrogen through species produced within the CPD alone.

3.6 Discussion

A key question for understanding and predicting icy satellite habitability has been whether their biocritical element inventory must be supplied directly from the protoplanetary disk or whether refractory carbon and nitrogen species can be locally produced within the CPD environment from which satellites are born. Though chemical production of carbon and nitrogen carriers that could be delivered to growing satellites has been studied in non-satellite-forming

CPDs, our work investigates the production and delivery of these carriers to potential satellites within satellite-forming CPDs. Our results indicate that production of refractory carbon and nitrogen species, specifically CO_2 and NH_3, is possible within both the S17 and B20 satellite-forming CPDs through the chemical networks utilized by Oberg et al. (2023). Additionally, we find that the production of CH_4 is minimally possible within the B20 CPD through the P+F81 chemical network.

The results of this work allow us to place constraints on the conditions under which refractory carbon and nitrogen species can be produced within a satellite-forming CPD and subsequently delivered to forming satellites. As discussed in Section 3.3.5, the reaction rates for the carbon and nitrogen networks from Oberg et al. (2023) are inversely proportional to gas density which leads to longer CO_2 and NH_3 production timescales at lower gas densities (Figures 3.3 and 3.5). Hence, material in CPDs with lower surface densities due to either lower central planet mass (e.g. Szulágyi et al., 2016; Szulágyi, 2017; Szulágyi et al., 2018) or age (Cilibrasi et al., 2018), or in more turbulent CPDs will have longer refractory carbon and nitrogen production timescales. Simulations of forming giant planets predict that as they near their final size and begin to deplete the gaseous and solid material in the surrounding protoplanetary disk, the rate of mass infalling onto the CPD decreases (e.g. D'Angelo et al., 2021). This leads to a global decrease in the CPD temperature and density. As the CPD cools, the location of molecular snowlines move inwards, allowing freeze-out of species onto small solids to occur and potentially be delivered to forming satellitesimals within a larger portion of the disk. However, as is described in our work, the simultaneous decrease in disk density leads to an increase in the reaction timescale for the creation of CO_2 and NH_3. These conditions would thus limit the abundance of these species that can be produced and accreted by growing satellitesimal seeds on relevant dynamical timescales (Figure 3.5). Similarly, if the radial outflow of gas to lower density environments within the CPD is more rapid than the reaction timescale for a refractory species, such as is seen for the production of NH_3 under the full inheritance compositional scenario (Figure 3.5) and which may occur

in disks with high turbulence or high mass incorporation rates, potential production of these species is also decreased.

There is then a trade-off between maintaining cool enough CPD temperatures for produced refractory carbon and nitrogen species to freeze out onto solids, while maintaining high enough densities to produce significant abundances of refractory species within the CPD lifetime. This trade-off implies that if existing observed satellites are the final surviving generation of satellites formed over the lifetime of the CPD (e.g. Canup & Ward, 2006; Sasaki et al., 2010; Ogihara & Ida, 2012; Cilibrasi et al., 2018), these satellites may not have been able to accrete a significant amount of refractory nitrogen species from those produced within the CPD. This is because while earlier generation satellites would form under density conditions that allow for more rapid production of refractory nitrogen, the last generation of satellites would form under low density conditions yielding slow production of NH_3 and limited nitrogen enhancement. Hence, satellites formed over a longer period of time within the CPD instead of at its end (as suggested by Shibaike et al., 2019; Ronnet et al., 2017) may have a higher potential for forming with refractory carbon and nitrogen species accreted from those produced within the CPD resulting in satellite compositions more conducive to the origin of extraterrestrial life.

We also find that the starting composition of protoplanetary material incorporated into the CPD is a key determinant for the subsequent potential production of refractory carbon and nitrogen species (Figures 3.3 and 3.5). Our results demonstrate that for both the S17 and B20 disks, CO_2 production yields the highest abundances and proceeds most quickly when accreted material composition is fully inherited without reset from the protoplanetary disk (Figure 3.3). This occurs because OH, a necessary reactant for the formation of CO_2, is destroyed by dissociation if the accreted material composition is fully or partially reset and reformation of OH from the resulting components (atomic O and H) proceeds incredibly slowly within the CPD (Oberg et al., 2023). CO, the other necessary reactant for CO_2 formation and the dominant carrier of carbon within the protoplanetary disk, does not

have the same issue as it is both highly abundant and able to reform quickly if material composition is partially or fully reset. Though CO is quickly reformed, the destruction and subsequent slow reformation of OH hinders the production of CO_2 within material whose composition is reset upon incorporation into the CPD.

In contrast to CO_2, NH_3 production is most efficient when the composition of accreted material is fully reset during accretion into the CPD for both the S17 and B20 CPDs (Figure 3.3). This is because the reactants for NH_3 that are affected by compositional reset (N and H) are actually produced instead of destroyed when molecular species dissociate upon infall. While the produced abundances of N and H will be highest if the composition of material is fully reset during accretion (though at abundances still orders of magnitude less than the abundances of CO and N_2 in the protoplanetary disk), a partial reset will also yield moderate abundances of N and H that can drive the production of NH_3. Atomic N and H are not expected to be highly abundant in material whose composition is directly inherited from the protoplanetary disk (e.g. Schwarz & Bergin, 2014; Bosman et al., 2018; Cleeves et al., 2018), resulting in low H and N abundances and minimal production of NH_3 under the full inheritance scenario.

From these results, we expect either the production of CO_2 or NH_3 to occur within CPD environments depending on whether the composition of material from the protoplanetary disk is altered upon incorporation into the CPD, but not the production of both. This means that satellites in disks where refractory carbon or refractory nitrogen production is not possible will need to receive those species directly from material accreted onto the CPD that does not undergo compositional reset. This presents a potential problem for delivering refractory carbon and nitrogen species to satellites in CPDs either in protoplanetary disks lacking refractory carriers of carbon or nitrogen or to CPDs located interior to refractory carbon and nitrogen species snowlines around the central star. Hence, the composition of material within the protoplanetary disk, as well as whether material within the protoplanetary disk survives incorporation onto the CPD, determines whether satellites form with a

rich inventory of biocritical elements or not.

Our work also allows us to determine that accretion of locally produced refractory carbon and nitrogen species is the bottleneck to producing satellites with locally produced enhanced carbon and nitrogen inventories. Within our simulations, we found that the fraction of small dust particles necessary to produce satellites comprised of a majority of enhanced solids needs to be greater than $f_s = 0.1$ in both the S17 and B20 CPDs. However, the satellite-forming disks we consider are both assumed to be optically thin and thus depleted in small dust grains (Shibaike et al., 2017; Batygin & Morbidelli, 2020). Hence, it is highly unlikely that the CPD would be able to sustain the dust abundances needed to yield small dust grain fractions of $f_s = 0.1$ or higher. Additionally, forming satellitesimals within CPDs with a small dust grain fraction more consistent with an optically thin disk ($f_s = 0.01$) accreted the vast majority of their mass ($\sim$95%) from solids directly incorporated from the protoplanetary disk. Due to the lower surface area to volume ratio of these larger solids, while produced refractory species can freeze out on their surface, these solids will not be significantly enhanced in produced refractory species.

Thus, while we have shown that refractory carbon or nitrogen species are able to be produced within the gas-phase of the satellite-forming CPDs studied, accreting those solids is likely the limiting factor to creating satellites with locally produced carbon and nitrogen inventories. In order to create satellites with CPD produced carbon and nitrogen, a mechanism would need to exist which allows for icy satellite creation within an optically thick, small dust rich CPD (such as low viscosity), or refractory carbon and nitrogen species would need to be supplied from an alternative source directly from the protoplanetary disk.

Other sources may indeed exist from which growing satellites could accrete refractory carbon and nitrogen that does not need to be produced within the CPD. If the protoplanetary disk material accreted onto the CPD is rich in refractory carbon and nitrogen species such as CO_2, NH_3, or even more refractory species, and those species survive incorporation onto the CPD (i.e. the composition of the accreted material is not partially or fully reset),

satellitesimals will then be able to incorporate these elements as they grow. As we have shown, the majority of material accreted by growing satellitesimals is directly inherited from the protoplanetary disk and so refractory carbon and nitrogen species within materials that survives incorporation into the CPD will be the feedstock from which satellitesimals grow. As such, future work should investigate in greater detail the chemical processing that occurs during the incorporation of material from the protoplanetary disk to the CPD to determine under what conditions and to what extent this processing is expected.

Alternatively, D'Angelo & Podolak (2015) and Ronnet & Johansen (2020) propose that a potentially significant delivery source of solids to the CPD is from the capture and ablation of planetesimals. Here, planetesimals from the local protoplanetary disk are captured by the CPD through drag-assisted capture and strongly ablated due to frictional heating. These solids could act as potential sources of refractory carbon and nitrogen species to growing satellitesimals within the CPD. However, as resulting solids from the captured planetesimals experience intense frictional heating resulting in their ablation, it is possible that ice species within the delivered solids would instead be driven off by this heating and supplied to the CPD in gaseous form. This potential source of additional refractory carbon and nitrogen species for growing satellitesimals and satellites warrants further study.

3.7 Conclusions

In this work, we model the production of refractory carbon and nitrogen species CH_4, CO_2, and NH_3 within satellite-forming CPDs through the chemical reaction networks detailed in Prinn & Fegley (1981) and Oberg et al. (2023). We find that the production of NH_3 and CO_2 through the Oberg et al. (2023) networks is viable in satellite-forming CPDs for both static and dynamically evolving material, though the production of NH_3 is less efficient when material is allowed to dynamically evolve. In contrast, we find the chemical reactions to form NH_3 and CH_4 detailed in Prinn & Fegley (1981) are kinetically inhibited in the S17 and B20 satellite-forming CPDs.

We then utilize our dynamic solid growth model to simulate the accretion of enhanced small solids bearing produced refractory carbon and nitrogen species in the S17 and B20 CPDs. We find that, for both the S17 and B20 satellite-forming CPDs at small dust fractions consistent with an optically thin disk, forming satellitesimal seeds do not accrete a significant proportion of enhanced solids bearing refractory carbon and nitrogen species produced through our chemical reaction networks. Even at higher small dust fractions characteristic of those predicted for the protoplanetary disk, we find that forming satellitesimal seeds maintain compositions that are primarily comprised of solids inherited from the protoplanetary disk.

This suggests that in order to form satellites with the necessary carbon and nitrogen inventories for life to originate, refractory carbon and nitrogen species must be supplied directly from the protoplanetary disk. This can occur if refractory carbon and nitrogen species within material infalling onto the CPD are able to survive accretion without undergoing dissociation, or if there is an alternative source of solids capable of delivering refractory carbon and nitrogen species to the CPD such as the capture and ablation of planetesimals (D'Angelo & Podolak, 2015; Ronnet & Johansen, 2020). The viability of these alternative sources for refractory carbon and nitrogen species delivery to growing satellites as well as the feasibility of refractory carbon and nitrogen species surviving incorporation onto the CPD should be the subject of future work.

CHAPTER 4

MODERATELY HIGH OBLIQUITY PROMOTES BIOSPHERIC OXYGENATION

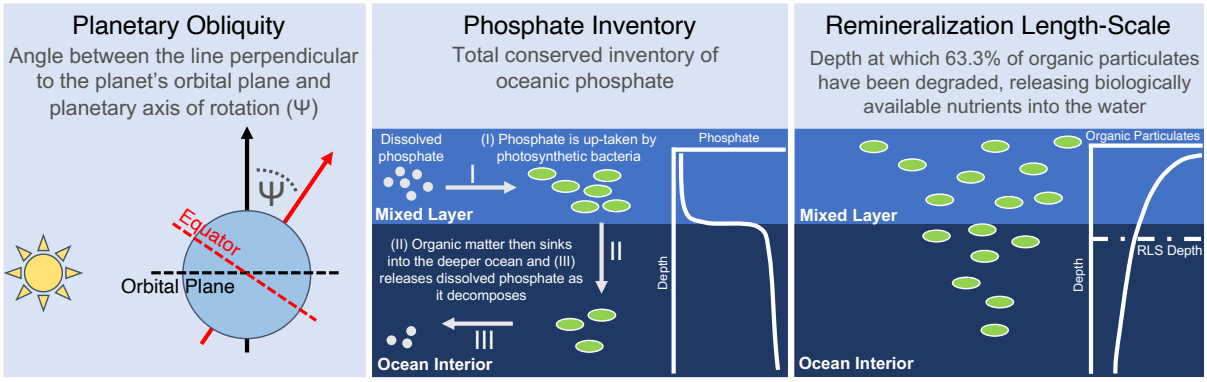

Figure 4.1: Depiction and definitions of parameters of interest varied in models in this paper. The white dash-dotted horizontal line in right-most panel indicates the depth of the remineralization length-scale (RLS) in the schematic.

4.1 Chapter Summary

Planetary obliquity is a first order control on planetary climate and seasonal contrast, which has a number of cascading consequences for life. How moderately high obliquity (obliquities greater than Earth's current obliquity up to 45°) affects a planet's surface physically has been studied previously, but we lack an understanding of how marine life will respond to these conditions. We couple the ROCKE-3D general circulation model to the cGENIE 3D biogeochemical model to simulate the ocean biosphere's response to various planetary obliquities, bioessential nutrient inventories, and biospheric structure. We find that the net rate of photosynthesis increased by 35% and sea-to-air flux of biogenic oxygen doubled between the 0° and 45° obliquity scenarios, which is an equivalent response to doubling bioessential nutrients. Our results suggest that moderately high-obliquity planets have higher potential for biospheric oxygenation than their low-obliquity counterparts and that life on moderately high-obliquity habitable planets may be easier to detect with next generation telescopes. These moderately high-obliquity habitable planets may also be more conducive to the evolution of complex life.

4.2 Introduction

Habitable exoplanets will differ from the Earth in several ways that may affect biogeochemical cycles, biospheric productivity, and biospheric detectability. One potential characteristic that might differ between Earth and exoplanets is planetary obliquity, or the angle between the planet's axis of rotation and orbital axis (Figure 4.1, left-most panel). Planetary obliquity can significantly affect planetary climate. Planets with larger obliquities have larger amplitude seasonal variations (e.g. Williams & Kasting, 1997; Spiegel et al., 2009; Armstrong et al., 2014; Nowajewski et al., 2018; Guendelman & Kaspi, 2019) due to differences in seasonal stellar energy distribution at the planetary surface with increasing obliquity. Moderately high-obliquity planets also experience a more uniform distribution of stellar energy across the planetary surface on annual average, leading these planets to be warmer on average than their low obliquity counterparts (e.g. Linsenmeier et al., 2015; Wang et al., 2016; Nowajewski et al., 2018; Kang, 2019a; Guendelman & Kaspi, 2019; Palubski et al., 2020; Komacek et al., 2021).

There is a wide range of obliquities amongst the terrestrial and giant planets in our solar system, ranging from slight to extreme. The terrestrial planets span a wide range of obliquities, with Mercury and Venus having obliquities very close to 0° (0.1° and 177.4° respectively, with Venus orbiting retrograde) and the Earth and Mars currently having moderate obliquities of 23.4° and 25°, respectively. Earth's obliquity is believed to have varied within the moderate range of 22.1° to 24.5° for at least the past 400 Myr (Williams, 1993), while Mars' obliquity may have varied between 0.2° to $\sim 60^\circ$ over the last 10-45 Myr (Bills, 1990; Laskar & Robutel, 1993; Laskar et al., 2004). Among the outer solar system giant planets, Jupiter, Saturn, and Neptune have obliquities of 3°, 26.7°, and 29.6°, while only Uranus has a much higher obliquity of 98°. These vastly different obliquities and their evolution in our own solar system suggest that exoplanet obliquities likely vary widely as well, though there are currently very few constraints on these measurements for individual exoplanets (Bryan et al., 2020).

Planetary obliquity does not just affect the planet's climate. Olson et al. (2020) used ROCKE-3D (Way et al., 2017), a state-of-the-art ocean-atmosphere general circulation model (GCM), to investigate the effect of planetary obliquity on ocean dynamics and marine habitats. They found that increasing planetary obliquity from 0° to 45° yielded warmer climates and increased seasonal variability of the mixed layer depth (the depth to which the water column is homogeneous due to turbulence and mixing). Olson et al. (2020) argued that ocean circulation patterns changes due to increased planetary obliquity could yield greater nutrient recycling, greater biosphere productivity, and greater biosignature accumulation. However, the GCM used by Olson et al. (2020) lacked explicit representation of life. We address that gap here.

In this work, we couple winds from a general circulation model (ROCKE-3D) with a marine biogeochemical model (cGENIE) to explicitly simulate the response of an Earth-like biosphere to moderately high planetary obliquity (Section 4.3). Section 4.4 describes the biospheric response to various planetary obliquities, phosphate inventories, and biospheric structure. We then discuss our results and their implications for planetary oxygenation, biological evolution, and exoplanet life detection in Section 4.5. These findings are summarized in Section 4.6.

4.3 Methods

We investigate the response of ocean life to planetary obliquity using the ROCKE-3D GCM leveraged by Olson et al. (2020) to force cGENIE, a 3D biogeochemical model originally developed by Ridgwell et al. (2007). cGENIE couples a 3D marine biogeochemistry model to a 3D ocean circulation model with dynamic-thermodynamic sea-ice, all under an energy-moisture balance model (EMBM) with bulk atmospheric chemistry. While cGENIE has historically been used to simulate the geologically recent past and near future, it has since been extended to include a full treatment of methane-based atmospheric chemistry, ocean/atmosphere methane cycling, and methane-based metabolisms to enable the simulation of low oxygen

biospheres (Olson et al., 2013, 2016; Reinhard et al., 2020).

Our experiments use the same topography (current Earth continental configuration minus Greenland) and bathymetry as the original ROCKE-3D experiments from Olson et al. (2020), and we prescribe steady-state surface wind output from their experiments to drive ocean circulation within cGENIE. Prescribing steady-state winds greatly reduces the computational cost of our simulations, allowing us to explore a larger swath of parameter space in our simulations. Using steady-state, rather than time-variable, winds is acceptable because wind-driven upwelling was only weakly sensitive to obliquity in the simulations from Olson et al. (2020). In contrast, the wind-mixed layer depth varied dramatically between seasons in moderately high obliquity scenarios due differences in thermal stratification. It is this mixed layer seasonality that Olson et al. (2020) argued will have the greatest affect on biogeochemical cycles on moderately high-obliquity worlds, and we include this effect in our simulations.

We prescribe an atmosphere with fixed 1% present atmospheric levels (PAL) of oxygen, similar to Proterozoic earth (e.g. Lyons et al., 2014). Prescribing atmospheric oxygen at low levels allows us to explore oxygen dynamics on on planets that have have not yet experienced a large-scale oxygenation despite the presence of oxygenic photosynthesis, like early Earth where biological oxygen production preceded atmospheric oxygenation by several hundred million years (e.g. Planavsky et al., 2014).

Unless otherwise specified, all other model parameters are set at their pre-industrial Earth values (e.g. solar insolation is set at 1368 W/m^{-2} and pCO_2 is set at 278 ppmv). This includes eccentricity, which is equal to 0.0167, with perihelion occurring during the northern hemisphere winter and introducing slight seasonality even in our 0° obliquity scenario.

We consider four different planetary obliquity values, with two low planetary obliquities less than Earth's current obliquity (0° and 15°), and two moderately high planetary obliquities greater than Earth's current obliquity (30° and 45°). We choose these obliquity values to sample the same obliquity space as Olson et al. (2020), whose experiments provided

necessary wind field inputs for our experiments.

In addition to planetary obliquity, we also test the effect of varying two key biosphere parameters. The first of these parameters is the total ocean phosphate inventory. Phosphate (PO_4^{3-}) is the carrier molecule for phosphorus, an essential element that limits biological activity on Earth over geologic timescales (Tyrrell, 1999; Reinhard et al., 2017). As phosphate is a critical nutrient for life, it is important to understand how a range of phosphate inventories would affect life on potential habitable exoplanets.

The second parameter varied in our simulations is the remineralization length-scale (RLS). Organic carbon decays according to the remineralization length-scale within the cGENIE model, implemented as an e-folding depth at which 63.3% of particulate organic carbon (POC) and associated nutrients have been recycled. We vary this length scale to characterize how the depth-distribution of POC remineralization affects nutrient cycles.

We run simulations where these three variables (phosphate inventory, remineralization length-scale, and obliquity) are both varied independently and co-varied, for a total of 80 distinct model configurations. Unless otherwise stated, all other model parameters are set to their present-day Earth values. We run the simulations until steady state is achieved (10,000 years). Then, we calculate both annual and seasonal averages for each model output parameter from the final year of model evolution.

4.4 Results

4.4.1 Planetary Obliquity Scenarios

We first consider the results from a range of obliquity scenarios (0° to 45°) with present-day Earth ocean phosphate inventory and remineralization length-scale to determine planetary obliquity's effect on export POC, the flux of organic carbon produced by photosynthesis that evades remineralization in surface waters and sinks to the deeper ocean–leaving behind oxygen. We additionally quantify the response of sea-to-air oxygen flux resulting from pho-

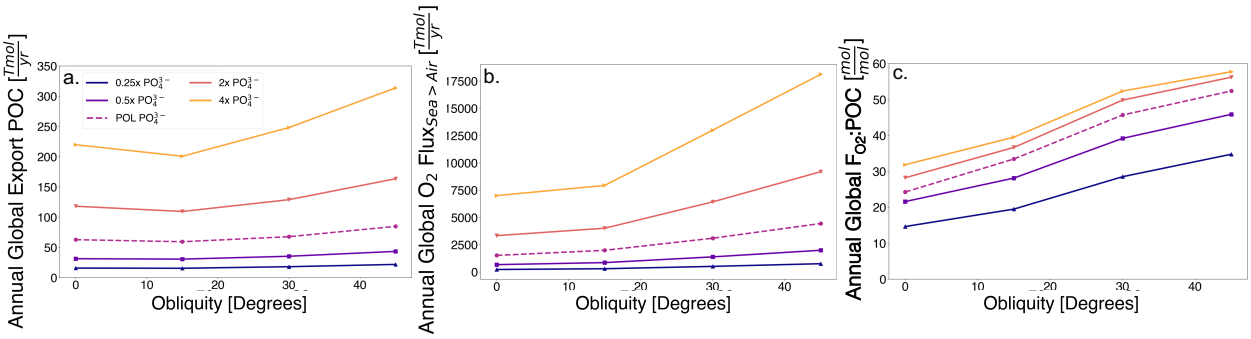

Figure 4.2: Export particulate organic carbon (POC, panel a), oxygen flux (F_{O_2}, panel b), and oxygen flux per unit organic carbon (F_{O_2}:POC, panel c) from varying phosphate levels at different obliquity levels. The POL label stands for present-day ocean levels, and indicates the present-day Earth phosphate inventory scenario. Other scenarios are labeled with their modification factor times present-day ocean levels. Remineralization length-scale is tuned to match chemical profiles from the Earth's present-day ocean and present day obliquity (Ridgwell et al., 2007).

tosynthesis. In these obliquity scenarios (ranging from 0° to 45°), annual total global export POC generally increases with increasing obliquity, with export POC increasing by 35% between the 0° and 45° obliquity scenarios. However, export POC reaches a minimum at 15° obliquity (Figure 4.2a, magenta line), decreasing by 5% between the 0° and 15° obliquity scenarios.

We also see that global oxygen sea-to-air flux (F_{O_2}) increases with obliquity. There is a two-fold increase in F_{O_2} between the 0° obliquity and 45° obliquity scenarios (Figure 4.2b, magenta line). While a portion of this increase in F_{O_2} from the ocean to the atmosphere is a consequence of increased photosynthesis, as evidenced by the increase in export POC values with increasing obliquity, the ratio of F_{O_2} to POC also increases with higher obliquity (Figure 4.2c, magenta line). This increase in F_{O_2}:POC in moderately high-obliquity scenarios suggests that physical effects caused by moderately high obliquity also contribute to the increase in F_{O_2} with higher obliquity.

4.4.2 Biospheric Sensitivity to Phosphate

We then simulate oceans with a range of phosphate inventories and planetary obliquity values. Increasing phosphate inventory in our simulations has an $\sim$ 1:1 effect on increasing export POC (Figure 4.2a). The phosphate inventory also affects the biospheric response to obliquity. The biosphere is relatively insensitive to obliquity when phosphate is scarce (0.25 - 0.5x POL), but export POC becomes increasingly sensitive to obliquity under phosphate replete conditions (2-4x POL).

This same trend is seen in F_{O_2} values as well (Figure 4.2b). At low phosphate inventory levels, F_{O_2} is relatively unaffected by obliquity. However, F_{O_2} increases more strongly with obliquity when phosphate is more abundant. At high phosphate inventory (2-4x POL), increasing obliquity from 0° to 45° yields greater that 2x F_{O_2}, an effect similar to doubling the phosphate inventory.

The ratio of F_{O_2} from sea-to-air to unit export POC experiences a similar two-fold increase with obliquity increase from 0° to 45° as is caused by a doubling of phosphate inventory (Figure 4.2c). Unlike for F_{O_2} values, scenarios at every phosphate inventory value experienced a doubling in F_{O_2}:POC ratio with an obliquity increase from 0° to 45°.

4.4.3 Biospheric Sensitivity to Remineralization Length-Scale

As POC sinks through the water column, nutrients are made re-available for metabolic reactions such as photosynthesis through remineralization at depth and transport back to the photic zone. Remineralization is the first step in this process, and occurs throughout the water column. The remineralization length-scale affects the vertical distribution of nutrients in the water column and the timescale for their return to the surface. When remineralization length-scales are longer, nutrient containing particles are able to settle deeper into the water column on average before they are processed and made available for transport back to the surface, leading to greater accumulation of nutrients at depth.

Simulations with shallower remineralization length scales displayed increased POC export

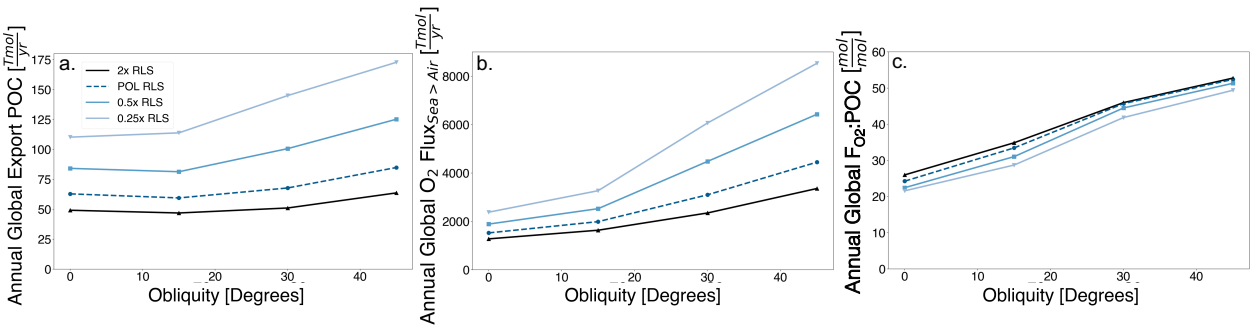

Figure 4.3: Export particulate organic carbon (POC, panel a), oxygen flux (F_{O_2}, panel b), and oxygen flux per unit organic carbon (F_{O_2}:POC, panel c) for scenarios with various remineralization length-scales (each scenario is labeled by the modifying factor times remineralization length-scale) at different obliquity levels. Phosphate inventory in each of these experiments is set to POL.

and biosphere activity (Figure 4.3a). The increase in POC export with shallower remineralization occurs because nutrients do not settle as far into the deep ocean and nutrients are more readily returned to the surface via wind-driven upwelling.

We find that export POC only slightly increases with obliquity for experiments with longer remineralization length scales. However, export POC increases with higher obliquity for scenarios with shorter remineralization length-scales (0.25 - 0.5x present ocean levels, or POL, Figure 4.3a). F_{O_2} increases by ∼3-4x with increasing obliquity and decreasing remineralization length-scale in all our sensitivity experiments at POL phosphate inventory (Figure 4.3b). Moderately high obliquity is a stronger driver of F_{O_2} increase than remineralization length-scale decrease, as halving remineralization length-scale causes an increase in F_{O_2} of approximately 50%, while increasing obliquity from 0° to 45° results in greater than double F_{O_2} ($\geq$ 100% increase).

The ratio of F_{O_2} to export POC increases with increasing obliquity (Figure 4.3c) for all simulated remineralization length-scales. This result also supports our assertion that physical changes caused by increasing obliquity are partially responsible for the observed increase in F_{O_2}.

Additionally, we find that while F_{O_2} and POC alone decrease with deeper remineral-

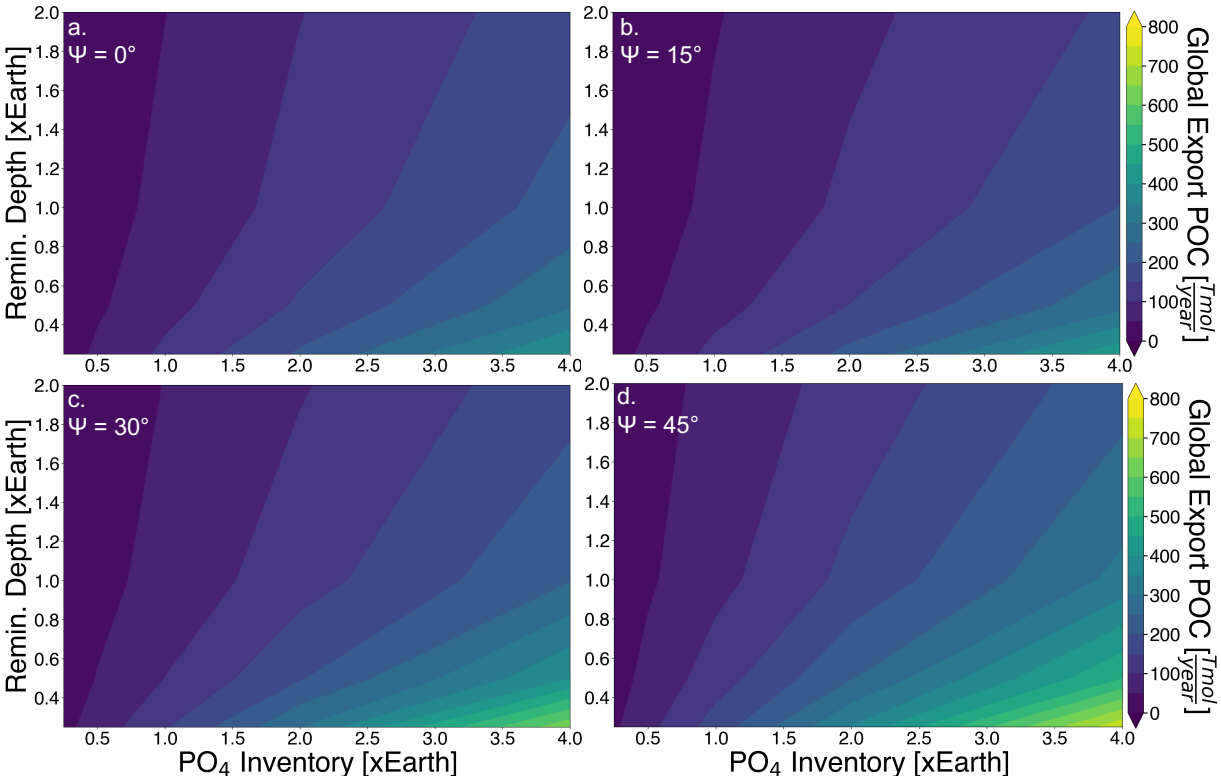

Figure 4.4: Global annual export particulate organic carbon for simulations with covaried phosphate inventory, remineralization length-scale, and obliquity. We consider obliquities of 0° (panel a), 15° (panel b), 30°(panel c), and 45° (panel d). Annual global export POC increases with increasing phosphate inventory (4.2, decreasing remineralization length-scale (4.3), and increasing obliquity.

ization length-scales, F_{O_2}:POC ratio increases with deeper remineralization length-scales. F_{O_2} and export POC decrease with increasing remineralization length-scale as when the remineralization length-scale is deeper, nutrients sink to deeper levels in the water column and decrease the amount of nutrients available for the surface biosphere. A decrease in photosynthesis due to a reduction of nutrients then leads to a decrease in oxygen production, and by extension F_{O_2} decrease. However, when we look at the F_{O_2}:POC ratio, we see this ratio increase with deeper remineralization depths. Although both F_{O_2} and POC decrease with increasing RLS, F_{O_2}:POC increases because deeper remineralization results in less near surface oxygen consumption.

4.4.4 Additional Experiments

We ran a series of experiments in which we covaried obliquity, remineralization length-scale, and phosphate inventory to explore potential synergistic effects introduced through covariance of these variables. Such effects could have profound implications for the potential for oxygen build-up on Earth-sized exoplanets.

The general trends for export POC, F_{O_2}, and F_{O_2}:POC ratio in response to increasing obliquity, phosphate inventory, and remineralization length-scale previously discussed in sections 3.1, 3.2, and 3.3 continue to hold true in the co-varying simulations (Figures 4.4, 4.5, 4.6). Both export POC and F_{O_2} increase most strongly in response to increasing phosphate inventory, with second order increases driven by decreasing remineralization length-scale and increasing obliquity. When we increase phosphate inventory and decrease remineralization length-scale in tandem, a synergistic effect is present. We find that scenarios with increased phosphate inventory and decreased remineralization depth yield >2x export POC and F_{O_2} levels than the sum of two independent scenarios with increased phosphate inventory and decreased remineralization length-scale.

4.5 Discussion

4.5.1 Increased Obliquity Drives Enhanced Biological Activity and Atmospheric Oxygenation

The general increase in export POC with higher obliquity is driven by increased nutrient availability. As discussed earlier, Olson et al. (2020) predicted that increased seasonal deepening of the mixed layer depth with increasing obliquity during each hemisphere's winter would lead to increased nutrient cycling. This increased seasonal deepening of the mixed layer depth occurs with increasing obliquity in our scenarios as well (Figure 4.7a).

Seasonal deepening of mixed layer depth in the winter hemisphere intensifies with increasing obliquity because as obliquity increases, the winter hemisphere receives less incident

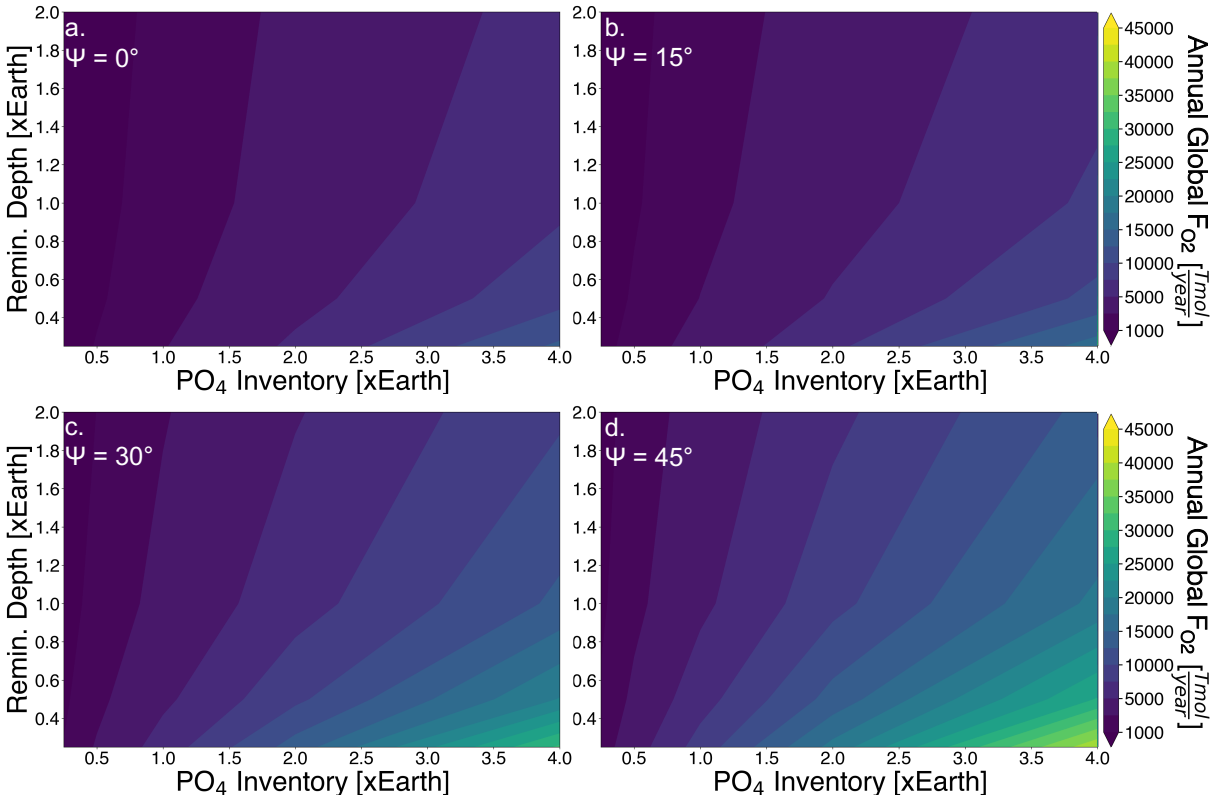

Figure 4.5: Annual global F_{O_2} for simulations with covaried phosphate inventory, remineralization length-scale, and obliquity. We consider obliquities of 0° (panel a), 15° (panel b), 30° (panel c), and 45° (panel d). As seen in the single variable models, annual global F_{O_2} increases with increasing phosphate inventory, decreasing remineralization length-scale, and increasing obliquity.

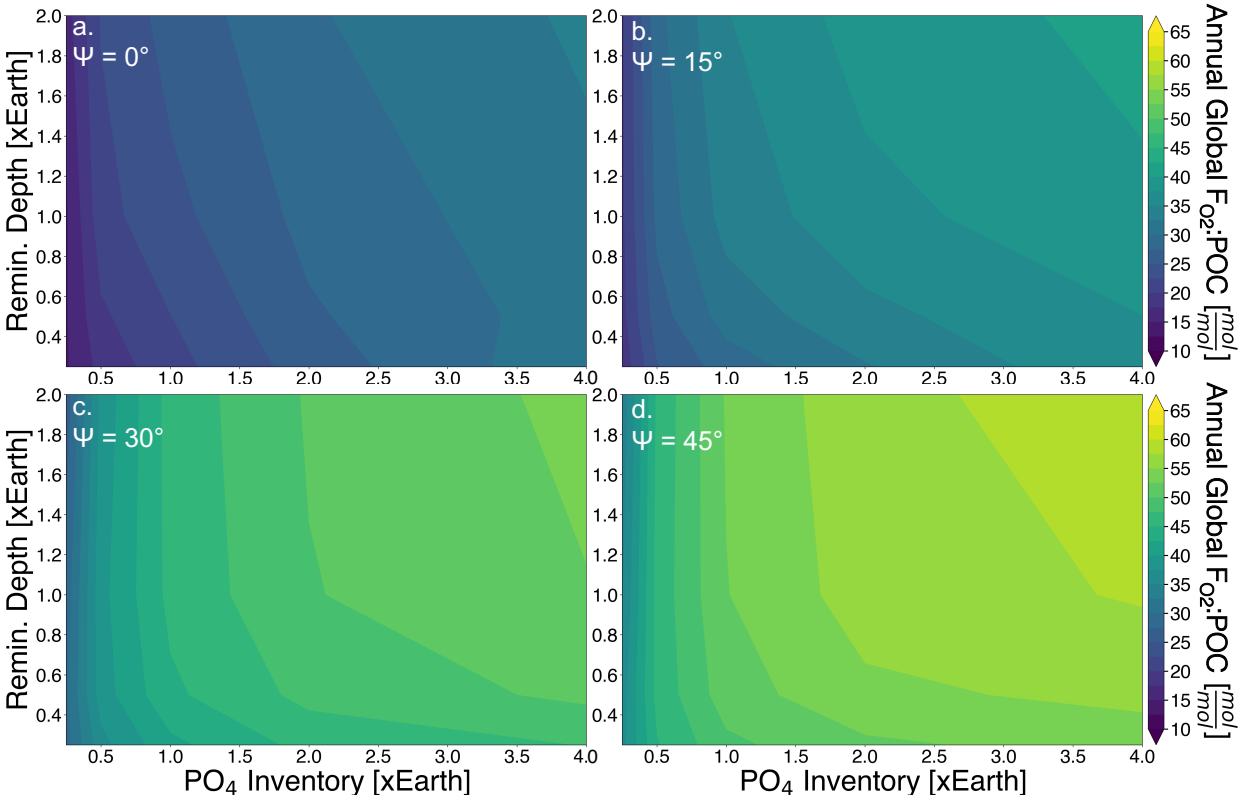

Figure 4.6: Annual global F_{O_2} per unit POC for simulations with covaried phosphate inventory, remineralization length-scale, and obliquity. We consider obliquities of 0° (panel a), 15° (panel b), 30°(panel c), and 45° (panel d). Global average F_{O_2}:POC increases with increasing phosphate inventory, increasing remineralization length-scale, and increasing obliquity.

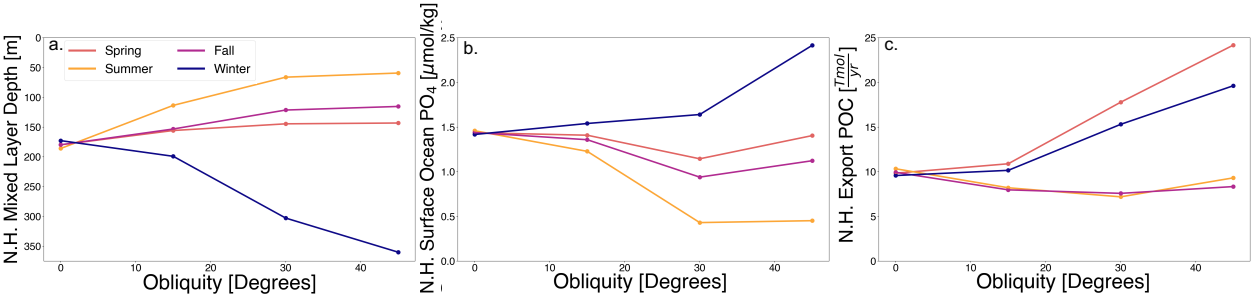

Figure 4.7: Seasonal Northern Hemisphere (N.H.) values for average mixed layer depth (panel a), total surface ocean PO_4 (panel b), and total export POC (panel c).

insolation. Reduced incident insolation leads to colder sea surface temperatures and weakened water density stratification, resulting in a deeper mixed layer depth. Deeper mixed layer depths allow for increased entrainment of nutrients from depth, resulting in higher surface phosphate concentrations (Figure 4.7b).

Varying seasonal nutrient availability significantly affects biological primary productivity throughout the year. In the 0° obliquity scenario, POC export rates do not significantly vary throughout the year due to the lack of seasons (the slight variation between seasons displayed is due to the planet's non-zero eccentricity). However, for obliquity scenarios of 15° or higher, spring has the highest rate of POC export, followed by winter (Figure 4.7c). In the 45° obliquity scenario, spring export POC increases by approximately 2.5x in comparison to the 0° obliquity scenario, while winter export POC increases by a factor of two when compared to the 0° obliquity scenario. In the non-zero degree obliquity scenarios, fall and summer have the lowest rates of POC export with summer POC export at slightly higher rates than in the fall.

POC export in the winter exceeds POC export in summer and fall due to enhanced nutrient inventories in the surface ocean (Figure 4.7c). These nutrient rich waters are dredged up by the deepened mixed layer in these moderately high obliquity scenarios. However, although winter surface waters have an enhanced nutrient inventory, these nutrients cannot be entirely utilized due to reduced insolation during the winter. This inhibits biological activity, and therefore limits POC export until the spring. When winter ends, a "spring bloom" of heightened biological activity occurs when incident insolation begins to increase again after the dark winter season and provides residual nutrient rich waters with light. Biological activity increases dramatically, fueled by both sufficient light and abundant nutrients, and leads to the observed maximum POC export in spring (Figure 4.7c). As a result of the deepened mixed layer and enhanced winter nutrient availability, the increases in seasonal export POC for moderately high obliquity scenarios lead to the observed increase in annual export POC with obliquity.

Though light and temperature do have significant effects on POC export in general, in our simulations these effects are negligible compared to the effect of nutrient availability. As obliquity increases, light is more evenly distributed over the planetary surface on annual average but the total amount of light the planet's surface receives does not change and so light cannot be the cause of the observed increased annual export POC. Moderately high obliquity increases the amount of incident irradiation on a hemisphere during the summer months, and decreases it during the winter months. One might then expect an increase in export POC during the summer, and a decrease in the winter, which is not observed in our results due to the overriding effect of nutrient availability. Additionally, in cGENIE's temperature-dependent export scheme, export POC increases with increasing temperature. One may then expect that larger temperature extremes due to increased seasonality would lead to increased export POC in the summer and decreased export POC in the winter. However, as we instead see that winter export POC surpasses summer export POC (Figure 4.7c), we conclude that nutrient availability is the dominant factor affecting export POC.

We find that both export POC and sea-to-air oxygen flux increase with increasing obliquity (Figures 4.2, 4.3, 4.4, and 4.5). This increase in F_{O_2} is a direct consequence of increased biological activity; as biological activity increases there are more photosynthetic organisms performing photosynthesis, resulting in an increase in biogenic oxygen production. An interesting consequence of increased obliquity, however, is the effect of increasing obliquity on annual global oxygen flux per unit export POC. This increase implies that increased oxygen flux cannot be solely attributed to the increase in export POC.

If the increase in F_{O_2} with increasing obliquity was simply due to the increase in export POC with obliquity, the F_{O_2}:POC ratio would be constant across all considered planetary obliquity values as produced oxygen would scale proportionally with increased primary productivity, which it is not (Figure 4.2). An increase in F_{O_2}:POC implies that physical effects are likely amplifying the increase in F_{O_2} with increasing obliquity.

The physical effects responsible for amplifying F_{O_2} increase with higher obliquity are

decreased sea surface ice coverage and decreased solubility of oxygen in warmer water. Higher obliquity results in a more even distribution of insolation over the planetary surface. This leads to a decrease in the global average percentage of sea ice coverage as obliquity increases (Figure 4.8 a,c,e,g) and warmer waters due to higher incident irradiation at the poles. As the sea ice coverage decreases due to the increase in obliquity and increase in ocean water temperature, a corresponding increase in oxygen flux from those now uncovered areas at high latitudes occurs (Figure 4.8 b,d,f,h). The resulting increase in oxygen flux occurs because (1) without ice coverage, these areas of open ocean are now able to exchange oxygen with the atmosphere with no physical barrier impeding gas exchange and (2) oxygen is less soluble in warmer water (e.g. Wanninkhof, 2014). Therefore, higher photosynthesis rates at the poles leads to enhanced sea-to-air fluxes of biogenic oxygen due to the combined effects of increased surface area available for gas exchange and warmer ocean temperatures.

4.5.2 Moderately High Obliquity Increases Biosphere Detectability

Atmospheric oxygen may be a remotely detectable signature of life on other planets (e.g. Meadows et al., 2018). Although current telescopes are not designed to detect biotic levels of oxygen in exoplanet atmospheres (Lustig-Yaeger et al., 2019), next generation telescopes such as the LUVOIR-like observatory recommended by the Astro2020 Decadal Survey would be able to detect biotic levels of oxygen in exoplanet atmospheres depending on cloud conditions and exposure times (Wang et al., 2018). As we have shown in our experiments, moderately high-obliquity planets have higher annual global oxygen fluxes from sea to air than their low obliquity equivalents (Figures 4.2b, 4.3b, 4.5a-d). Therefore, biospheres on moderately high-obliquity exoplanets may be easier to detect than on their equivalent low obliquity counterparts due to their higher atmospheric oxygenation potential.

Oxygen is not the only potential biosignature that is enhanced by moderately high obliquity. Olson et al. (2018) explored the potential for the use of seasonality as a biosignature, in which the seasonal increase and decrease of biogenic gases such as CO_2, CH_4, O_2, and

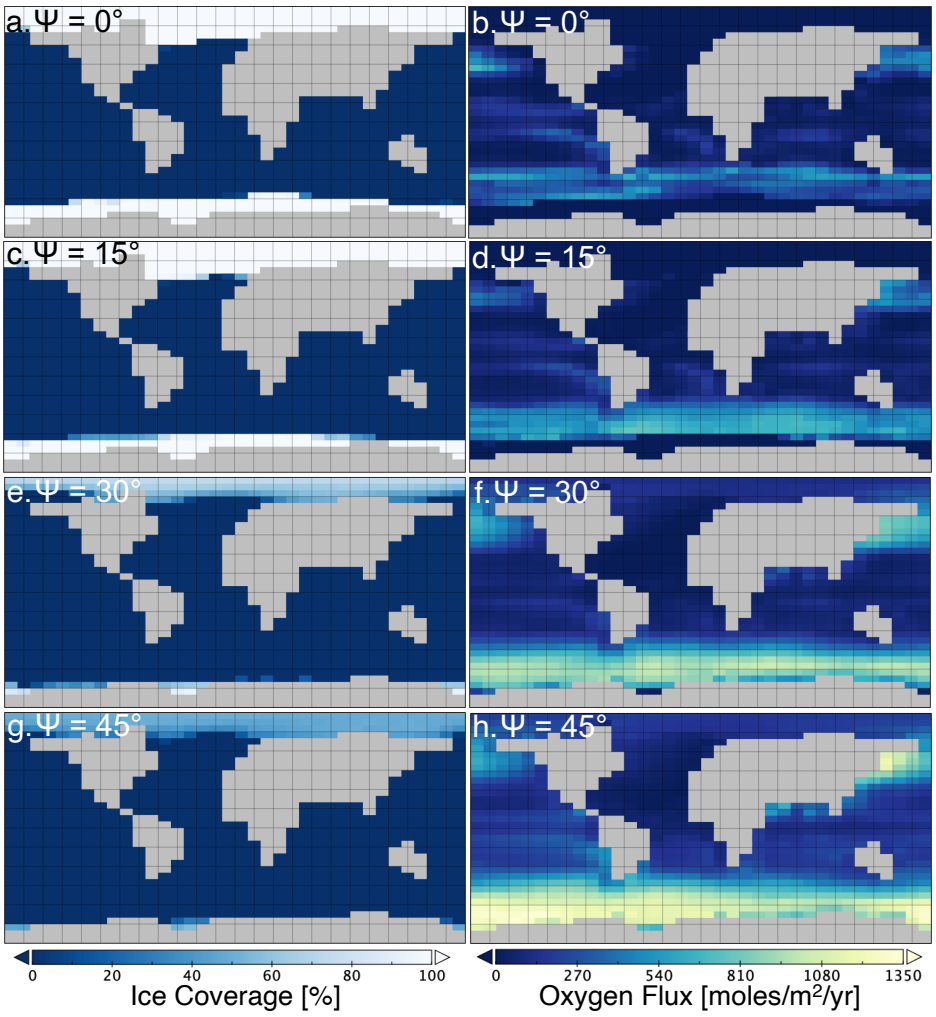

Figure 4.8: Global maps of annual average sea ice cover percentage and oxygen flux for simulations with POL phosphate inventory and remineralization length-scale. We consider obliquities of 0° (panels a/b), 15° (panels c/d), 30°(panels e/f), and 45° (panels g/h). The left color bar denotes the percentage sea ice cover in each area box, while the right colorbar denotes annual average oxygen flux from each quadrant. The grey regions correspond to areas of land coverage, where ice coverage and oxygen flux are not measured.

O_3 due to seasonal variation in insolation could be detectable by a LUVOIR-like instrument and indicate the presence of an active biosphere. As we have seen here on Earth, CO_2 and O_2 oscillate seasonally due to changes in the balance of photosynthesis (draw down CO_2, make O_2) and respiration (release CO_2, consume O_2) (Keeling et al., 2001). While Earth has relatively moderate seasonality, exoplanets with higher obliquities would have more intense seasonality with large changes in temperature. As seasonal changes in the environment manifest as changes in atmospheric composition, larger seasonal differences may result in a larger, more detectable atmospheric signal (Olson et al., 2018).

4.5.3 Challenges for Life on Moderately High-Obliquity planets

While aquatic life is protected from seasonality due to the high heat capacity of water, land environments may experience extreme seasonality on moderately high-obliquity planets. This could be a problem because terrestrial microbes and ectothermic organisms are unable to regulate their own body temperatures (e.g. Wright & Cooper, 1981; Cossins & Bowler, 1987; Huey & Kingsolver, 1989; Hochachka & Somero, 2016) and therefore would be unlikely to survive the temperature extremes on land resulting from increased seasonality (similar to predictions by Paaijmans et al., 2013, of exotherm response to temperature variations caused by climate change on Earth). Additionally, while evolved terrestrial life that self-regulates body temperature (endotherms) can survive more extreme temperatures than ectotherms (e.g. Scholander et al., 1950; Irving & Krog, 1954; Heinrich, 1977; Lovegrove et al., 1991; McNab, 2002), many adaptations to either extremely cold or hot environments are incompatible, such as fur or blubber.

Intensified seasonality does not have to be a death sentence for terrestrial life on moderately high-obliquity planets, however. Multiple microbial species and a few multi-cellular species have been discovered living in extreme environments on Earth, including those at extremely cold and hot temperatures (e.g. Cavicchioli, 2002). Life evolving on a planet with extreme seasons could potentially adapt to both extreme warm and cold climates, and

ultimately be more resilient against sudden environmental changes or mass extinctions.

Another potential problem for the origin and evolution of life on moderately high-obliquity planets is water loss. Kang (2019b) found that high-obliquity planets have a much higher seasonal stratospheric water vapor abundance in comparison to equivalent low obliquity planets, which may allow more water vapor to be lost due to photodissociation and hydrodynamic escape of hydrogen to space. This potential for increased water loss suggests that liquid water on high-obliquity planet surfaces could be lost quickly, potentially endangering the origin/evolution of life on these planets as liquid water is a key requirement for life. However, Kang (2019b) was looking at planets with obliquities higher than those considered in this work, so moderately high-obliquity planet atmospheres may not experience the wetter stratospheres seen in higher-obliquity planet atmospheres. Additionally, potential water loss may be mitigated by the fact that wetter stratospheres only occurred seasonally in simulations from Kang (2019b), and may average out to negligible increased water loss on long-term average for high-obliquity exoplanets and their moderately high-obliquity counterparts.

4.5.4 Opportunities for Future Work

Our results suggest that moderately high-obliquity planets may experience both higher export POC production and higher oxygenation potential than their low-obliquity counterparts. However, as we only simulate planetary obliquities up to 45°, it is still unknown how the biospheres on higher-obliquity planets will fare under the physical and climatic changes that occur at higher obliquities. At planetary obliquities greater than 54°, the planet enters a different climate regime where the poles begin to receive more incident insolation than the equatorial regions, potentially leading to the formation of equatorial ice belts (e.g. Rose et al., 2017; Kilic et al., 2017, 2018; Colose et al., 2019). These equatorial ice belts would cause changes to both ocean circulation and surface wind fields, which may have significant effects on biospheric activity. We did not explore these obliquity scenarios because imposing annually averaged winds from ROCKE-3D would likely become an increasingly poor assumption

at very high obliquities. Modeling biospheric dynamics and oxygenation potential on planets with higher obliquities remains an opportunity for future work.

4.6 Conclusions

We simulated Earth-like marine life on an Earth-sized planet at various obliquities. We found that moderately high obliquity promotes increased photosynthetic activity and associated oxygen flux to the atmosphere, potentially enhancing atmospheric oxygenation. Sea-to-air oxygen fluxes are further amplified by decreasing sea surface ice coverage at high latitudes on moderately high-obliquity planets, exposing greater ocean surface area for sea-to-air gas exchange. This oxygenation may ultimately be beneficial for the evolution of complex life on moderately high-obliquity planets (e.g. Catling et al., 2005; Reinhard et al., 2016). In short, our results suggest that life may not just survive, but also thrive at moderately high obliquity.

Active biospheres may be easier to detect on moderately high-obliquity planets as well. Increased planetary oxygenation on moderately high-obliquity planets could result in easier detection of biogenic oxygen on moderately high-obliquity planets with next generation telescope concepts and potential earlier evolution of complex life (e.g. Catling et al., 2005; Reinhard et al., 2016). Additionally, life on moderately high-obliquity planets may be easier to detect through heightened variations in biosignature gases over more intense seasonal cycles. Given the potential for increased biological activity and oxygenation on moderately high-obliquity planets, the habitability and biosignatures of moderately high-obliquity planets are exciting opportunities for future work.

CHAPTER 5

CONCLUSION

Through the work presented in this thesis, I have modeled and evaluated the extent to which the formation and subsequent evolution of planetary bodies contributes to potential habitability. In Chapter 2, I explore the how a luminous planetary core effects the solids that it ultimately accretes. I find that a critical transition occurs where very hot (rapidly accreting) cores drive off volatiles prior to accretion, while cool cores (slowly accreting) are able to inherit volatile-rich solids. My work serves to place an upper limit on the mass accretion rate onto the Jovian core, and by extension the effective temperature of the core, where this critical transition occurs that would allow the chemical constraints inferred for Jupiter's formation to be met. I find that for a 5 $M_\oplus$ core, this implies that $\dot{M} \lesssim 10^{-10}$ $M_\odot$ yr^{-1} to stay below the critical temperature where nitrogen is driven off of infalling solids, T_{core} <2000 K. Lower mass cores were found to have even lower limits on the the critical mass accretion rate needed to maintain frozen N_2.

While my work demonstrates that enhancement of nitrogen in the Jovian atmosphere is possible through the accretion of nitrogen-rich solids, it also shows that thermal processing driven by forming giant planet core luminosity is a significant side-effect of giant planet core formation which should be considered when studying the effect of giant planet core formation on the surrounding protoplanetary disk and material. Subsequent work considering the atmospheric recycling of volatiles by pebble-accreting planets has taken into consideration my work detailing thermal processing of accreted solids during giant planet core formation, noting that this effect could drive additional volatiles beyond nitrogen off of accreted pebbles and yielding vapor-poor planetary envelopes (Wang et al., 2023). The effect of the luminosity from a forming giant planet core on additional volatile species should be studied in the future.

In Chapter 3, I model the production of refractory carbon and nitrogen species CH_4, CO_2, and NH_4 within satellite-forming CPDs (Shibaike et al., 2017; Batygin & Morbidelli, 2020) through the chemical reaction networks detailed in Prinn & Fegley (1981) and Oberg et al. (2022, 2023). I then utilize my dynamic solid growth model to simulate the accretion of solids bearing produced refractory carbon and nitrogen species in the studied CPDs. I find

that, for the satellite-forming CPDs modeled, forming satellites do not accrete a significant proportion of solids bearing refractory carbon and nitrogen species produced through our chemical reaction networks.

As the satellite-forming CPDs I model surround a Jupiter-sized central planet orbiting at Jupiter's current orbital separation from the sun, these satellite-forming CPDs would form icy satellites analogous to the Galilean satellites. Therefore, my work can potentially serve to provide context for observations by upcoming and recently launched missions to the Galilean icy moons such as the NASA Europa CLIPPER and ESA JUICE missions. The NASA Europa CLIPPER is a remote sensing mission currently scheduled to be launched on October 10th, 2024 with the main goal of determining whether Europa harbors a sub-surface liquid water ocean under its icy shell. Through this mission, NASA aims to determine the thickness of the ice layer, definitively detect the presence of a sub-surface ocean, characterize the ice layer and the potential sub-surface ocean floor, and detect potential geysers that may errupt from the Europa surface (Phillips & Pappalardo, 2014; Bayer et al., 2015; Cochrane et al., 2023). Similarly, the ESA JUICE mission was launched in April 2023 with the main goal of taking detailed observations of Jupiter and the three Galilean moons evidenced to have sub-surface oceans, Europa, Callisto, and Ganymede.

Though neither mission will be able to directly sample the composition of Europa, Callisto, or Ganymede's potential subsurface oceans, spectrometer measurements of vapor off-gassed from any detected plumes or geysers would provide an indirect measurement of sub-surface ocean composition (e.g. similar to spectrometer measurements from Enceladus plumes discussed in Porco et al., 2006; Hansen et al., 2006; Hao et al., 2022). The identities and abundances (or lack there-of) of biocritical element-bearing molecules, when viewed through the lens of my work simulating the production of refractory carbon and nitrogen species in satellite-forming CPDs, could provide insight into the potential environment of the Jovian CPD and CPD material infall scenario. Also, if there are biocritical element-bearing molecules present in spectral observations which I predicted would not form within

satellite-forming CPDs, this might provide further motivation to investigate additional chemical processing pathways or refractory carbon and nitrogen bearing solid sources such as is suggested in Section 4.6.

Additionally, as telescope resolution continues to improve, the astronomy and planetary science fields are moving closer to being able to detect smaller objects such as CPDs within protoplanetary disks. There is currently strong evidence indicating the positive detection of three circumplanetary disks within the PDS-70 and SR 12 protoplanetary disks (Christiaens et al., 2019; Benisty et al., 2021; Wu et al., 2022). Two of the detected planets within PDS-70, PDS-70b and PDS-70c, are believed to be actively forming giant planets (Wagner et al., 2018; Keppler et al., 2018; Haffert et al., 2019; Wang et al., 2020). When these growing planets were studied more closely, observations suggested the presence of active circumplanetary disks around PDS-70b and PDS-70c (Christiaens et al., 2019; Benisty et al., 2021), marking the first reported positive detections of CPDs. These CPD discoveries were then followed up by the detection of a potential planetary companion object around SR 12c, which is believed to also be a CPD (Wu et al., 2022).

With future technological advances in telescope resolution, it may be possible to observe chemical signatures from the production of detectable refractory carbon and nitrogen species or intermediates, such as NH_2, NH_3, and CO_2. These observations could serve as a test to determine whether the chemical processing I have modeled is occurring within a range of different circumplanetary disks. Additionally, these observations could also serve to determine whether the shocking of material upon infall onto the CPD is common within circumplanetary disks and whether this shocking affects the composition of material as currently theorized.

Finally, in Chapter 4 I couple the ROCKE-3D general circulation model to the cGENIE 3D biogeochemical model to simulate the response of the ocean biosphere on an Earth-sized planet to various planetary obliquities, bioessential nutrient inventories, and biospheric structure. Through these simulations, I find that the net rate of photosynthesis increased

by 35% while the sea-to-air flux of biogenic oxygen doubled by increasing obliquity from 0° to 45° - an equivalent response to doubling bioessential nutrients. My results suggest that moderately high obliquity planets have higher potential for biospheric oxygenation than those with low obliquity, and that life originating on planets with moderately high obliquity may be easier to detect through upcoming high resolution telescopes.

My work investigating the potential biospheric oxygenation of Earth-sized planets with moderately high obliquity has served to highlight a parameter of importance for the search for life on exoplanets. Expanding upon my work in Chapter 4, Jernigan et al. (2023) tested the biospheric activity within oceans on Earth-sized planets with obliquities greater than 45° and a range of orbital eccentricities, finding that marine biological activity increases both with obliquities beyond 45° and with increasing orbital eccentricities up to 0.4. In fact, planets with obliquities beyond 45° and eccentricities higher than zero were found to potentially be superhabitable worlds that are favorable not only for the origination and survival of life, but also for the detection of exoplanet life.

In the future, work should be done to further investigate the potential habitability of planets with more extreme or different physical characteristics than Earth. As discussed in Section 4.5, potential enhanced water loss from high obliquity planets could place a constraint on the time window for planetary habitability (e.g. Kasting, 1988; Meadows et al., 2018; Kang, 2019b). This effect should be revisited to determine whether there are scenarios under which potential water loss is mitigated or eliminated completely. Additionally, both Jernigan et al. (2023) and I assume a present-day Earth continental configuration in our models. However, terrestrial exoplanets with continents will almost certainly not have the same continental configuration or percentage continental coverage currently seen on present-day Earth, as even Earth's continental configuration has changed drastically over time (as reviewed in Bradley, 2011). As continent configuration affects ocean circulation (e.g. von der Heydt & Dijkstra, 2006, 2008), different continental configurations may yield different results for planetary biospheric oxygenation potential and habitability.

REFERENCES

Akimkin, V., Zhukovska, S., Wiebe, D., et al. 2013, The Astrophysical Journal, 766, 8

Alexander, R. 2008, New Astronomy Reviews, 52, 60

Ali-Dib, M., Mousis, O., Petit, J.-M., & Lunine, J. I. 2014, The Astrophysical Journal, 785, 125

Alibert, Y., Mousis, O., & Benz, W. 2005, Astronomy & Astrophysics, 439, 1205

Anderson, D. E., Blake, G. A., Cleeves, L. I., et al. 2021, The Astrophysical Journal, 909, 55

Anderson, R. C., Dohm, J. M., Haldemann, A. F. C., Hare, T. M., & Baker, V. R. 2004, Icarus, 171, 31

Aoyama, Y., Ikoma, M., & Tanigawa, T. 2018, The Astrophysical Journal, 866, 84

Armstrong, J., Barnes, R., Domagal-Goldman, S., et al. 2014, Astrobiology, 14, 277

Arvidson, R. E., Ashley, J. W., Bell III, J. F., et al. 2011, Journal of Geophysical Research: Planets, 116, doi:10.1029/2010JE003746

Atreya, S., Wong, M., Owen, T., et al. 1999, Planetary and Space Science, 47, 1243

Atreya, S. K., Mahaffy, P. R., Niemann, H. B., Wong, M. H., & Owen, T. C. 2003, Planetary and Space Science, 51, 105

Ayliffe, B. A., & Bate, M. R. 2009, Monthly Notices of the Royal Astronomical Society, 393, 49

Barnett, M. N., & Ciesla, F. J. 2022, The Astrophysical Journal, 925, 141

Barnett, M. N., & Olson, S. L. 2022, The Planetary Science Journal, 3, 132

Bate, M. R., Lubow, S. H., Ogilvie, G. I., & Miller, K. A. 2003, Monthly Notices of the Royal Astronomical Society, 341, 213

Batygin, K., & Morbidelli, A. 2020, The Astrophysical Journal, 894, 143

Bayer, T., Cooke, B., Gontijo, I., & Kirby, K. 2015, in 2015 IEEE Aerospace Conference, 1–12

Beckwith, S. V. W., Henning, T., & Nakagawa, Y. 1999, arXiv:astro-ph/9902241

Benisty, M., Bae, J., Facchini, S., et al. 2021, The Astrophysical Journal Letters, 916, L2

Bergin, E. A., Blake, G. A., Ciesla, F., Hirschmann, M. M., & Li, J. 2015, Proceedings of the National Academy of Sciences, 112, 8965

Beuther, H., Klessen, R. S., Dullemond, C. P., & Henning, T. K. 2014, Protostars and Planets VI (University of Arizona Press)

Bills, B. G. 1990, Journal of Geophysical Research: Solid Earth, 95, 14137

Birnstiel, T., Dullemond, C. P., & Brauer, F. 2010, Astronomy & Astrophysics, 513, A79

Birnstiel, T., Klahr, H., & Ercolano, B. 2012, Astronomy & Astrophysics, 539, A148

Birnstiel, T., Ormel, C. W., & Dullemond, C. P. 2011, Astronomy & Astrophysics, 525, A11

Bisschop, S. E., Fraser, H. J., Öberg, K. I., van Dishoeck, E. F., & Schlemmer, S. 2006, Astronomy & Astrophysics, 449, 1297

Bitsch, B., Lambrechts, M., & Johansen, A. 2015, Astronomy & Astrophysics, 582, A112

Borucki, W. J., Koch, D., Basri, G., et al. 2010, Science, 327, 977

Bosman, A. D., Cridland, A. J., & Miguel, Y. 2019, Astronomy & Astrophysics, 632, L11

Bosman, A. D., Walsh, C., & Dishoeck, E. F. v. 2018, Astronomy & Astrophysics, 618, A182

Boss, A. P. 1997, Science, 276, 1836

—. 2002, Earth and Planetary Science Letters, 202, 513

Bradley, D. C. 2011, Earth-Science Reviews, 108, 16

Bryan, M. L., Chiang, E., Bowler, B. P., et al. 2020, The Astronomical Journal, 159, 181

Béghin, C., Sotin, C., & Hamelin, M. 2010, Comptes Rendus Geoscience, 342, 425

Béghin, C., Canu, P., Karkoschka, E., et al. 2009, Planetary and Space Science, 57, 1872

Canup, R. M., & Ward, W. R. 2002, The Astronomical Journal, 124, 3404

—. 2006, Nature, 441, 834

—. 2008, arXiv:0812.4995 [astro-ph]

Capone, D. G., Popa, R., Flood, B., & Nealson, K. H. 2006, Science, 312, 708

Carr, M. H., Belton, M. J. S., Chapman, C. R., et al. 1998, Nature, 391, 363

Castillo-Rogez, J. C. 2011, Icarus, 215, 599

Castillo-Rogez, J. C., & McCord, T. B. 2010, Icarus, 205, 443

Castillo-Rogez, J. C., & Lunine, J. I. 2010, Geophysical Research Letters, 37, doi:10.1029/2010GL044398

Catling, D. C., Glein, C. R., Zahnle, K. J., & McKay, C. P. 2005, Astrobiology, 5, 415

Cavicchioli, R. 2002, Astrobiology, 2, 281

Chambers, J. 2017, The Astrophysical Journal, 849, 30

Chambers, J. E. 2014, Icarus, 233, 83

Christensen, P. R., Bandfield, J. L., Bell III, J. F., et al. 2003, Science, 300, 2056

Christiaens, V., Cantalloube, F., Casassus, S., et al. 2019, The Astrophysical Journal Letters, 877, L33

Chyba, C. F., Thomas, P. J., Brookshaw, L., & Sagan, C. 1990, Science, 249, 366

Ciesla, F. J. 2007, Science, 318, 613

—. 2009, Icarus, 200, 655

—. 2010, The Astrophysical Journal, 723, 514

—. 2011, The Astrophysical Journal, 740, 9

Ciesla, F. J., & Sandford, S. A. 2012, Science, 336, 452

Cilibrasi, M., Szulágyi, J., Mayer, L., et al. 2018, Monthly Notices of the Royal Astronomical Society, doi:10.1093/mnras/sty2163

Cleeves, L. I., Bergin, E. A., & Harries, T. J. 2015, The Astrophysical Journal, 807, 2

Cleeves, L. I., Öberg, K. I., Wilner, D. J., et al. 2016, The Astrophysical Journal, 832, 110

—. 2018, The Astrophysical Journal, 865, 155

Cochrane, C. J., Murphy, N., Raymond, C. A., et al. 2023, Space Science Reviews, 219, 34

Colose, C. M., Genio, A. D. D., & Way, M. J. 2019, The Astrophysical Journal, 884, 138

Coradini, A., Magni, G., & Turrini, D. 2010, Space Science Reviews, 153, 411

Cossins, A. R., & Bowler, K. 1987, Temperature Biology of Animals (Dordrecht: Springer Netherlands), doi:10.1007/978-94-009-3127-5

Council, N. R., Sciences, D. o. E. a. P., Board, S. S., & Survey, C. o. t. P. S. D. 2012, Vision and Voyages for Planetary Science in the Decade 2013-2022 (National Academies Press)

D'Angelo, G., & Podolak, M. 2015, The Astrophysical Journal, 806, 203

D'Angelo, G., Weidenschilling, S. J., Lissauer, J. J., & Bodenheimer, P. 2021, Icarus, 355, 114087

Deschamps, F., Mousis, O., Sanchez-Valle, C., & Lunine, J. I. 2010, The Astrophysical Journal, 724, 887

Dougherty, A. J., Bartholet, Z. T., Chumsky, R. J., et al. 2018, Journal of Geophysical Research: Planets, 123, 3080

Drazkowska, J., Windmark, F., & Dullemond, C. P. 2013, Astronomy & Astrophysics, 556, A37

Dullemond, C. P., & Dominik, C. 2005, Astronomy and Astrophysics, 434, 971

Fayolle, E. C., Balfe, J., Loomis, R., et al. 2016, The Astrophysical Journal, 816, L28

Folkner, W. M., Woo, R., & Nandi, S. 1998, Journal of Geophysical Research: Planets, 103, 22847

Fouchet, L., & Mayer, L. 2008, arXiv:0806.3975 [astro-ph]

Fujii, Y. I., Okuzumi, S., Tanigawa, T., & Inutsuka, S.-i. 2014, The Astrophysical Journal, 785, 101

Fulton, B. J., Petigura, E. A., Howard, A. W., et al. 2017, The Astronomical Journal, 154, 109

Gordon, S., Mulac, W., & Nangia, P. 1971, The Journal of Physical Chemistry, 75, 2087

Grasset, O., Dougherty, M. K., Coustenis, A., et al. 2013, Planetary and Space Science, 78, 1

Guendelman, I., & Kaspi, Y. 2019, The Astrophysical Journal, 881, 67

Gundlach, B., & Blum, J. 2015, The Astrophysical Journal, 798, 34

Güttler, C., Blum, J., Zsom, A., Ormel, C. W., & Dullemond, C. P. 2009, Geochimica et Cosmochimica Acta Supplement, 73, A482

Haffert, S. Y., Bohn, A. J., de Boer, J., et al. 2019, Nature Astronomy, 3, 749

Haisch, K. E., Lada, E. A., & Lada, C. J. 2001, The Astrophysical Journal, 553, L153

Hansen, C. J., Esposito, L., Stewart, A. I. F., et al. 2006, Science, 311, 1422

Hao, J., Glein, C. R., Huang, F., et al. 2022, Proceedings of the National Academy of Sciences, 119, e2201388119

Hecht, M. H. 2002, Icarus, 156, 373

Heinrich, B. 1977, The American Naturalist, 111, 623

Helled, R., Bodenheimer, P., Podolak, M., et al. 2014, in Protostars and planets VI (Tucson : University of Arizona Press), 643–665

Hernández, J., Hartmann, L., Megeath, T., et al. 2007, The Astrophysical Journal, 662, 1067

Hirschmann, M. M., Bergin, E. A., Blake, G. A., Ciesla, F. J., & Li, J. 2021, Proceedings of the National Academy of Sciences, 118, e2026779118

Hochachka, P. W., & Somero, G. N. 2016, Biochemical Adaptation (Princeton Legacy Library)

Hollenbach, D., Kaufman, M. J., Bergin, E. A., & Melnick, G. J. 2008, The Astrophysical Journal, 690, 1497

Homma, T., Ohtsuki, K., Maeda, N., et al. 2020, The Astrophysical Journal, 903, 98

Hori, Y., & Ikoma, M. 2011, Monthly Notices of the Royal Astronomical Society, 416, 1419

Howell, S. B., Sobeck, C., Haas, M., et al. 2014, Publications of the Astronomical Society of the Pacific, 126, 398

Hubickyj, O., Bodenheimer, P., & Lissauer, J. J. 2005, Icarus, 179, 415

Huey, R. B., & Kingsolver, J. G. 1989, Trends in Ecology & Evolution, 4, 131

Iess, L., Stevenson, D. J., Parisi, M., et al. 2014, Science, 344, 78

Irving, L., & Krog, J. 1954, Journal of Applied Physiology, 6, 667

Jacobson, R. A. 2004, The Astronomical Journal, 128, 492

Jernigan, J., Laflèche, E., Burke, A., & Olson, S. 2023, The Astrophysical Journal, 944, 205

Johansen, A., & Lacerda, P. 2010, Monthly Notices of the Royal Astronomical Society, 404, 475

Johansen, A., & Lambrechts, M. 2017, Annual Review of Earth and Planetary Sciences, 45, 359

Johansen, A., Ronnet, T., Bizzarro, M., et al. 2021, Science Advances, 7, eabc0444

Johnson, T. V., Yeates, C. M., & Young, R. 1992, in The Galileo Mission, ed. C. T. Russell (Dordrecht: Springer Netherlands), 3–21

Kane, S. R., Hill, M. L., Kasting, J. F., et al. 2016, The Astrophysical Journal, 830, 1

Kang, W. 2019a, The Astrophysical Journal, 876, L1

—. 2019b, The Astrophysical Journal, 877, L6

Kargel, J. S. 1991, Icarus, 94, 368

—. 1992, Icarus, 100, 556

Kasting, J. F. 1988, Icarus, 74, 472

Kasting, J. F., & Pollack, J. B. 1983, Icarus, 53, 479

Kasting, J. F., Whitmire, D. P., & Reynolds, R. T. 1993, Icarus, 101, 108

Keeling, C. D., Piper, S. C., Bacastow, R. B., et al. 2001, Scripps Institution of Oceanography

Keller, C., & Gail, H.-P. 2004, Astronomy & Astrophysics, 415, 1177

Keppler, M., Benisty, M., Müller, A., et al. 2018, Astronomy & Astrophysics, 617, A44

Khurana, K. K., Kivelson, M. G., Stevenson, D. J., et al. 1998, Nature, 395, 777

Kilic, C., Lunkeit, F., Raible, C. C., & Stocker, T. F. 2018, The Astrophysical Journal, 864, 106

Kilic, C., Raible, C. C., & Stocker, T. F. 2017, The Astrophysical Journal, 844, 147

Kitadai, N., & Maruyama, S. 2018, Geoscience Frontiers, 9, 1117

Kivelson, M. G., Khurana, K. K., Russell, C. T., et al. 2000, Science, 289, 5

Komacek, T. D., Kang, W., Lustig-Yaeger, J., & Olson, S. L. 2021, Elements, 17, 251

Kretke, K. A., & Levison, H. F. 2014, The Astronomical Journal, 148, 109

Krijt, S., & Ciesla, F. J. 2016, The Astrophysical Journal, 822, 111

Kulikov, Y. N., Lammer, H., Lichtenegger, H. I. M., et al. 2006, Planetary and Space Science, 54, 1425

Kurokawa, H., & Tanigawa, T. 2018, Monthly Notices of the Royal Astronomical Society, 479, 635

Lambrechts, M., & Johansen, A. 2012, Astronomy & Astrophysics, 544, A32

—. 2014, Astronomy & Astrophysics, 572, A107

Lambrechts, M., Johansen, A., & Morbidelli, A. 2014, Astronomy & Astrophysics, 572, A35

Lambrechts, M., & Lega, E. 2017, Astronomy & Astrophysics, 606, A146

Laskar, J., Correia, A. C. M., Gastineau, M., et al. 2004, Icarus, 170, 343

Laskar, J., & Robutel, P. 1993, Nature, 361, 608

Lee, U., Saio, H., & Osaki, Y. 1991, Monthly Notices of the Royal Astronomical Society, 250, 432

Levison, H. F., Kretke, K. A., & Duncan, M. J. 2015, Nature, 524, 322

Levison, H. F., Thommes, E., & Duncan, M. J. 2010, The Astronomical Journal, 139, 1297

Lewis, J. S. 1974, Science, 186, 440

Lewis, J. S., & Prinn, R. G. 1980, The Astrophysical Journal, 238, 357

Li, C., Ingersoll, A., Bolton, S., et al. 2020, Nature Astronomy, 4, 609

Li, J., Bergin, E. A., Blake, G. A., Ciesla, F. J., & Hirschmann, M. M. 2021, Science Advances, 7, eabd3632

Linsenmeier, M., Pascale, S., & Lucarini, V. 2015, Planetary and Space Science, 105, 43

Lissauer, J. J., Hubickyj, O., D'Angelo, G., & Bodenheimer, P. 2009, Icarus, 199, 338

Lissauer, J. J., & Stevenson, D. J. 2007, Formation of Giant Planets (University of Arizona Press)

Lorenz, R. D., Stiles, B. W., Kirk, R. L., et al. 2008, Science, 319, 1649

Lorenz, R. D., Turtle, E. P., Barnes, J. W., et al. 2018, Johns Hopkins APL Technical Digest, 34

Lovegrove, B. G., Heldmaier, G., & Ruf, T. 1991, Journal of Thermal Biology, 16, 185

Lustig-Yaeger, J., Meadows, V. S., & Lincowski, A. P. 2019, The Astronomical Journal, 158, 27

Lyons, T. W., Reinhard, C. T., & Planavsky, N. J. 2014, Nature, 506, 307

Machida, M. N., Kokubo, E., Inutsuka, S., & Matsumoto, T. 2008, The Astrophysical Journal, 685, 1220

MacPherson, G. J. 2014, Calcium-Aluminum-Rich Inclusions in Chondritic Meteorites, Vol. 1 (Elsevier)

Madhusudhan, N., Amin, M. A., & Kennedy, G. M. 2014, The Astrophysical Journal, 794, L12

Madhusudhan, N., Mousis, O., Johnson, T. V., & Lunine, J. I. 2011, The Astrophysical Journal, 743, 191

Mamajek, E. E., Usuda, T., Tamura, M., & Ishii, M. 2009, in AIP Conference Proceedings (Kailua-Kona (Hawaii): AIP), 3–10

Marov, M. Y. 1978, Annual Review of Astronomy and Astrophysics, 16, 141

Marty, B. 2012, Earth and Planetary Science Letters, 313-314, 56

Masters, A., Achilleos, N., Agnor, C., et al. 2014, Planetary and Space Science, 104, 108

McElroy, D., Walsh, C., Markwick, A. J., et al. 2013, Astronomy & Astrophysics, 550, A36

McKay, C. P. 2014, Proceedings of the National Academy of Sciences, 111, 12628

McKinnon, W. B., Lunine, J. I., & Banfield, D. 1995, Origin and evolution of Triton. (University of Arizona Press)

McNab, B. K. 2002, The Physiological Ecology of Vertebrates: A View from Energetics (Cornell University Press)

Meadows, V. S., Reinhard, C. T., Arney, G. N., et al. 2018, Astrobiology, 18, 630

Misener, W., Krijt, S., & Ciesla, F. J. 2019, The Astrophysical Journal, 885, 118

Montesinos, M., Cuadra, J., Perez, S., Baruteau, C., & Casassus, S. 2015, The Astrophysical Journal, 806, 253

Morbidelli, A., Lunine, J., O'Brien, D., Raymond, S., & Walsh, K. 2012, Annual Review of Earth and Planetary Sciences, 40, 251

Morbidelli, A., Szulágyi, J., Crida, A., et al. 2014, Icarus, 232, 266

Mordasini, C. 2013, Astronomy & Astrophysics, 558, A113

Morrison, D., & Cruikshank, D. P. 1974, Space Science Reviews, 15, 641

Mosqueira, I., & Estrada, P. R. 2003a, Icarus, 163, 198

—. 2003b, Icarus, 163, 232

Mousis, O., & Alibert, Y. 2006, Astronomy & Astrophysics, 448, 771

Mousis, O., & Gautier, D. 2004, Planetary and Space Science, 52, 361

Mousis, O., Gautier, D., & Bockelée-Morvan, D. 2002, Icarus, 156, 162

Mousis, O., Lunine, J. I., Thomas, C., et al. 2009, The Astrophysical Journal, 691, 1780

Müller, S., Helled, R., & Cumming, A. 2020, arXiv:2004.13534 [astro-ph]

Nakamoto, T., & Nakagawa, Y. 1994, The Astrophysical Journal, 421, 640

Nelson, R. P., Papaloizou, J. C. B., Masset, F., & Kley, W. 2000, Monthly Notices of the Royal Astronomical Society, 318, 18

Neugebauer, O. 2012, A History of Ancient Mathematical Astronomy (Springer Science & Business Media)

Niemann, H. B., Atreya, S. K., Carignan, G. R., et al. 1996, Science, 272, 846

Nogueira, E., Brasser, R., & Gomes, R. 2011, Icarus, 214, 113

Nowajewski, P., Rojas, M., Rojo, P., & Kimeswenger, S. 2018, Icarus, 305, 84

Oberg, K. I., & Wordsworth, R. 2019, The Astronomical Journal, 158, 194

Oberg, N., Cazaux, S., Kamp, I., et al. 2023, Circumplanetary disk ices II. Composition, doi:10.48550/arXiv.2302.14425

Oberg, N., Kamp, I., Cazaux, S., Woitke, P., & Thi, W.-F. 2022, Circumplanetary disk ices. I. Ice formation vs. viscous evolution and grain drift

Ogihara, M., & Ida, S. 2012, The Astrophysical Journal, 753, 60

Ohno, K., & Ueda, T. 2021, Astronomy & Astrophysics, 651, L2

Okamura, T., & Kobayashi, H. 2021, The Astrophysical Journal, 916, 109

Okuzumi, S., Tanaka, H., Kobayashi, H., & Wada, K. 2012, The Astrophysical Journal, 752, 106

Olmstead, A. T. 1938, The American Journal of Semitic Languages and Literatures, 55, 113

Olson, S. L., Jansen, M., & Abbot, D. S. 2020, The Astrophysical Journal, 895, 19

Olson, S. L., Kump, L. R., & Kasting, J. F. 2013, Chemical Geology, 362, 35

Olson, S. L., Reinhard, C. T., & Lyons, T. W. 2016, Proceedings of the National Academy of Sciences, 113, 11447

Olson, S. L., Schwieterman, E. W., Reinhard, C. T., et al. 2018, The Astrophysical Journal, 858, L14

Ormel, C. W. 2017, in Formation, Evolution, and Dynamics of Young Solar Systems, ed. M. Pessah & O. Gressel, Astrophysics and Space Science Library (Cham: Springer International Publishing), 197–228

Ormel, C. W., & Klahr, H. H. 2010, Astronomy & Astrophysics, 520, A43

Ormel, C. W., & Kobayashi, H. 2012, The Astrophysical Journal, 747, 115

Owen, T., Mahaffy, P., Niemann, H. B., et al. 1999, Nature, 402, 269

Paaijmans, K. P., Heinig, R. L., Seliga, R. A., et al. 2013, Global Change Biology, 19, 2373

Paardekooper, S.-J., & Johansen, A. 2018, Space Science Reviews, 214, 38

Palubski, I. Z., Shields, A. L., & Deitrick, R. 2020, The Astrophysical Journal, 890, 30

Pappalardo, R. T., McKinnon, W. B., & Khurana, K. 2009, Europa (University of Arizona Press)

Pappalardo, R. T., Belton, M. J. S., Breneman, H. H., et al. 1999, Journal of Geophysical Research: Planets, 104, 24015

Parkinson, C. D., Liang, M.-C., Hartman, H., et al. 2007, Astronomy & Astrophysics, 463, 353

Peale, S. J. 1999, Annual Review of Astronomy and Astrophysics, 37, 533

—. 2007, in Treatise on Geophysics, ed. G. Schubert (Amsterdam: Elsevier), 465–508

Petigura, E. A. 2020, The Astronomical Journal, 160, 89

Phillips, C. B., & Pappalardo, R. T. 2014, Eos, Transactions American Geophysical Union, 95, 165

Pineda, J. E., Szulágyi, J., Quanz, S. P., et al. 2019, The Astrophysical Journal, 871, 48

Pirani, S., Johansen, A., Bitsch, B., Mustill, A. J., & Turrini, D. 2019, Astronomy & Astrophysics, 623, A169

Piso, A.-M. A., Öberg, K. I., Birnstiel, T., & Murray-Clay, R. A. 2015, The Astrophysical Journal, 815, 109

Planavsky, N. J., Asael, D., Hofmann, A., et al. 2014, Nature Geoscience, 7, 283

Pollack, J. B., Grossman, A. S., Moore, R., & Graboske, H. C. 1976, Icarus, 29, 35

Pollack, J. B., Hubickyj, O., Bodenheimer, P., et al. 1996, Icarus, 124, 62

Pontoppidan, K. M., Salyk, C., Banzatti, A., et al. 2019, The Astrophysical Journal, 874, 92

Popovas, A., Nordlund, A., Ramsey, J. P., & Ormel, C. W. 2018, Monthly Notices of the Royal Astronomical Society, 479, 5136

Porco, C. C., Helfenstein, P., Thomas, P. C., et al. 2006, Science, 311, 1393

Pringle, J. E. 1991, Monthly Notices of the Royal Astronomical Society, 248, 754

Prinn, R. G., & Barshay, S. S. 1977, Science, 198, 1031

Prinn, R. G., & Fegley, Jr., B. 1981, The Astrophysical Journal, 249, 308

Rab, C., Kamp, I., Ginski, C., et al. 2019, Astronomy & Astrophysics, 624, A16

Rafikov, R. R. 2006, The Astrophysical Journal, 648, 666

—. 2016, The Astrophysical Journal, 830, 7

Raymond, S. N., Quinn, T., & Lunine, J. I. 2005, The Astrophysical Journal, 632, 670

Redfield, A. C. 1942, Woods Hole Oceanographic Institution

—. 1963, The Sea, 2, 26

Reinhard, C. T., Olson, S. L., Kirtland Turner, S., et al. 2020, Geoscientific Model Development, 13, 5687

Reinhard, C. T., Planavsky, N. J., Olson, S. L., Lyons, T. W., & Erwin, D. H. 2016, Proceedings of the National Academy of Sciences, 113, 8933

Reinhard, C. T., Planavsky, N. J., Gill, B. C., et al. 2017, Nature, 541, 386

Richardson, M. I., & Mischna, M. A. 2005, Journal of Geophysical Research: Planets, 110, doi:10.1029/2004JE002367

Ricker, G. R., Winn, J. N., Vanderspek, R., et al. 2014, Journal of Astronomical Telescopes, Instruments, and Systems, 1, 014003

Ridgwell, A., Hargreaves, J. C., Edwards, N. R., et al. 2007, Biogeosciences, 4, 87

Rogers, L. A. 2015, The Astrophysical Journal, 801, 41

Ronnet, T., & Johansen, A. 2020, Astronomy & Astrophysics, 633, A93

Ronnet, T., Mousis, O., & Vernazza, P. 2017, The Astrophysical Journal, 845, 92

Rose, B. E. J., Cronin, T. W., & Bitz, C. M. 2017, The Astrophysical Journal, 846, 28

Russell, S. S., Jr, H. C. C., & Krot, A. N. 2018, Chondrules: Records of Protoplanetary Disk Processes (Cambridge University Press)

Sasaki, T., Stewart, G. R., & Ida, S. 2010, The Astrophysical Journal, 714, 1052

Sato, T., Okuzumi, S., & Ida, S. 2016, Astronomy & Astrophysics, 589, A15

Schneider, A. D., & Bitsch, B. 2021, arXiv:2109.03589 [astro-ph]

Scholander, P. F., Hock, R., Walters, V., & Irving, L. 1950, The Biological Bulletin, 99, 259

Schubert, G., Hussmann, H., Lainey, V., et al. 2010, Space Science Reviews, 153, 447

Schwarz, K. R., & Bergin, E. A. 2014, The Astrophysical Journal, 797, 113

Semenov, D., Henning, T., Helling, C., Ilgner, M., & Sedlmayr, E. 2003, Astronomy & Astrophysics, 410, 611

Shakura, N. I., & Sunyaev, R. A. 1973, Astronomy and Astrophysics, 24, 337

Shibaike, Y., Okuzumi, S., Sasaki, T., & Ida, S. 2017, The Astrophysical Journal, 846, 81

Shibaike, Y., Ormel, C. W., Ida, S., Okuzumi, S., & Sasaki, T. 2019, The Astrophysical Journal, 885, 79

Sicilia-Aguilar, A., Hartmann, L., Calvet, N., et al. 2006, The Astrophysical Journal, 638, 897

Sotin, C., Kalousová, K., & Tobie, G. 2021, Annual Review of Earth and Planetary Sciences, 49, 579

Spiegel, D. S., Menou, K., & Scharf, C. A. 2009, The Astrophysical Journal, 691, 596

Szulágyi, J. 2017, The Astrophysical Journal, 842, 103

Szulágyi, J., Binkert, F., & Surville, C. 2022, The Astrophysical Journal, 924, 1

Szulágyi, J., Cilibrasi, M., & Mayer, L. 2018, The Astrophysical Journal, 868, L13

Szulágyi, J., Masset, F., Lega, E., et al. 2016, Monthly Notices of the Royal Astronomical Society, 460, 2853

Szulágyi, J., Mayer, L., & Quinn, T. 2017, Monthly Notices of the Royal Astronomical Society, 464, 3158

Szulágyi, J., Morbidelli, A., Crida, A., & Masset, F. 2014, The Astrophysical Journal, 782, 65

Szulágyi, J., & Mordasini, C. 2017, Monthly Notices of the Royal Astronomical Society: Letters, 465, L64

Takeuchi, T., & Lin, D. N. C. 2002, The Astrophysical Journal, 581, 1344

Tanigawa, T., Maruta, A., & Machida, M. N. 2014, The Astrophysical Journal, 784, 109

Tanigawa, T., Ohtsuki, K., & Machida, M. N. 2012, The Astrophysical Journal, 747, 47

Titov, D., Bibring, J.-P., Cardesin, A., et al. 2016, EGU General Assembly, EPSC2016

Trigo-Rodríguez, J. M., Rimola, A., Tanbakouei, S., Soto, V. C., & Lee, M. 2019, Space Science Reviews, 215, 18

Tyrrell, T. 1999, Nature, 400, 525

Valencia, D., O'Connell, R. J., & Sasselov, D. 2006, Icarus, 181, 545

Van Eylen, V., Agentoft, C., Lundkvist, M. S., et al. 2018, Monthly Notices of the Royal Astronomical Society, 479, 4786

Venturini, J., Alibert, Y., Benz, W., & Ikoma, M. 2015, Astronomy & Astrophysics, 576, A114

Visser, R. G., & Ormel, C. W. 2016, Astronomy & Astrophysics, 586, A66

von der Heydt, A., & Dijkstra, H. A. 2006, Paleoceanography, 21, doi:10.1029/2005PA001149

—. 2008, Global and Planetary Change, 62, 132

Wada, K., Tanaka, H., Suyama, T., Kimura, H., & Yamamoto, T. 2009, The Astrophysical Journal, 702, 1490

Wagner, K., Follete, K. B., Close, L. M., et al. 2018, The Astrophysical Journal, 863, L8

Wahl, S. M., Hubbard, W. B., Militzer, B., et al. 2017, Geophysical Research Letters, 44, 4649

Wang, J., Mawet, D., Hu, R., et al. 2018, Journal of Astronomical Telescopes, Instruments, and Systems, 4, 035001

Wang, J. J., Ginzburg, S., Ren, B., et al. 2020, The Astronomical Journal, 159, 263

Wang, Y., Liu, Y., Tian, F., et al. 2016, The Astrophysical Journal, 823, L20

Wang, Y., Ormel, C. W., Huang, P., & Kuiper, R. 2023, Monthly Notices of the Royal Astronomical Society, 523, 6186

Wanninkhof, R. 2014, Limnology and Oceanography: Methods, 12, 351

Ward, W. R., & Canup, R. M. 2010, The Astronomical Journal, 140, 1168

Way, M. J., Aleinov, I., Amundsen, D. S., et al. 2017, The Astrophysical Journal Supplement Series, 231, 12

Weidenschilling, S. J. 1977, Monthly Notices of the Royal Astronomical Society, 180, 57

—. 1980, Icarus, 44, 172

—. 1995, Icarus, 116, 433

Williams, D. M., & Kasting, J. F. 1997, Icarus, 129, 254

Williams, G. E. 1993, Earth-Science Reviews, 34, 1

Wolff, S. G., Ménard, F., Caceres, C., et al. 2017, The Astronomical Journal, 154, 26

Wray, J. J. 2021, Annual Review of Earth and Planetary Sciences, 49, 141

Wright, R. K., & Cooper, E. L. 1981, Developmental & Comparative Immunology, 5, 117

Wu, Y.-L., Bowler, B. P., Sheehan, P. D., et al. 2022, The Astrophysical Journal Letters, 930, L3

Wyatt, M. C. 2008, Annual Review of Astronomy and Astrophysics, 46, 339

Youdin, A. N., & Goodman, J. 2005, The Astrophysical Journal, 620, 459

Zhu, Z., Andrews, S. M., & Isella, A. 2018, Monthly Notices of the Royal Astronomical Society, 479, 1850

Zhu, Z., Nelson, R. P., Dong, R., Espaillat, C., & Hartmann, L. 2012, The Astrophysical Journal, 755, 6

Zimmer, C. 2000, Icarus, 147, 329

Zsom, A., & Dullemond, C. P. 2008, Astronomy & Astrophysics, 489, 931

Öberg, K. I., Boogert, A. C. A., Pontoppidan, K. M., et al. 2011a, The Astrophysical Journal, 740, 109

Öberg, K. I., Murray-Clay, R., & Bergin, E. A. 2011b, The Astrophysical Journal, 743, L16